Super-dense Hydrogen Adsorption below Critical Temperature
(臨界温度以下における超高密度水素吸着)

学位取得年月　2023 年 3 月

魏　弘之

Abstract

In this work, the cryogenic H_2 adsorption properties were systematically investigated below the critical temperature of H_2 (33 K). Especially, we focused on the studies for the "super-dense H_2 adsorption" which had much higher density than liquid H_2 density. This is of great interest because the properties of super-dense H_2 are contrary to the general understanding that the upper limit of adsorbed H_2 density is equivalent to the density of liquid H_2. However, the reports about super-dense H_2 adsorption are still few, and the factors and conditions leading to the super-dense H_2 state is not understood well. This work is the first report as systematic research of the cryogenic H_2 adsorption to understand the super-dense H_2 adsorption by investigating the material dependence, temperature dependence, adsorbed layer dependence and gas dependence.

The densities of adsorbed H_2 were measured by the volumetric method using PCI (Pressure-Composition-Isotherm) apparatus equipped with a cryostat system. The 9 kinds of materials with different elements and textural properties (specific surface area, pore size, pore volume), such as carbon materials, MOFs, and silica gels, were used as absorbents. The temperature change of adsorbed H_2 densities were evaluated below the critical temperature of H_2. In order to investigate the adsorbed layer dependence of the super-dense H_2 adsorption, BET theory was used and the monolayer and multilayer H_2 were evaluated separately. These results for H_2 were compared with that for deuterium (D_2), neon (Ne), and nitrogen (N_2) at each liquefied temperature.

As a result, it is revealed that the density of monolayer H_2, which is adsorbed just on the surface of adsorbents, is evaluated to be 50 mmol/cm^3 regardless of temperature changes below 33 K and the differences of elements and textural properties of adsorbents. In other words, the monolayer adsorption is the factor leading to the super-dense H_2 adsorption without the material and temperature dependence. It is noteworthy that the monolayer H_2 as the super-dense state has higher density than not only the liquid H_2 density (35 mmol/cm^3) but also the solid H_2 density (43

mmol/cm^3). From the practical point of view, the volumetric H_2 uptake including the volume of adsorbents themselves is the important value for the H_2 storage. it is found that the volumetric surface area of adsorbents is a unique factor to increase the volumetric H_2 uptake.

In contrast to the results of super-dense H_2 adsorption as described above, the density of adsorbed Ne and N_2 are almost equivalent to that of liquid phase at each liquified temperature, indicating that Ne and N_2 do not form the super-dense state. On the other hand, the density of adsorbed D_2 shows higher density than that of liquid D_2, and the temperature independence similar to the super-dense H_2 is also revealed. Furthermore, the monolayer D_2 and H_2 have equivalent density of 50 mmol/cm^3, even though the density of liquid D_2 is 1.15 times higher than that of H_2 at each boiling point. It is known that the lower density of liquid H_2 is caused by the higher zero-point energy compared with that of D_2. Therefore, it can be expected that the quantum effect caused by the different zero-point energy is cancelled out by interactions between adsorbates and adsorbents at cryogenic conditions, and the super-dense H_2 is formed.

Contents

1. Introduction

1.1 Carbon neutral society

Energy is the most fundamental ingredient for human society. But we mostly obtain energy from fossil fuels, which is a major cause of global warming and climate change due to the carbon dioxide (CO_2) emission. The Intergovernmental Panel on Climate Change (IPCC) reported that "Human influence on the climate system is clear" in the fifth assessment report in 2013,[1] furthermore, the sixth assessment report emphasizes human influence as "It is unequivocal that human influence has warmed the atmosphere, ocean and land" published in 2022.[2] The 21st session of the Conference of the Parties (COP21), which is the international climate summit, was held, and the Paris Agreement was adopted by 194 parties. Its goal is to keep the increase in global temperature increase below 2 ºC, preferably to 1.5 ºC compared to pre-industrial levels. The aim of Japan in the Paris Agreement is 26% of reduction in greenhouse gas emissions by 2030 and 80% of reduction by 2050 compared to that in 2013. In this recent year, the Japanese government declared the aim of carbon neutrality by 2050. To achieve these goals, renewable energy such as wind, solar, and hydropower should be mainstream power sources. However, renewable energy supply is not a good match to energy demand because of the lack of adjustment ability of renewable energy. Some suitable energy storage devices, such as rechargeable batteries, pumped hydropower, heat storage, compressed air, and flywheel, are necessary. Hydrogen (H_2) is the most important candidate to realize not only energy storage but also energy transportation. Therefore, it has been widely recognized that a hydrogen-based energy system is necessary to realize a carbon-free society because of the H_2 ability of regenerative properties with zero emissions of pollute gases such as CO_2 and high gravimetric energy density. However, the technological development of H_2 storage and transportation still needs challenges for the realization of a hydrogen-based society.

1.2 Properties of Hydrogen

The hydrogen atom (Protium) is the simplest element in the universe. Protium is composed of one proton and one electron. There are two isotopes of hydrogen, which are deuterium and tritium with one and two neutrons, respectively. The elemental hydrogen usually exists as a hydrogen molecule (H_2) with a covalent bond. Table 1.2.1 shows the physical properties of H_2 and deuterium molecules (D_2). Fig. 1.2.1 shows the binding energy of hydrogen molecule, and the energy levels of the stretching vibration as a function of internuclear distance[3,4] . The vibration frequency (ν_0) of H-H binding as the harmonic oscillator at the ground state of the binding energy is given by

$$\nu_0 = \frac{1}{2\pi}\sqrt{\frac{k}{\mu}}, \tag{1.2.1}$$

where μ is the reduced mass given by $\frac{m \cdot m}{m+m}$; m is the mass of atomic hydrogen; k is the curvature of the potential of the harmonic oscillation. According to the quantum theory, the vibration energy ($e_V^{n_V}$) is given by

$$e_V^{n_V} = \left(n_V + \frac{1}{2}\right)h\nu_0, \qquad n_V = 0,1,2\cdots, \tag{1.2.2}$$

where h is the Planck constant. The $n_V = 0$, e_V^0 $(= \frac{1}{2}h\nu_0)$ is called zero-point vibration energy, which depends on the mass of the atom. The lighter mass of hydrogen gives a higher zero-point vibration energy compared with that of deuterium, resulting in different physical properties as shown in Table 1.2.1.

Since the excitation energy of the stretching vibration is quite large, most of the H_2 molecules exist on the ground state below 2000 K, and the partition function is given by

$$Z_v = \sum_{n_V} \exp\left(-\frac{e_V^{n_V}}{k_B T}\right) \approx \exp\left(-\frac{e_V^0}{k_B T}\right) \tag{1.2.3}$$

The partition function for the rotational motion (Z_r) is given

$$Z_r = \frac{1}{2}\sum_J (2J+1)\exp\left(-\frac{e_r^J}{k_B T}\right) \tag{1.2.4}$$

$$e_r^J = \frac{h^2}{8\pi^2 I_r} J(J+1), \qquad J = 0, 1, 2 \cdots, \tag{1.2.5}$$

where J is the rotational quantum number; I_r ($= \frac{1}{2}\mu r^2$) is the moment of inertia. The important thing that rotational motion provides is that there are two distinct states of ortho-H_2 and para-H_2. Protium is a fermion with a nuclear spin of 1/2, so the H_2 molecule has total nuclear spins (I) of $I = 1$ or $I = 0$, which are categorized as ortho-H_2 and para-H_2, respectively. In the case of $I = 1$, the ortho-H_2 is 3-fold degenerate and it takes $J = \text{odd}$. In the case of $I = 0$, the para-H_2 is 1-fold degenerate and it takes $J =$even. These distinctions are due to the requirement of fermions that the wave function must be antisymmetric under particle exchange. The ratio of ortho-H_2 and para-H_2 in thermal equilibrium is given by

$$\frac{Z_o}{Z_p} = \frac{g_{(I=1)} \sum_{J=odd}(2J+1)\exp\left(-\frac{e_r^J}{k_B T}\right)}{g_{(I=0)} \sum_{J=even}(2J+1)\exp\left(-\frac{e_r^J}{k_B T}\right)}, \tag{1.2.6}$$

where $g_{(I)}$ is each degeneracy ($g_{(I=1)} = 3$ and $g_{(I=0)}$=1). Fig. 1.2.2 shows the ratio of ortho-H_2/para-H_2 as a function of temperature, obtained from equation 1.2.6. At room temperature, the ortho-para ratio is approximately 3:1 (75%:25%), since the statistical multiplicities for each rotational state are equivalent. On the other hand, almost all of H_2 exists as para-H_2 at the boiling point (20.4 K), because the distribution of the rotational state at the ground state ($J = 0$) increases at a lower temperature.

Table. 1.2.1 Some properties of H_2 and D_2.[3,5,6]

	unit	H_2	D_2
Molecular mass	g/mol	2.016	4.282
Natural abandance	%	99.985	0.015
Binding energy	eV	4.748	4.748
Dissociation energy	eV	4.478	4.556
Zero point vibration energy	eV	0.270	0.192
Triplet point (temperature)	K	13.96	18.73
Triplet point (pressure)	kPa	7.2	17.15
Critical point (temperature)	K	32.98	38.34
Critical point (pressure)	kPa	1.298	1.649
Boiling point at 0.1 MPa	K	20.41	23.67
Latent heat	J/mol	913	1235

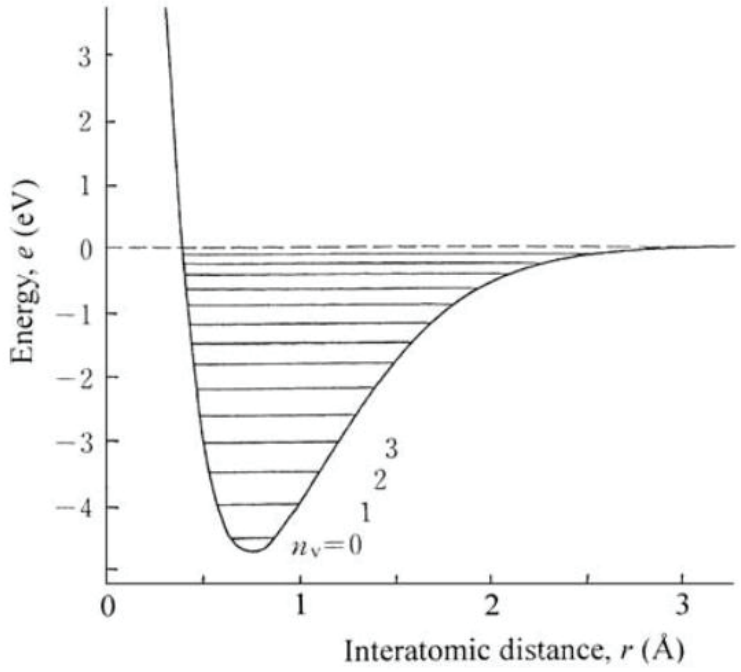

Fig. 1.2.1 Adiabatic potential and energy levels of the stretching vibration of H_2 molecule. [3,4]

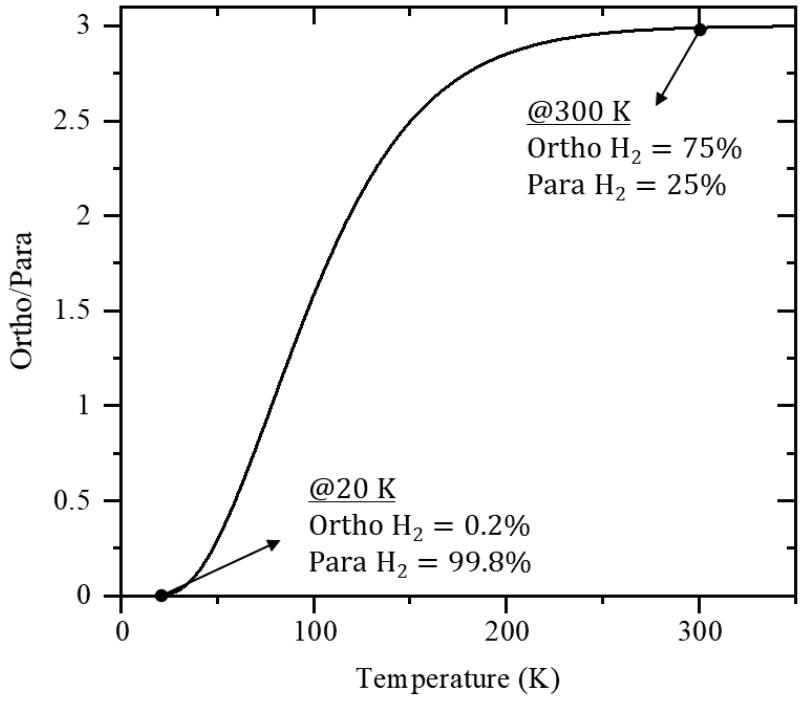

Fig. 1.2.2 Equilibrium ortho-para ratio of hydrogen as a function of temperatures.

1.3 Hydrogen storage

Table 1.3.1 shows the gravimetric and volumetric energy density (Higher Heating Value; HHV) of H_2 and common fuels.[7] H_2 has a very high gravimetric energy density compared with other fuels such as gasoline, diesel, and natural gas. On the other hand, the volumetric energy density of H_2 under ambient conditions is extremely low compared with other fuels. In order to increase the volumetric and gravimetric energy density of H_2, the following techniques have been considered: Compressed H_2, Liquid H_2, and H_2 ab/adsorption on materials, which are described below.

Table 1.3.1 Gravimetric and volumetric energy density (HHV) of fuels.[7]

Fuel	Condition	Gravimetric dnergy density MJ/kg	Volumetric energy density MJ/L
Hydrogen	ambient condition	142	0.012
	compressed (70 MPa)		5.6
	liquid (20 K)		10.1
Gasoline	ambient condition	46.4	34.2
Desel	ambient condition	45.4	34.6
Natural gas	compressed 25 MPa	53.6	9
	liquid		22.2

Compressed hydrogen

Compressed H_2 is the most common method of H_2 storage and transportation. A typical steel cylinder stores the compressed H_2 at 15 MPa. A new type of high-pressure H_2 tank, which consists of three layers made from the plastic liner, carbon fiber reinforced plastic (CFRP), and grass fiber reinforced plastic layer (GFRP), is used for the fuel cell vehicle (FCV). The high-pressure tank developed by TOYOTA stores compressed H_2 at 70 MPa and the gravimetric H_2 density is 6.0 wt.% including the weight of the H_2 tank.[8] Even for H_2 highly compressed at 70 MPa, volumetric energy density is not high compared with other fuels as shown in Table 1.3.1.

Liquid hydrogen

Fig. 1.3.1 shows the phase diagram of H_2, which is referred from the National Institute of Standards and Technology (NIST) chemistry Web Book.[9] The boiling point of H_2 is 20.4 K under 0.1 MPa of pressure, and the triplet point of H_2 is at 14.0 K and 0.007 MPa. Since the critical point of H_2 is 33.0 K at 1.3 MPa, thus H_2 can't be liquified at room temperature even under high the pressure. The volumetric density of liquid H_2 is 35.2 mmol/cm^3 at the boiling point, which is about 800 times higher than the density of gaseous H_2 at the standard ambient temperature and pressure (0.040 mmol/cm^3 at 298.15 K and 0.1 MPa) and much higher than the density of compressed H_2 at 70 MPa (19.5 mmol/cm^3).

Liquid H_2 is considered as a practicable method for large-scale H_2 transport due to the high volumetric H_2 density. In this recent years, Kawasaki Heavy Industries, Ltd. has built a large-scale liquid H_2 carrier.[10] The technique of liquid H_2 storage is being developed, but there are still challenges, which are the development of a high energy-efficient liquefaction technique, and the suppression of H_2 losses by evaporation of liquid H_2 (boil-off). The boil-off is caused by heat input from an outer wall of the storage tank, and internal heat generation by the ortho-para conversion.

The ortho-para ratio is approximately 3:1 at room temperature, while almost all of H_2 exists as para-H_2 at the boiling point (20.4 K). This ortho-para conversion is the exothermic reaction with 1.406 kJ/mol of heat generation ($J = 1 \rightarrow 0$), which is higher than the heat of vaporization of H_2 (913 J/mol).[4] Since interconversion between these isomers is a forbidden process in an isolated molecule, it takes a long time more than 100 h to complete the ortho-para conversion reaction. In long-term storage of liquid H_2, the ortho-para conversion gradually proceeds and it leads to the boil-off due to the internal heat generation. To avoid this problem, it is necessary to complete the ortho-para conversion at the moment of liquefying H_2 by using ortho-para conversion catalysts improving the sluggish kinetics.

H_2 ab/adsorption on materials

In order to achieve higher gravimetric and volumetric H_2 density compared with the compressed H_2 and liquid H_2, various kinds of material-based H_2 storage methods have been investigated. There are two types of sorption to store H_2 in solid-state materials, which are “chemical absorption” and “physical adsorption”.

In the case of chemical absorption, the atomic hydrogen is bonded to materials, and hydrides are formed with metallic, ionic, or covalent bonds, which lead to relatively high volumetric H_2 density. However, they generally require thermal management to control the reaction of H_2 absorption and desorption due to the enthalpy change for the formation of hydrides. For example, magnesium hydride (MgH_2) with the enthalpy of formation of 74 kJ/mol requires 300 °C to desorb H_2 at 0.1 MPa.[3,11] Furthermore, the slow kinetics of reactions are often problematic to control of the H_2 absorption and desorption. In the case of MgH_2, it requires a higher temperature than 300 °C for H_2 absorption reaction as a thermal activation even though it proceeds in an exothermic reaction.[12] In order to improve the kinetic issues, the use of catalysts and several activation processes are generally

required.[11–15] Thus, the H_2 storage by chemical absorption using materials realize the high volumetric H_2 density, while there are thermodynamic and kinetic issues for the practical H_2 absorption and desorption process.

On the other hand, molecular H_2 can be stored on the surface of materials by physical adsorption (hereinafter, this is just called “adsorption”). The H_2 adsorption is mainly due to the weak van der Waals interaction between the H_2 molecule and material surface, and this phenomenon is similar to the condensation from a gas to a liquid phase. The enthalpy of the physical adsorption is less than 10 kJ/mol,[16] which is slightly higher than the enthalpy of liquefaction. In consequence, low temperature and high pressure are required to obtain high H_2 capacity for the H_2 adsorption. The processes of H_2 adsorption and desorption show good reversibility with fast kinetics.

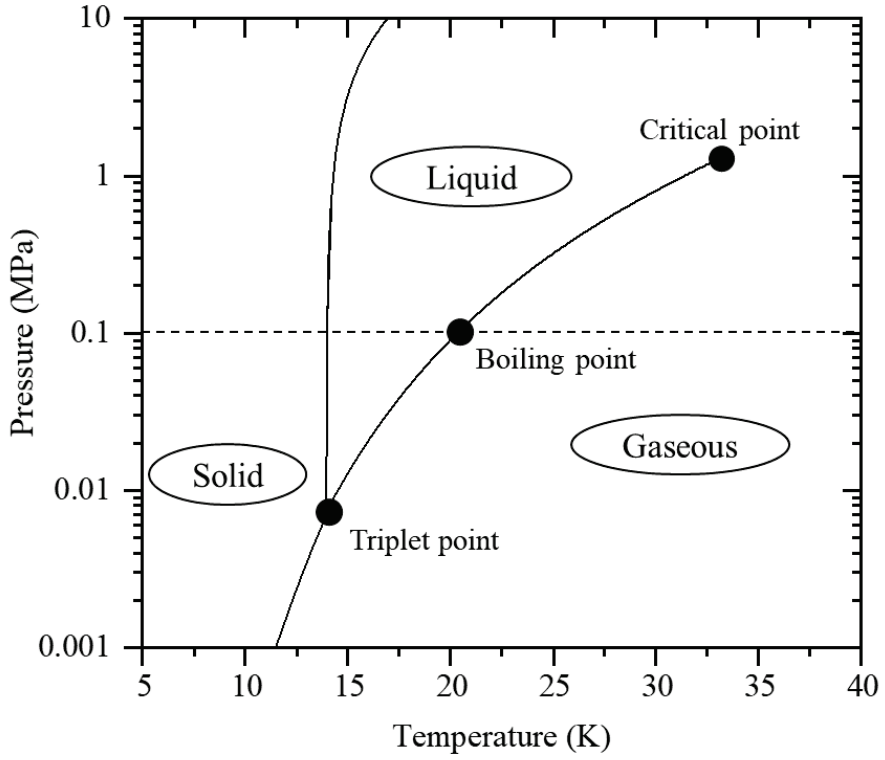

Fig. 1.3.1 Phase diagram of H_2. The boiling point is at 20.4 K and 0.1 MPa, the critical point of H_2 is at 33.0 K and 1.3 MPa, the triplet point of H_2 is at 14.0 K and 0.007 MPa.

1.4 Previous work on hydrogen physical adsorption

The H_2 adsorption storage on the surface of materials has long been studied to improve the gravimetric and volumetric H_2 density. In 1997, Dillon et al.[17] published the quite high gravimetric storage density (5~10 wt.%) on single-walled nanotubes (SWNTs) under ambient conditions. However, the inadequacy of this report has been proved by Hirscher et al.[18] who clarified that the titanium alloy contained in the synthesis process of SWNTs stored H_2, and the true capacity of only SWNTs was just around 1 wt.%. In 1998, Chambers et al.[19] also published the extremely high gravimetric H_2 density (~67 wt.%) on graphite nanofibers (GNF), but the result has not been reproduced even though many validation experiments have been performed.[20–22] The above huge H_2 capacity of carbon materials has not been confirmed unfortunately. However, these high-impact reports stimulated this research field and accelerated the research and development more actively.

The porous carbon materials with a high specific surface area have been developed,[23–37] because it has been revealed that the gravimetric H_2 uptake approximately corresponds to 1 wt.% H_2 per 500 m^2/g of specific surface area at 77 K, which is the so-called Chahine's rule.[38,39] Fig. 1.4.1 shows the linear relationship between H_2 uptake and specific surface area for carbon materials,[24] indicating that the specific surface area is the critical factor to increase the H_2 adsorption capacity. The super-activated carbon of "MAXSORB",[40–42] which is manufactured by an alkali activation process, has the highest specific surface area (more than 3000 m^2/g) in the carbon materials, and it shows the gravimetric H_2 uptake of 5 wt.% at 77 K above 2 MPa of pressure.[23] However, the research field of carbon materials for H_2 storage tends to stagnate due to the limit of material development to obtain higher surface area.

In late 1990, a new type of high surface area material of Metal-Organic Framework (MOF) was developed.[43] MOFs are crystalline porous materials composed of metal ions and organic ligands, which act as the joints and linkers in the network structure, respectively. By changing the metal ions

and organic ligands, it is possible to design the desired pore structure. The first paper for H_2 storage using MOFs was reported in 2003 using MOF-5 with a surface area of 2500 m^2/g,[44] which shows 4.5 wt.% of the gravimetric H_2 uptake at 77 K below 0.1 MPa, but this result was corrected to 1.3 wt.% at 77 K and 0.1 MPa.[45] After that, a lot of MOFs were developed and H_2 adsorption uptakes were investigated.[24,46–63] Fig. 1.4.2 shows the gravimetric H_2 uptake for each MOFs material obtained at 77 K as a function of the specific surface area.[24] The linear relationship between the gravimetric H_2 uptake and the specific surface area is also observed on MOF materials, and it was clarified that Chahine's rule is adequate for MOF materials as well.[64] Therefore, it can be concluded that the gravimetric H_2 uptake on solid materials is proportional to the specific surface area, namely, the specific surface area is the critical factor to increase the gravimetric H_2 storage uptake.

The volumetric H_2 density is also an important value as the practical performance for H_2 storage. However, there is a trade-off relationship between volumetric and gravimetric surface area, i.e., volumetric and gravimetric H_2 uptake, for porous materials.[65,66] For example, although ultra-porous MOF materials, e.g., MOF-210,[61] NU110,[62] and DUT60[63] have a relatively high gravimetric surface area in the range of 6000-8000 m^2/g, they have a relatively low volumetric surface area and H_2 uptake due to the high pore volume and large pore size. Some papers have focused on the development of MOFs to optimize the gravimetric and volumetric H_2 capacity.[65,66] As described above, the history of H_2 adsorption storage using porous materials can be said to be the history of the development of materials with a high specific surface area.

In order to improve the H_2 adsorption capacity, it is important not only to develop porous materials but also to understand the properties of adsorbate (adsorbed H_2) on the material surface. In general understanding, adsorbates are regarded as a liquid phase at the boiling point of the adsorbates. The cross-sectional area of N_2, which is a two-dimensional area per molecule widely used for the evaluation of the surface area, at the boiling point of N_2 (77 K) is determined based on

the three-dimensional (3D) density of liquid N_2.[67] For the adsorbate of H_2, the density of adsorbed H_2 is also regarded as that of liquid H_2 in a lot of papers,[23,24,68] in other words, the upper limit of adsorbed H_2 density is regarded as the density of liquid H_2. This indicates that the volumetric H_2 capacity using porous materials would never be superior to that of liquid H_2, no matter how high a specific surface area of the material is developed. However, the conventional experiments carried out at 77 K are inadequate to understand the essential properties of adsorbed H_2 because the boiling point of H_2 is 20.4 K.

In 1949, Livingston[67] reported the anomalously low cross-sectional areas of H_2 (8.3 Å/molecule) adsorbed on the surface of Ni foil at 20 K compared with the value estimated from liquid H_2 density (14.2 Å/molecule), indicating the anomalously high two-dimensional (2D) density of monolayer H_2 on the material surface. In the quite recent year 2022, Xicohténcatl et al.[69] reported the anomalously high 2D density of monolayer H_2 on mesoporous silica at 20.4 K, which shows 7.1 Å/molecule of H_2 cross-sectional area with the density larger than bulk-liquid and solid H_2. These results are contrary to the general understanding that the upper limit of adsorbed H_2 density is equivalent to the density of liquid H_2. They called the highly condensed H_2 "super-dense H_2". In this study, we also found the super-dense H_2 on a super-activated carbon at 20.4 K, which showed the three-dimensional (3D) density of 43.1 mmol/cm^3 with the density higher than bulk-liquid and bulk-solid H_2. This result is described later in the section 4.2.1. This is expected to further enhancement of H_2 adsorption capacity from the practical point of view and further understanding of the physical properties of adsorbed H_2 from the academic point of view.

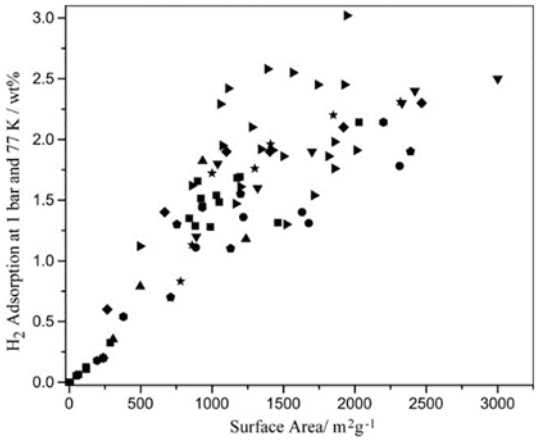

Fig. 1.4.1 The liner relationship between H_2 uptake and the surface area at 77 K and 0.1 MPa for carbon materials: (■) Nijkamp et al.,[36] (●) Pang et al.,[34] (◆) Parra et al.,[35] (★) Takagi et al.,[33] (▲) Zhao et al.,[32,37] (▼) Texier-Mandoki et al.,[29] (⬟) Gadiou et al.,[31] and (▶) Gogotsi et al.[30]

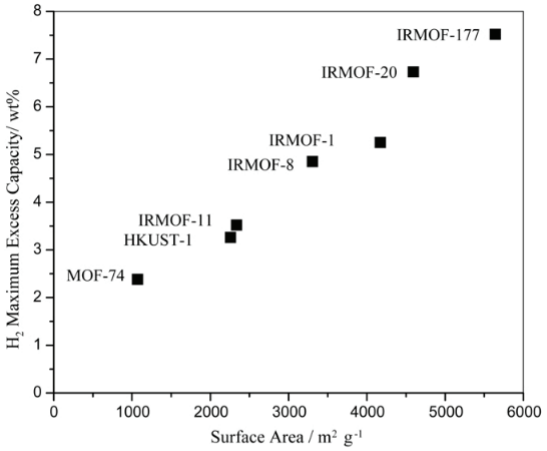

Fig. 9. The variation of H_2 adsorbed at saturation with Langmuir surface area for porous metal organic framework materials at 77 K [36].

Fig. 1.4.2 The liner relationship between H_2 uptake and the surface area at 77 K with Langmuir surface area for metal-organic frameworks (MOFs). [24]

References

1. Pahchauri, R. K., Allen, M. R., R., V., Barros, J. B. & Wolfgang Cramer. *Climate Change 2014: Fifth Assessment Report*. *Journal of Crystal Growth* vol. 218 (2000).
2. Valerie, M.-D. *et al.* Climate Change 2021: Sixth Assessment Report. *Climate Change 2021: The Physical Science Basis.* 1–16 (2021) doi:10.1017/9781009157896.
3. Fukai, Y. *The Metal-Hydrogen System*. (Springer, 2004).
4. Van Kranendonk, J. *SOLID HYDROGEN*. (Plenum, 1983).
5. Haissinsky, M. *Nuclear Chemistry and Its Appplications*. (Addison-Wesley, 1964).
6. Vargaftik, N. B. *Tables on the thermophysical properties of liquids and gases*. (Hemisphere Pub. Corp., 1975).
7. Mazloomi, K. & Gomes, C. Hydrogen as an energy carrier: Prospects and challenges. *Renewable and Sustainable Energy Reviews* **16**, 3024–3033 (2012).
8. https://www.toyota.co.jp/fuelcells/en/technology.html.
9. Eric W. Lemmon, Ian H. Bell, Marcia L. Huber, and Mark O. McLinden, "Thermophysical Properties of Fluid Systems" in NIST Chemistry WebBook, NIST Standard Reference Database Number 69, Eds. P.J. Linstrom and W.G. Mallard, National Institute of Standards and Technology, Gaithersburg MD, 20899, https://webbook.nist.gov/chemistry/, (retrieved September 19, 2022).
10. https://global.kawasaki.com/en/corp/newsroom/news/detail/?f=20220422_3378.
11. Kimura, T., Miyaoka, H., Ichikawa, T. & Kojima, Y. Hydrogen absorption of catalyzed magnesium below room temperature. *Int J Hydrogen Energy* **38**, 13728–13733 (2013).
12. Gi, H. *et al.* Effective Factor on Catalysis of Niobium Oxide for Magnesium. *ACS Omega* **5**, 21906–21912 (2020).
13. Barkhordarian, G., Klassen, T. & Bormann, R. U. Effect of Nb2O5 content on hydrogen reaction kinetics of Mg. *J Alloys Compd* **364**, 242–246 (2004).
14. Barkhordarian, G., Klassen, T. & Bormann, R. Catalytic mechanism of transition-metal compounds on Mg hydrogen sorption reaction. *Journal of Physical Chemistry B* **110**, 11020–11024 (2006).
15. Hanada, N., Ichikawa, T. & Fujii, H. Catalytic effect of Ni nano-particle and Nb oxide on H-desorption properties in MgH2 prepared by ball milling. *J Alloys Compd* **404–406**, 716–719 (2005).
16. Boateng, E. & Chen, A. Recent advances in nanomaterial-based solid-state hydrogen storage. *Mater Today Adv* **6**, 100022 (2020).
17. Dillon, A. C. *et al.* Storage of hydrogen in single-walled carbon nanotubes. *Nature* **386**, 377–379

(1997).

18. Hirscher, M. *et al.* Hydrogen storage in sonicated carbon materials. *Appl Phys A Mater Sci Process* **72**, 129–132 (2001).
19. Chambers, A., Park, C., R., B. T. K. & M., R. N. Hydrogen storage in platelet graphite nanofibers. *Sep Purif Technol* **58**, 219–223 (2007).
20. Ahn, C. C. *et al.* Hydrogen desorption and adsorption measurements on graphite nanofibers. *Appl Phys Lett* **73**, 3378–3380 (1998).
21. Ströbel, R. *et al.* Hydrogen adsorption on carbon materials. *J Power Sources* **84**, 221–224 (1999).
22. Ye, Y. *et al.* Hydrogen adsorption and cohesive energy of single-walled carbon nanotubes. *Appl Phys Lett* **74**, 2307–2309 (1999).
23. Kojima, Y. *et al.* Hydrogen adsorption and desorption by carbon materials. *J Alloys Compd* **421**, 204–208 (2006).
24. Thomas, K. M. Hydrogen adsorption and storage on porous materials. *Catal Today* **120**, 389–398 (2007).
25. Man Mohan, Vinod Kumar Sharma, Gayathri, E. Anil Kumar, V. G. Hydrogen storage in carbon materials. *Energy Storage* **1**, 1–26 (2019).
26. Ströbel, R., Garche, J., Moseley, P. T., Jörissen, L. & Wolf, G. Hydrogen storage by carbon materials. *J Power Sources* **159**, 781–801 (2006).
27. Sevilla, M. & Mokaya, R. Energy storage applications of activated carbons: Supercapacitors and hydrogen storage. *Energy Environ Sci* **7**, 1250–1280 (2014).
28. Xia, Y., Yang, Z. & Zhu, Y. Porous carbon-based materials for hydrogen storage: Advancement and challenges. *J Mater Chem A Mater* **1**, 9365–9381 (2013).
29. Texier-Mandoki, N. *et al.* Hydrogen storage in activated carbon materials: Role of the nanoporous texture. *Carbon N Y* **42**, 2744–2747 (2004).
30. Gogotsi, Y. *et al.* Tailoring of nanoscale porosity in carbide-derived carbons for hydrogen storage. *J Am Chem Soc* **127**, 16006–16007 (2005).
31. Gadiou, R. *et al.* The influence of textural properties on the adsorption of hydrogen on ordered nanostructured carbons. *Microporous and Mesoporous Materials* **79**, 121–128 (2005).
32. Zhao, X. B., Xiao, B., Fletcher, A. J. & Thomas, K. M. Hydrogen adsorption on functionalized nanoporous activated carbons. *Journal of Physical Chemistry B* **109**, 8880–8888 (2005).
33. Takagi, H., Hatori, H., Yamada, Y., Matsuo, S. & Shiraishi, M. Hydrogen adsorption properties of

activated carbons with modified surfaces. *J Alloys Compd* **385**, 257–263 (2004).

34. Pang, J., Hampsey, J. E., Wu, Z., Hu, Q. & Lu, Y. Hydrogen adsorption in mesoporous carbons. *Appl Phys Lett* **85**, 4887–4889 (2004).

35. Parra, J. B. *et al.* Textural development and hydrogen adsorption of carbon materials from PET waste. *J Alloys Compd* **379**, 280–289 (2004).

36. Nijkamp, M. G., Raaymakers, J. E. M. J., van Dillen, A. J. & de Jong, K. P. Hydrogen storage using physisorption-materials demands. *Appl Phys A Mater Sci Process* **72**, 619–623 (2001).

37. Zhao, X., Villar-Rodil, S., Fletcher, A. J. & Thomas, K. M. Kinetic Isotope Effect for H 2 and D 2 Quantum Molecular Sieving in Adsorption/Desorption on Porous Carbon Materials. (2006) doi:10.1021/jp060748p.

38. Poirier, E., Chahine, R. & Bose, T. K. Hydrogen adsorption in carbon nanostructures. *Int J Non Linear Mech* **26**, 831–835 (2001).

39. Bénard, P. & Chahine, R. Storage of hydrogen by physisorption on carbon and nanostructured materials. *Scr Mater* **56**, 803–808 (2007).

40. Zhao, W., Fierro, V., Fernández-Huerta, N., Izquierdo, M. T. & Celzard, A. Impact of synthesis conditions of KOH activated carbons on their hydrogen storage capacities. *Int J Hydrogen Energy* **37**, 14278–14284 (2012).

41. Zhao, W. *et al.* Activated carbons with appropriate micropore size distribution for hydrogen adsorption. *Int J Hydrogen Energy* **36**, 5431–5434 (2011).

42. Otowa, T., Tanibata, R. & Itoh, M. Production and adsorption characteristics of MAXSORB: High-surface-area active carbon. *Gas Separation and Purification* **7**, 241–245 (1993).

43. Li, H., Eddaoudi, M., O'Keeffe, M. & Yaghi, O. M. Design and synthesis of an exceptionally stable and highly. *Nature* **402**, 276–279 (1999).

44. Rosi, N. L. *et al.* Hydrogen storage in microporous metal-organic frameworks. *Science (1979)* **300**, 1127–1129 (2003).

45. Rowsell, J. L. C., Millward, A. R., Park, K. S. & Yaghi, O. M. Hydrogen Sorption in Functionalized Metal-Organic Frameworks. *J Am Chem Soc* **126**, 5666–5667 (2004).

46. Shet, S. P., Shanmuga Priya, S., Sudhakar, K. & Tahir, M. A review on current trends in potential use of metal-organic framework for hydrogen storage. *Int J Hydrogen Energy* **46**, 11782–11803 (2021).

47. Grünker, R. *et al.* A new metal-organic framework with ultra-high surface area. *Chemical Communications* **50**, 3450–3452 (2014).

48. Lim, D. W., Yoon, J. W., Ryu, K. Y. & Suh, M. P. Magnesium nanocrystals embedded in a metal-organic framework: Hybrid hydrogen storage with synergistic effect on physi- and chemisorption. *Angewandte Chemie - International Edition* **51**, 9814–9817 (2012).

49. Gómez-Gualdrón, D. A. *et al.* Evaluating topologically diverse metal-organic frameworks for cryo-adsorbed hydrogen storage. *Energy Environ Sci* **9**, 3279–3289 (2016).

50. Bambalaza, S. E., Langmi, H. W., Mokaya, R., Musyoka, N. M. & Khotseng, L. E. Experimental Demonstration of Dynamic Temperature-Dependent Behavior of UiO-66 Metal-Organic Framework: Compaction of Hydroxylated and Dehydroxylated Forms of UiO-66 for High-Pressure Hydrogen Storage. *ACS Appl Mater Interfaces* **12**, 24883–24894 (2020).

51. Sumida, K. *et al.* Hydrogen storage and carbon dioxide capture in an iron-based sodalite-type metal-organic framework (Fe-BTT) discovered via high-throughput methods. *Chem Sci* **1**, 184–191 (2010).

52. Xia, L. & Liu, Q. Adsorption of H2 on aluminum-based metal-organic frameworks: A computational study. *Comput Mater Sci* **126**, 176–181 (2017).

53. Orcajo, G. *et al.* Li-Crown ether complex inclusion in MOF materials for enhanced H2 volumetric storage capacity at room temperature. *Int J Hydrogen Energy* **4**, 19285–19293 (2019).

54. Furukawa, H., Miller, M. A. & Yaghi, O. M. Independent verification of the saturation hydrogen uptake in MOF-177 and establishment of a benchmark for hydrogen adsorption in metal-organic frameworks. *J Mater Chem* **17**, 3197–3204 (2007).

55. Panella, B., Hirscher, M., Pütter, H. & Müller, U. Hydrogen adsorption in metal-organic frameworks: Cu-MOFs and Zn-MOFs compared. *Adv Funct Mater* **16**, 520–524 (2006).

56. Bordiga, S. *et al.* Adsorption properties of HKUST-1 toward hydrogen and other small molecules monitored by IR. *Physical Chemistry Chemical Physics* **9**, 2676–2685 (2007).

57. Lin, K. S., Adhikari, A. K., Ku, C. N., Chiang, C. L. & Kuo, H. Synthesis and characterization of porous HKUST-1 metal organic frameworks for hydrogen storage. *Int J Hydrogen Energy* **37**, 13865–13871 (2012).

58. Murray, L. J., Dinca, M. & Long, J. R. Hydrogen storage in metal-organic frameworks. *Chem Soc Rev* **38**, 1294–1314 (2009).

59. Hirscher, M. & Panella, B. Hydrogen storage in metal-organic frameworks. *Scr Mater* **56**, 809–812 (2007).

60. Saha, D., Wei, Z. & Deng, S. Equilibrium, kinetics and enthalpy of hydrogen adsorption in MOF-177. *Int J Hydrogen Energy* **33**, 7479–7488 (2008).

61. Furukawa, H. *et al.* Ultrahigh porosity in metal-organic frameworks. *Science (1979)* **329**, 424–428 (2010).

62. Farha, O. K. *et al.* Metal-organic framework materials with ultrahigh surface areas: Is the sky the limit *J Am Chem Soc* **134**, 15016–15021 (2012).

63. Hönicke, I. M. *et al.* Balancing Mechanical Stability and Ultrahigh Porosity in Crystalline Framework Materials. *Angewandte Chemie - International Edition* **57**, 13780–13783 (2018).

64. Wong-Foy, A. G., Matzger, A. J. & Yaghi, O. M. Exceptional H2 saturation uptake in microporous metal-organic frameworks. *J Am Chem Soc* **128**, 3494–3495 (2006).

65. Chen, Z. *et al.* Balancing volumetric and gravimetric uptake in highly porous materials for clean energy. *Science (1979)* **368**, 297–303 (2020).

66. Ahmed, A. *et al.* Balancing gravimetric and volumetric hydrogen density in MOFs. *Energy Environ Sci* **10**, 2459–2471 (2017).

67. Livingston, H. K. The cross-sectional areas of molecules adsorbed on solid surfaces. *J Colloid Sci* **4**, 447–458 (1949).

68. Hirscher, M. *et al.* Materials for hydrogen-based energy storage – past, recent progress and future outlook. *J Alloys Compd* **827**, (2020).

69. Balderas-Xicohténcatl, R. *et al.* Formation of a super-dense hydrogen monolayer on mesoporous silica. *Nat Chem* (2022) doi:10.1038/s41557-022-01019-7.

2. Purpose

The H_2 adsorption storage using porous materials have long been studied. It is well known that the H_2 capacity strongly depends on the specific surface area of porous materials. Therefore, the main efforts of this research field have been the development of porous materials to increase the specific surface area, such as porous carbon materials and MOFs. However, in recent years, the improvement of H_2 adsorption capacity seems to be stagnating due to the limit of the material development to obtain a higher specific surface area. Most of previous researches have been focused on H_2 adsorption capacity at the boiling point of N_2 (77 K), which is higher than the boiling point of H_2 (20.4 K). Meanwhile, in this study carried out at 20.4 K, the "super-dense H_2 adsorption" with a higher density of adsorbed H_2 compared with that of bulk-liquid and solid H_2 was reported. This result is contrary to the general understanding that the upper limit of adsorbed H_2 density is equivalent to the density of liquid H_2. The super-dense H_2 adsorption is expected to lead to further enhancement of H_2 adsorption capacity from the practical point view and further understanding of physical properties of the adsorbed H_2 from the academic point of view. However, the reports about super-dense H_2 adsorption are still few, and the details of the super-dense H_2 have not been understood well.

In this thesis, the factors leading to the super-dense H_2 adsorption under the cryogenic condition were discussed from the following point of view. In addition, for the H_2 storage as liquid phase, the feasibility about suppression of boil-off by using the H_2 adsorption phenomena on porous materials was discussed.

1) Material dependence

In the previous studies, the super-dense H_2 adsorption was reported on only a few materials, and the material dependences were not understood well. In this work, various kind of

materials, such as the carbon materials, MOFs, and other porous materials, were used for the adsorption tests at the boiling point of H_2 (20.4 K). The influence of different material species, specific surface area, and pore structure, for the density of super-dense H_2 were investigated.

2) Temperature dependence

The super-dense H_2 adsorption has been observed only at the boiling point of H_2 (20.4 K) in previous studies. In this work, the temperature dependence of the super-dense H_2 density was investigated below the critical point of H_2 (33 K). In addition, the feasibility of suppression for liquid H_2 boil-off was discussed by using the effect of super-dense H_2 on porous materials.

3) Adsorbed layer dependence

Molecules of adsorbates can be divided into the two types; molecules adsorbed just on the material surface (monolayer) and molecules adsorbed on adsorbates (multilayer). Analysis methods to distinguish between the monolayer and multilayer adsorption have been established based on the BET theory, which is explained next section in detail, and the densities of monolayer and multilayer H_2 were independently evaluated in order to discuss the adsorption state in furhter detail.

4) Gas dependence

The phenomenon of the super-dense adsorption has been investigated only for H_2 under cryogenic condition so far. In order to understand the gas dependence of the super-dense adsorption state, the densities of deuterium (D_2), neon (Ne), and nitrogen (N_2) on the carbon materials were investigated at the boiling points 23.6, 27.1, and 77.1 K, respectively.

3. Theory and Experiments

3.1 Theory of gas adsorption on solid surface

3.1.1. Van der Waals Forces

Van der Waals force is a weak intermolecular force existing between molecules and surfaces due to dipolar interactions. The van der Waals force is usually categorized three different types of interactions; Keesom interaction, Debye interaction, and London dispersion interaction as summarized in Fig. 3.1.1. The Keesom interaction and Debye interaction are based on electrostatic mechanisms. The Keesom interaction arises from the interaction between two permanent dipoles, which is a so-called orientation force. The Debye interaction arises from a molecule with a permanent dipole, inducing charge redistribution to neighboring molecules with no dipole moments, which is a so-called induction force. The London dispersion interaction is most widely known as the van der Waals interaction based on two molecules without permanent dipole. The electron cloud in the atom can yield an instantaneous dipole, and it can induce a dipole to neighboring molecules. The induced dipoles are weakly attracted to another molecule by the dispersion force. The strength of the London dispersion force increases with the number of electrons in the molecules. The potential energy of the van der Waals force (V_{vdW}) is given by

$$V_{\mathrm{vdW}} = -\frac{C_{\mathrm{vdW}}}{r^6}, \qquad \text{where } C_{\mathrm{vdW}} = C_{\mathrm{orient}} + C_{\mathrm{ind}} + C_{\mathrm{disp}} \tag{3.1.1}$$

where C_{vdW}, C_{orient}, C_{ind}, and C_{disp} are constants for each interaction, and r is the distance between two molecules. The potential energy decreases with $1/r^6$. The interaction between H_2 molecules and a solid surface is basically dominated by this London dispersion interactions.

Lennard-Jones potential

Lennard-Jones potential is described as the total potential of repulsion and attraction on the van der Waals force as a function of the distance between molecules. This is a typical model to explain the interactions between molecules. The potential of V_{LJ} is given by

$$V_{\mathrm{LJ}} = 4\varepsilon\left\{\left(\frac{\sigma_0}{r}\right)^{12} - \left(\frac{\sigma_0}{r}\right)^{6}\right\} \tag{3.1.2}$$

where ε corresponds to minimum potential, and σ_0 is the value of the distance (r) when V_{LJ} is zero. When $r = 2^{1/6}\sigma_0$, V_{LJ} shows a minimum value of ε. Table 3.1.1 shows the parameters of ε/k_B for each species of molecule, where k_B is Boltzmann constant, and the Lennard-Jones potential between H_2-H_2 molecule is calculated and shown in Fig. 3.1.2. The attraction term of $1/r^6$ is basically given by the London dispersion force. The repulsive term of $1/r^{12}$ is the Pauli repulsion due to the overlapping electron orbitals.

Table. 3.1.1 Parameters of Lennard-Jones potential (ε/k_B and σ_0).[1]

Species	ε/k_B (K)	σ (A°)
He	10.22	2.56
Ne	35.6	2.75
Ar	120	3.40
Kr	171	3.60
Xe	220	4.10
N_2	95.5	3.74
CH_4	148.4	3.81
CF_4	151.4	4.75
H_2	39.4	2.81
O_2	118	3.58
CO	100	3.76
CO_2	309	3.36
C_2H_4	470	2.5
C_2H_6	243	3.95
C_3H_8	242	5.64
$C(CH_3)_4$	232	7.44
C_6H_6	830	3.4
C_6H_6–CH_4O	1018.2	2.896
C_6H_6–C_2H_6O	553.5	4.651
C_6H_6–C_3H_6O	632.1	4.620
C_6H_6–$C_4H_{10}O$	1122.3	3.425

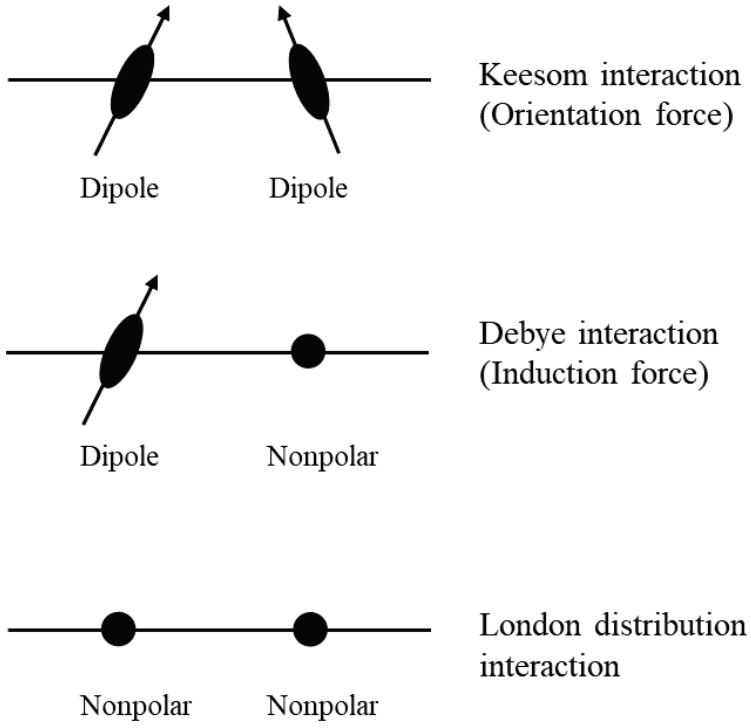

Fig. 3.1.1 Types of van der Waals forces (Keesom interaction, Debye interaction, London distribution interaction).[2]

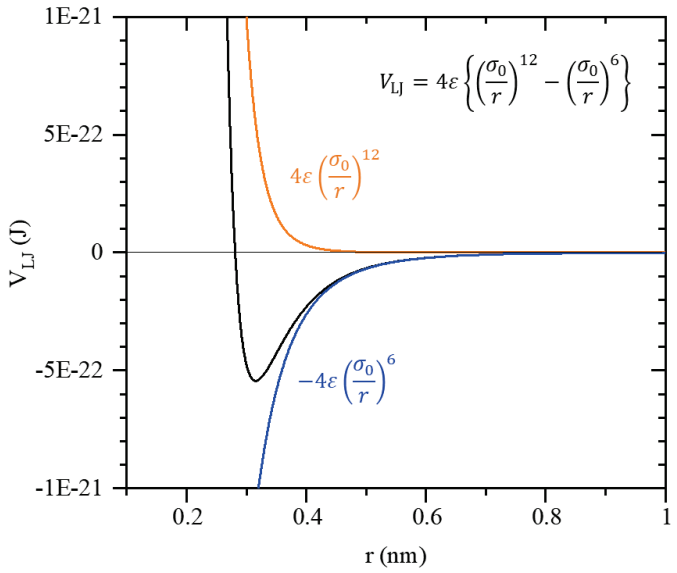

Fig. 3.1.2 Lennard-Jones potential (V_{LJ}) for H_2-H_2 molecules. Blue curve is the attraction term of $-4\varepsilon\left(\frac{\sigma_0}{r}\right)^6$, Orange curve is the repulsive term of $4\varepsilon\left(\frac{\sigma_0}{r}\right)^{12}$.

3.1.2. Langmuir and BET theory

Langmuir theory

The Langmuir adsorption model is the simplest model representing the monolayer adsorption between adsorbates and adsorbents. This adsorption model was proposed by Irving Langmuir in 1918.[3] The Langmuir adsorption model is based on the assumptions as shown below.

Assumptions of Langmuir theory

1. Gas molecules behave ideally
2. Only monolayer forms
3. All adsorption sites on the surface are equivalent
4. There are no interactions between adsorbate - adsorbate
5. Adsorbed molecules are immobile

The Langmuir equation is given based on the above assumptions, and it is derived below. The rate of adsorption (v_a) and desorption (v_b) are described as

$$v_a = apS \tag{3.1.3}$$

$$v_b = bA, \tag{3.1.4}$$

where a and b are constants of adsorption and desorption reaction, p is the partial pressure of the adsorbate, S is the number of free sites on the surface, and A is the number of sites occupied by adsorbate on the surface. Both rate of v_a and v_b should be equal in the equilibrium state and the equation 3.1.3 and 3.1.4 give

$$\frac{A}{pS} = \frac{a}{b} = K, \tag{3.1.5}$$

where K is the equilibrium constant. The total number of sites (S_0) is given by

$$S_0 = S + A = \frac{A}{Kp} + A = \frac{1 + Kp}{Kp} A \tag{3.1.6}$$

Since the fraction of the occupied sites, i.e., the fractional coverage, on the surface (θ_A) can be given as

$$\theta_A = \frac{A}{S_0}, \tag{3.1.7}$$

the Langmuir equation is given by

$$\theta_A = \frac{Kp}{1 + Kp} \tag{3.1.8}$$

Fig. 3.1.4 shows the Langmuir isotherm for different values of K. The different values of K give the different isotherms. The fractional coverage increases and approaches 1 with increasing pressure.

BET theory

The BET theory is widely used to determine the specific surface area dealing with multilayer adsorption, which is developed by Stephen Brunauer, Paul Emmett, and Edward Teller in 1938.[4] The BET model is an extension of Langmuir model based on the following assumptions.

Assumptions of BET theory

1. The surface is homogeneous (All sites are equivalent)
2. Gas molecules behave ideally
3. Multilayers can be formed on each site infinitely
4. After first layer, each molecule provides adsorption site for next layer
5. The Langmuir theory can be applied to each layer
6. Adsorbed molecules are immobile
7. Gas molecules only interact with adjacent layers
8. There are no lateral interaction between molecules

9. The enthalpy of adsorption for the first layer is constant for all sites
10. Adsorbate molecules in the second and higher layers are assumed as liquid and they have the same enthalpy of liquefaction

The image of BET adsorption model is illustrated in Fig. 3.1.5. The BET equation is derived based on the assumption in the following paragraph.

In the multilayer adsorption with 0, 1, 2 … i … layers, the number of adsorption site is represented s_0, s_1, s_2 … s_i, … for each layer. At equilibrium state of the adsorption, the rate of adsorption on $(i-1)$ layer is equal to the evaporation from i layer. Since the rate of adsorption (v_a) on the layer i is proportional to the pressure (p) of adsorbate and the number of sites on the layer $(i-1)$, therefore v_a is given by

$$v_a = a_i p s_{i-1}, \tag{3.1.9}$$

where a_i is a rate constant. Since the rate of evaporation from layer i (v_b) is proportional to the number of sites on layer i and exp $(-E_i/RT)$, so v_b is given by

$$v_b = b_i s_i \exp\left(-\frac{E_i}{RT}\right), \tag{3.1.10}$$

where b_i is a rate constant, E_i is the heat of adsorption on layer i, R is the gas constant, and T is a temperature. Thus, both rate of v_a and v_b should be equal, and the equation 3.1.9 and 3.1.10 give

$$a_i p s_{i-1} = b_i s_i \exp\left(-\frac{E_i}{RT}\right) \tag{3.1.11}$$

Here, the total number of adsorbed molecules (N) and the number of monolayer sites (N_m) on an adsorbent are given by

$$N = \sum_i i s_i \tag{3.1.12}$$

$$N_m = \sum_i s_i \tag{3.1.13}$$

Considering the assumption (10) of "Adsorbate molecules in the second and higher layers are

assumed as liquid and they have the same enthalpy of liquefaction", it gives

$$E_i = E_L \qquad (i \geq 2) \tag{3.1.14}$$

$$\frac{b_i}{a_i} = g = \text{constant} \qquad (i \geq 2), \tag{3.1.15}$$

where E_L is the heat of liquefaction. Now, the number of site (s_1, s_2 … s_i) can be expressed by only using s_0.

$$s_1 = ys_0, \text{where } y = (a_1/b_1)p \cdot \exp(E_1/\mathrm{R}T) \tag{3.1.16}$$

$$s_2 = xs_1, \text{where } x = (p/g)\exp(E_L/\mathrm{R}T) \tag{3.1.17}$$

$$s_3 = xs_2 = x^2 s_1 \tag{3.1.18}$$

$$s_i = xs_{i-1} = x^{i-1}s_1 = yx^{i-1}s_0 = cx^i s_0, \text{where } c = \frac{y}{x} = \frac{a_1 g}{b_1}\exp((E_1 - E_L)/\mathrm{R}T) \tag{3.1.19}$$

Inserting equation (3.1.19) into equation (3.1.12), it is given by

$$N = cs_0 \sum_{i=i}^{\infty} i\, x^i = \frac{cs_0 x}{(1-x)^2}, \tag{3.1.20}$$

Inserting equation (3.1.19) into equation (3.1.13), it is given by

$$N_m = s_0 \left\{1 + c\sum_{i=i}^{\infty} x^i\right\} = s_0\left(1 + \frac{cx}{1-x}\right) \tag{3.1.21}$$

In equation 3.1.20 and 3.1.21, the sum of an infinite geometric progression is expressed by

$$\sum_{i=i}^{\infty} x^i = \frac{x}{1-x} \tag{3.1.22}$$

$$\sum_{i=i}^{\infty} i\, x^i = x\frac{\mathrm{d}}{\mathrm{dx}}\sum_{i=i}^{\infty} x^i = \frac{x}{(1-x)^2} \tag{3.1.23}$$

Therefore, equations 3.1.20 and 3.1.21 are changed to

$$\frac{N}{N_m} = \frac{cx}{(1-x)(1-x+cx)} \tag{3.1.24}$$

In this adsorption model, it is assumed that the number of layers can accumulate to infinity at the saturation pressure (p_0). When $N = \infty$ at $p = p_0$, x must be equal to 1, and equation 3.1.17 can be expressed by

$$\left(\frac{p_0}{g}\right)\exp\left(\frac{E_L}{\mathrm{RT}}\right) = 1, \text{and} \quad x = \frac{p}{p_0} \tag{3.1.25}$$

Inserting equation (3.1.25) into equation (3.1.24), the BET equation is given by

$$\frac{p/p_0}{N(1-p/p_0)} = \frac{1}{N_m c} + \frac{(c-1)}{N_m c} \cdot p/p_0 \tag{3.1.26}$$

Fig. 3.1.6 shows the BET isotherms for different values of c, which is large when the enthalpy of desorption from a monolayer is large compared with the enthalpy of vaporization of the liquid phase. The value of N/N_m increases infinitely with increasing pressure because there is no limit of the multiple adsorbed layers.

BET surface area

The BET surface area is evaluated by the amount of monolayer molecules on the BET adsorption model. An experimentally measured adsorption isotherm can be fitted by the BET equation 3.1.26, and the value of a slope ($(c-1)/N_m c$) and an intercept ($1/N_m c$) can be obtained in the BET plot. Usually, the fitting of BET plot is applied in the relative pressure range of 0.03-0.35. The BET plot gives the amount of monolayer molecule (N_m: mol/g), and the BET surface area (SSA) of adsorbents can be evaluated by

$$SSA = \sigma \times N_m \times N_A \tag{3.1.27}$$

where σ is the cross-sectional area (Å^2/molecule). Usually, N_2 is used for the BET method and the cross-sectional area of N_2 is 16.2 Å^2/molecule. Typically, the cross-sectional area can be evaluated by equation 3.1.26 based on two assumptions, which are (1) the density of adsorbate is regarded as bulk-liquid density; (2) adsorbates form a hexagonal- close-packed layer.[5]

$$\sigma = F\left(\frac{M}{N_A \cdot \rho}\right)^{2/3} \tag{3.1.28}$$

where M (g/mol) is the molar mass of molecule, ρ is the density of bulk-liquid phase, F is the packing factor. $F = 1.091$ is well used as the hexagonal close-packed factor. [5]

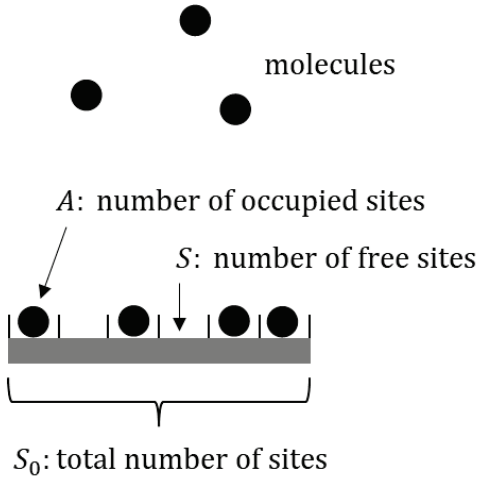

Fig. 3.1.3 Image of Langmuir adsorption model.

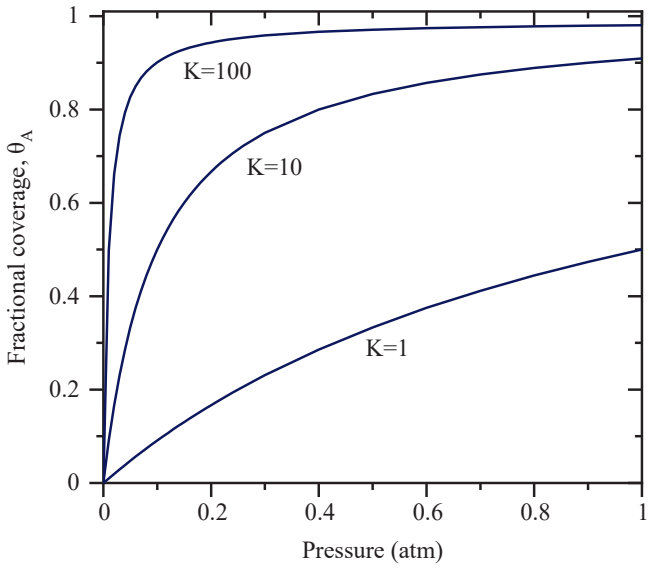

Fig. 3.1.4 Langmuir isotherms for different values of *K*.

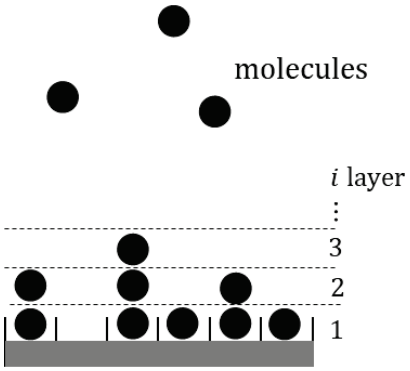

Fig. 3.1.5 Image of BET adsorption model.

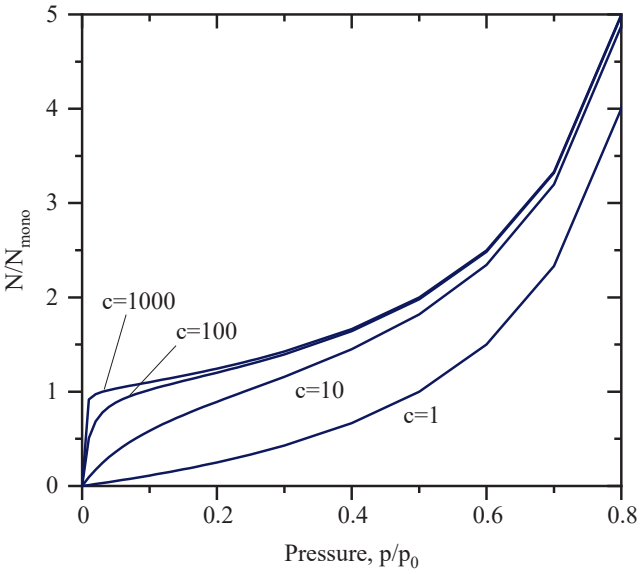

Fig. 3.1.6 BET isotherms for different values of c.

3.1.3. Adsorption isotherms

Type of adsorption isotherms

Adsorption properties are usually investigated by adsorption isotherms which is the plot of adsorbed amounts as a function of the pressure. It is well known that the shape of adsorption isotherms is related to a pore structure of adsorbents. In 1985, an International Union of Pure and Applied Chemistry (IUPAC) technical report[6] was published, and typical adsorption isotherms were classified to six types as shown in Fig. 3.1.7. According to the report, the pore structures are defined as

i) Pores with widths exceeding about 50 nm; ***macropores***

ii) Pores of widths between 2 nm and 50 nm; ***mesopores***

iii) Pores with widths not exceeding about 2 nm; ***micropores***

Type I shows a steep uptake at very low pressure, and the uptake approaches to a saturated value with increasing pressure. This is due to a microporous material, where micropores enhance the interaction between adsorbates and adsorbents. The saturated uptake is governed by the micropore volume rather than the external surface area. Especially, Type I(a) isotherm represents the typical microporous materials with mainly narrow micropores less than 1 nm. Type I(b) isotherms are given by materials with pore size distributions including wider micropores and narrow mesopores (<2.5 nm).

Type II isotherms are given by microporous or nonporous materials. The end point of steep uptake at low pressure, which is called “B-point”, corresponds to the completion of monolayer coverage, and after that, the uptake gradually increases by multilayer adsorption.

Type III isotherms doesn’t show the B-point, i.e., the monolayer adsorption is not observable. The interactions between adsorbent and adsorbate are relatively weak, and then the heats of adsorption are less than the heat of liquefaction of the adsorbate. The additional adsorption on an

adsorbed layer proceeds because the heat of additional adsorption is greater than the adsorption on the material surface.

Type IV isotherms are shown by mesoporous adsorbents. The initial adsorption step corresponds to the path of Type II isotherm on mesopore wall, and the final saturation plateau correspond the complete filling of the pore. The typical feature of Type IV(a) is the hysteresis loop in the final step, which is associated with capillary condensation in the mesopores. This phenomenon occurs when the pore size exceeds a certain size, which depends on the adsorption system and temperature. When the pore size is smaller than the certain size, Type IV(b) isotherms are obtained with completely reversible loop.

Type V isotherm in the low-pressure range is similar to that of Type III without the B-point, because of the relatively weak adsorbent–adsorbate interactions. In the high pressure, the shape is similar to that of Type IV.

Type VI isotherm is representative of layer-by-layer adsorption on a highly uniform nonporous surface, such as a graphitized carbon

Quantitative definitions of adsorption

The adsorption isotherm represents the amount of adsorbate on the adsorbent surface as a function of the pressure of the gas, and it is usually measured by volumetric method described later in the section 3.3.1 "Principle of volumetric apparatus". The experimental method doesn't directly measure the real amount of adsorbate because it is difficult to define the boundaries between the adsorbate and free gas. In general, there are four concepts to express the amount of adsorbed gas (uptake) on adsorbents, which are "Net", "Excess", "Absolute", and "Total" uptake as illustrated in Fig. 3.1.8.

In the concept of "Net" uptake (n_{net}), the amount of molecules with higher density than free-gas in the cell is counted, i.e., the amount of free-gas in the cell volume (V_{cell}) is subtracted from the total introduced amount into the cell (n_{intro}), corresponding to "A − D" in Fig. 3.1.8. Therefore, n_{net} is given by

$$n_{net} = n_{intro} - \rho_{gas} V_{cell} \tag{3.1.29}$$

where ρ_{gas} is the density of gaseous adsorbate. In the concept of "Excess" uptake (n_{ex}), the amount of molecules with higher density than that of free-gas in the free volume (V_{free}) is counted, i.e., the amount of free-gas in the free volume is subtracted from the total introduced amount, corresponding to "A" in Fig. 3.1.8. Therefore, n_{ex} is given by

$$n_{ex} = n_{intro} - \rho_{gas} V_{free}, \qquad \text{where } V_{free} = V_{cell} - V_{sk} \tag{3.1.30}$$

In the concept of "Absolute" uptake (n_{abs}), the adsorbed amounts in the volume V_{ads} is counted, corresponding to "A + B" in Fig. 3.1.8, and n_{ads} is given by

$$n_{ads} = n_{intro} - \rho_{gas}\left(V_{free} - V_{ads}\right), \qquad \text{where } V_{ads} = \frac{n_{ads}}{\rho_{ads}} \tag{3.1.31}$$

In the concept of "Total" uptake, the amount of molecules in the free volume is counted, corresponding to "A + B + C" in Fig. 3.1.8, and n_{tot} is given by

$$n_{tot} = n_{ex} + \rho_{gas}(V_{cell} - V_{sk}) \tag{3.1.32}$$

In this study, the adsorbed uptake was evaluated as “Absolute” uptake. To discuss the gravimetric capacity for each adsorbent, n_{ads} was represented as the gravimetric units of “wt.%” and “mmol/g”

$$n_{\mathrm{wt.\%}}\,[\mathrm{wt.\%}] = \frac{n_{ads}\, m_{mole}}{m + n_{ads}\, m_{mole}} \times 100 \tag{3.1.33}$$

$$n_{\mathrm{mmol/g}}\,[\mathrm{mmol/g}] = \frac{{}^{n_{ads}}/_{1000}}{m}, \tag{3.1.34}$$

where m is the mass of materials, and m_{mole} is the molar mass of gases.

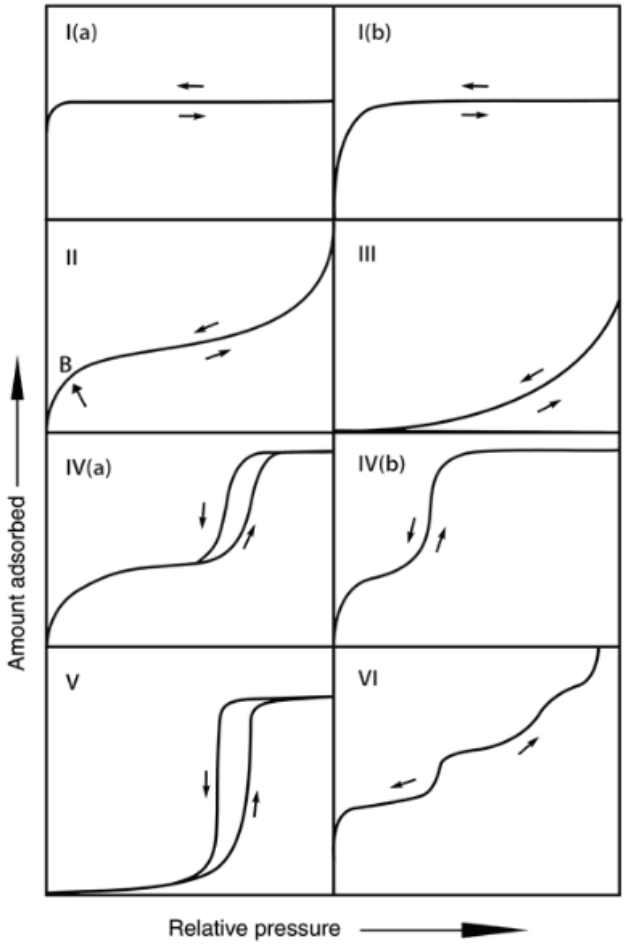

Fig. 3.1.7 IUPAC classification of adsorption isotherms.[6]

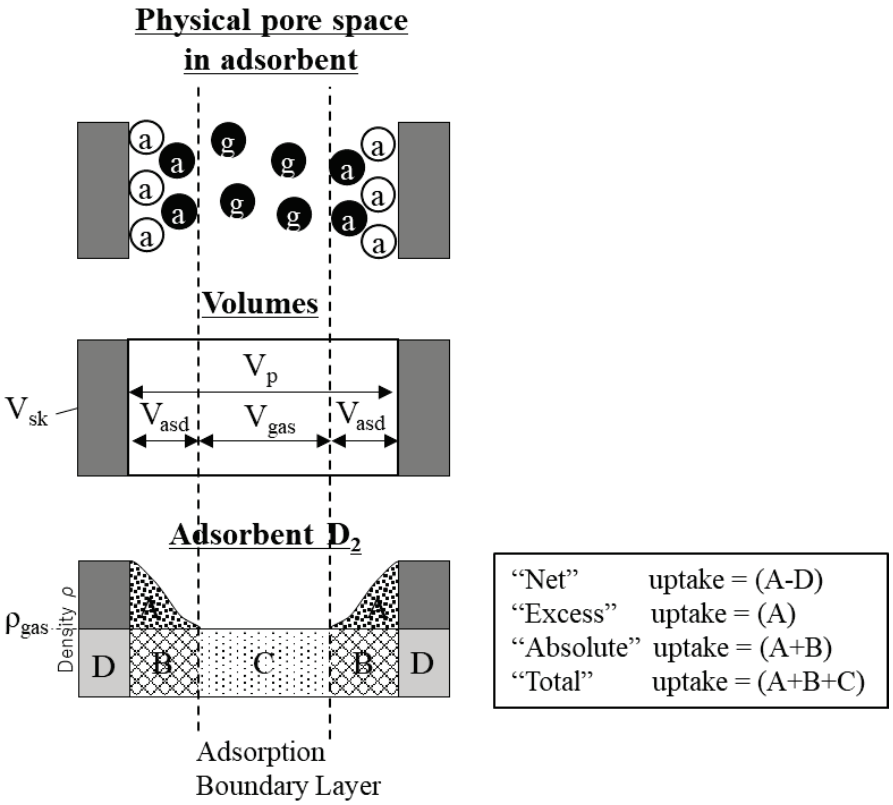

Fig. 3.1.8 Concept of "Net", "Excess", "Absolute" and "Total" adsorption capacities,[7] where Open and solid dots of "**a**" are "Excess adsorbed molecule" and "Adsorbed molecule normally present in gas phase", respectively; solid dots of "**g**" is "Bulk gas molecule"; V_{sk} is the skeletal volume of material; V_{ad} is the volume of adsorbate; V_p is the pore volume; V_{gas} is the volume of bulk-gas; ρ_{gas} is the density of bulk-gas; region of "**A**" corresponds to "Excess adsorbent"; region of "**B**" corresponds to "Adsorbed molecule normally present in the gas phase"; region of "**C**" is "Bulk gaseous molecule"; region of "D" is "Free gas that would occupy V_{sk}.

3.1.4. Isosteric heat of adsorption

Clausius-Clapeyron equation

Clausius-Clapeyron equation describes a characteristic of phase boundaries, i.e., the solid-liquid boundary and the vapor-liquid boundary. In this study, the Clausius-Clapeyron equation was applied into the adsorption isotherms representing the properties of the adsorbed-vapor phase boundary, and the heat of adsorption was evaluated on adsorbents.

In order to derive the Clausius-Clapeyron equation, two phases α and β are considered in an equilibrium condition at temperature (T) and pressure (P). Since the free energies (G) of both phases are equal, it is expressed as

$$G_\alpha(T,P) = G_\beta(T,P) \tag{3.1.35}$$

Based on the principles of thermodynamics, the variations of free energy with temperature and pressure are given as

$$dG_\alpha = V_\alpha dP - S_\alpha dT \tag{3.1.36}$$

$$dG_\beta = V_\beta dP - S_\beta dT \tag{3.1.37}$$

When the equilibrium pressure and temperature change from P to $P + \Delta P$ and from T to $T + \Delta T$, respectively, equation 3.1.35 can be given by

$$G_\alpha(T + \Delta T, P + \Delta P) = G_\beta(T + \Delta T, P + \Delta P) \tag{3.1.38}$$

$$(G_\alpha + dG_\alpha) = (G_\beta + dG_\beta) \tag{3.1.39}$$

Inserting equation 3.1.35 into equation 3.1.39, the equation 3.1.39 is transformed into

$$dG_\alpha = dG_\beta \tag{3.1.40}$$

According to equation 3.1.36 and equation 3.1.37, equation 3.1.40 is transformed into

$$V_\alpha dP - S_\alpha dT = V_\beta dP - S_\beta dT \tag{3.1.41}$$

$$\frac{dP}{dT} = \frac{S_\beta - S_\alpha}{V_\beta - V_\alpha} \tag{3.1.42}$$

When ΔH is the heat of phase transformation at a temperature, the entropy change (dS) can be

described as

$$dS = S_\beta - S_\alpha = \frac{\Delta H}{T} \tag{3.1.43}$$

Finally, the Clausius-Clapeyron equation is given by inserting equation (3.1.43) into (3.1.42)

$$\frac{dP}{dT} = \frac{\Delta H}{T(V_\beta - V_\alpha)} \tag{3.1.44}$$

Considering the gas adsorption on solid surface, the α and β phases are defined as the adsorbed phase and the gaseous phase, respectively. In this case, the volume of gaseous phase is much larger than that of adsorbed phase ($V_{gas} \gg V_{ads}$), so equation 3.1.44 is transformed into

$$\frac{dP}{dT} = \frac{\Delta H_{ads}}{TV_{gas}} = \frac{\Delta H_{ads}}{T\frac{RT}{P}}, \qquad \text{where } V_{gas} = \frac{RT}{P} \tag{3.1.45}$$

and,

$$\frac{dP}{P} = \frac{\Delta H_{ads}}{R}\frac{dT}{T^2} \tag{3.1.46}$$

When the equilibrium pressure and the temperature change from P_1 to P_2 and from T_1 to T_2, respectively, equation 3.1.46 is expressed as

$$\int_{P_1}^{P_2} \frac{dP}{P} = \frac{\Delta H_{ads}}{R}\int_{T_1}^{T_2} \frac{dT}{T^2} \tag{3.1.47}$$

$$\ln\frac{P_2}{P_1} = \frac{\Delta H_{ads}}{R}\left(\frac{1}{T_1} - \frac{1}{T_2}\right) \tag{3.1.48}$$

Finally, the Clausius-Clapeyron equation for evaluating the heat of adsorption is derived in equation 3.1.48.

Procedure of evaluation of heat adsorption

The adsorption isotherms measured at different temperatures were used to evaluate the heat of adsorption. Fig. 3.1.9 shows the typical isotherms measured at different temperature of T_1 and T_2. The equilibrium pressures of $P_{T_1}(A)$ and $P_{T_2}(A)$, corresponding to a certain adsorbed amount (n_A), were defined as shown in Fig. 3.1.9. By substituting these values (T_1, T_2, $P_{T_1}(A)$ and $P_{T_2}(A)$,) into equation 3.1.48, the heat of adsorption at a certain adsorbed amount was evaluated. The heat of adsorption for different adsorbed amount was evaluated, and the relationship between the adsorbed amount and the heat of adsorption for each adsorbent was shown in the result section of Fig. 4.3.2.

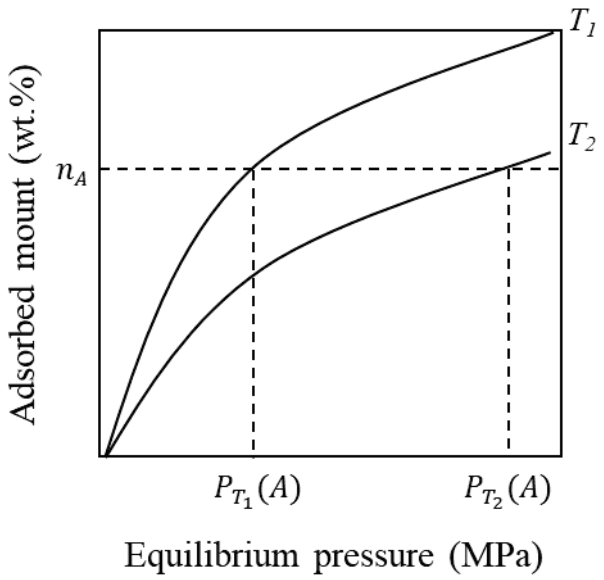

Fig. 3.1.9 Schematic drawing the equilibrium pressures (P) at two temperatures (T_1>T_2) with a certain adsorbed amount (n_A) on an adsorbent.

3.2 Materials

Various materials were used as the adsorbents in this study, and the information of materials were listed in Table. 3.2.1. Prior to the measurement, all adsorbents were degassed at 200 ºC for 12 h under dynamic vacuum condition in a stainless tube.

Table 3.2.1 Information of adsorbent materials

Adsorbent		Suplyer	Information for MOFs	
			Metal	Ligand
Crbon	MSC-30	Kansai Coke and Chemicals Co., Ltd		
	GNPs	STREM chemicals (item number: 06-0235)		
MOFs	MOF-177	Sigma-Aldrich (Basolite Z377)	Zn	Benzenetribenzoate
	HKUST-1	Air Liquide Laboratories	Cu	1,3,5-Benzenetricarboxylate
	Fe-Mil-100	Air Liquide Laboratories	Fe	Trimesic acid
	MIL-53	Sigma-Aldrich (Basolite A100)	Al	Terephthalate
	ZIF-8	Sigma-Aldrich (Basolite Z1200)	Zn	2-Methylimidazolate
Silica gel	Wakogel C-300	FuJIFILM Wako		
	Aerogel	Air Liquide Laboratories		

Definitions of material's volume and density

In order to perform the volumetric measurement and discuss the volumetric capacity of adsorbates, it is important to understand the definitions of volume and density of materials. There are several concepts to define the volume and density for the material level and the system level as shown in Fig. 3.2.1.[7]

Fig. 3.2.1 (a) shows the materials level definitions, and there are some concepts of density and volume for the porous materials. The pores can be classified as "open" and "closed" pores, which are defined as whether a gas can freely access in the pores. In the actual materials for experiments, there are intermediate pores between open and closed pores because the size of the accessible pores is dependent on the species of gas probe, i.e., the size of the molecule. The absolute or true volume (V_T) is defined as the volume of materials themselves without any pores, and the true density (ρ_T) is described as

$$\rho_T = \frac{m}{V_T}, \tag{3.2.1}$$

where m is the mass of the material. The skeletal volume (V_{sk}) can be defined as the volume occupied by the materials themselves plus the volume of the closed pores, and the skeletal density (ρ_{sk}) can be described as

$$\rho_{sk} = \frac{m}{V_{sk}} \tag{3.2.2}$$

Fig. 3.2.1 (b) shows the systems level definitions of the density and volume. The aggregations of powder materials are packed in a cell, and there is a space between grains due to the imperfect packing. The apparent volume including the space between grains is called a bulk volume (V_{bulk}), and then the bulk density can be described as $\rho_{bulk} = m/V_{bulk}$. The bulk density is easily changed by the packing methods, e.g., tapping, shaking, compression, and making pellets. The cell volume (V_{cell}) is the volume of the inside empty cell without materials. The free volume (V_{free}) is

the cell volume excluding the skeletal volume of materials, described as $V_{free} = V_{cell} - m/\rho_{sk}$, which is also called “Dead volume”.

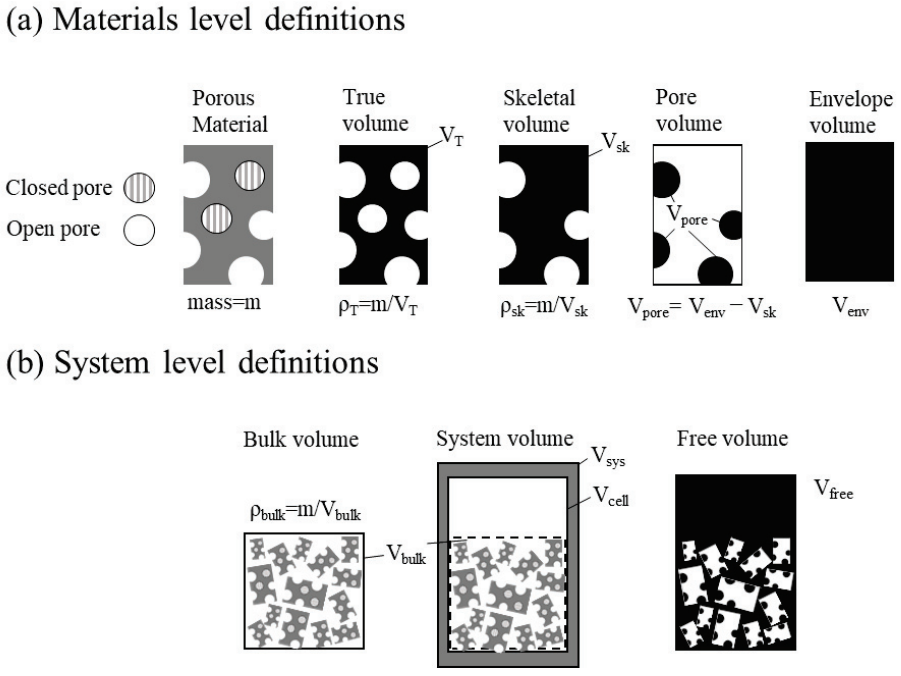

Fig. 3.2.1 Definitions of volume and density for (a) material level and (b) system level

3.3 Experiment and analysis of gas adsorption

3.3.1 Principle of volumetric method by Sievert's apparatus

The volumetric method (known as Sievert's type apparatus) is widely used for the gas sorption measurement to obtain the isothermal curves. In this chapter, the principle of volumetric apparatus is described. Fig. 3.3.1 shows a schematic diagram of a typical Sievert's apparatus composed of a reservoir with a specific volume, gas cylinder, line part, sample cell, and vacuum pump system. The initial gas amount (n) in the system (in the reservoir, line part and sample cell) can be given by

$$n_0 = V_R \cdot \rho(P_0, T_R) + V_L \cdot \rho(P_0, T_L) + \left(V_S - \frac{m}{\rho_{sk}}\right) \cdot \rho(P_0, T_S) \tag{3.3.1}$$

where $V_R, V_L,$ and V_S is the volume of the reservoir, line part, and sample cell, respectively, $T_R, T_L,$ and T_S is the temperature of the reservoir, line part and sample cell, respectively, *ρ(P,T)* is the density of real gas at a certain pressure and temperature, m is the mass of a material in the cell, and ρ_{sk} is the skeletal of density of a material. Thus, $(V_S - m/\rho_{sk})$ represents the free volume of the sample cell.

At the first step, the gas is introduced into the reservoir at pressure of P_1 by opening valve G and closing valve S, and then the gas amount (n_1) in the V_R, V_L and V_S is given by

$$n_1 = V_R \cdot \rho(P_1, T_R) + V_L \cdot \rho(P_0, T_L) + \left(V_S - \frac{m}{\rho_{sk}}\right) \cdot \rho(P_0, T_S) \tag{3.3.2}$$

After opening the valve S (valve G is closed), the pressure changes from P_1 to P_1' in a certain time, due to the gas introduction from the reservoir into the line part and sample cell. The gas amount in the system (n_1') at P_1' can be given by

$$n_1' = V_R \cdot \rho(P_1', T_R) + V_L \cdot \rho(P_1', T_L) + \left(V_S - \frac{m}{\rho_{sk}}\right) \cdot \rho(P_1', T_S) \tag{3.3.3}$$

Therefore, the sorbed gas amount (n_{sorb-1}) can be evaluated by.

$$n_{sorb\_1} = (n_1 - n_1') = \Delta n_1 \tag{3.3.4}$$

At the second step, the sorbed gas amount (n_{sorb_2}) is given by

$$n_{sorb\_2} = n_{sorb\_1} + \Delta n_2 \tag{3.3.5}$$

Repeating the above process by i times, the sorbed gas at the i steps is expressed as

$$n_{sorb\_i} = n_{sorb\_(i-1)} + \Delta n_i \tag{3.3.6}$$

The typical isotherms can be obtained by plotting the relationship between n_{sorb_i} and P_i'.

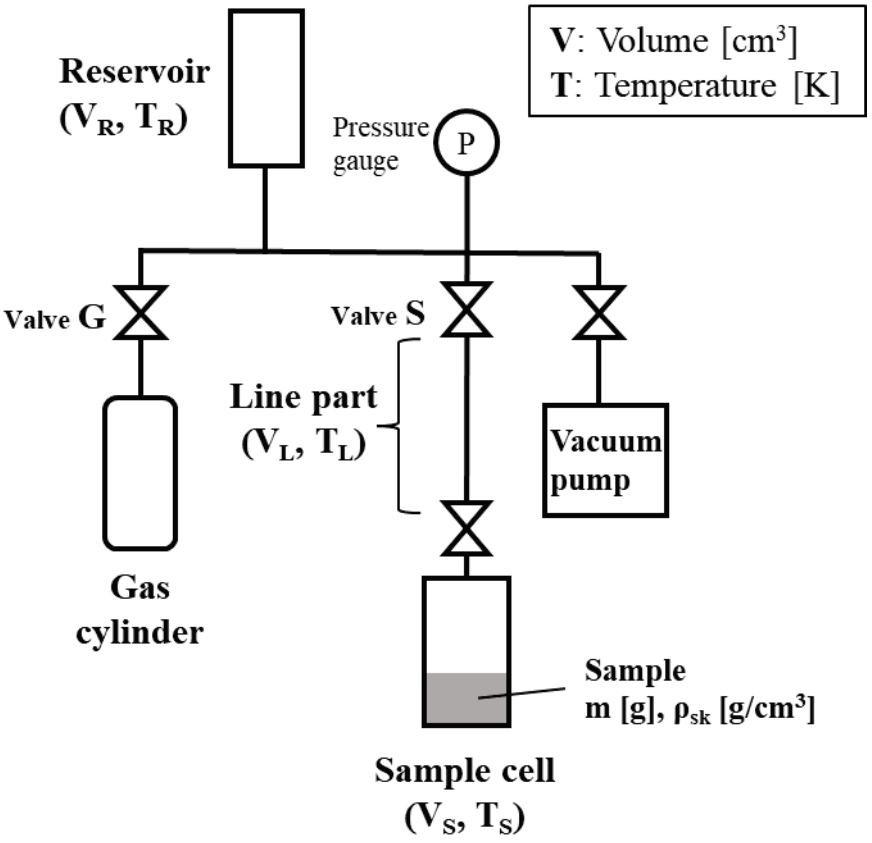

Fig. 3.3.1 Schematic diagram of a typical volumetric apparatus (Sievert's apparatus)

3.3.2 N_2 adsorption isotherms for investigation of textural properties

N_2 adsorption isotherms for all adsorbents were measured by a Sievert's apparatus (Belsorp-max 12N-VP-LTC, Microtrac BEL) at the liquid N_2 temperature (77 K). Fig. 3.3.2 shows the schematic diagram and picture of the experimental system. Prior to the measurement, all adsorbents were heated up to 200 ºC for 12 h under dynamic vacuum condition, and water and other gases on adsorbents were degassed. The degassed adsorbent was put into the sample cell in a globe box filled in high purity Ar gas (>99.9999%), where oxygen level and water level were less than 5 and 2 ppm, respectively. A glass rod was used to reduce the free volume in the sample cell. The two cells with materials and one empty cell (reference cell) were installed as shown in Fig. 3.3.2 because this apparatus allows the measurement for two sample cells at the same time. The free volume of the sample cells was measured by He gas as a non-adsorbing gas at room temperature. After vacuuming the sample cells at room temperature, the cells were put in the dewar vessel with liquid N_2, and the measurement of N_2 adsorption isotherm was carried out in the automatic operation system. An equilibrium pressure was determined when the pressure variation was within 0.1 % in each 5 min period. As the adsorption measurement proceeds, the level of liquid N_2 in the dewar vessel decrease due to the evaporation of liquid N_2. This leads to a change of the cooling volume in the sample cell. The change of cooling volume in the reference cell was measured at each measurement point, it allows a correction of the volume change of the sample cells due to the decrease of the liquid N_2 level in the dewar vessel.The measured N_2 adsorption isotherms give the information about the textural properties of adsorbents, such as the specific surface area, total pore volume, and average of pore diameter, as described below.

Specific surface area

The specific surface area (m^2/g) of each adsorbent was evaluated by applying BET

equation (equation 3.1.26) into the measured N_2 adsorption isotherms. Usually, the results in the relative pressure (p/p_0) range of 0.03-0.35 is used for the BET analysis, however it is not suitable for Type I adsorption attributed to micropores because the monolayer adsorption is completed at lower pressure than $p/p_0 = 0.35$. The appropriate range of p/p_0 for microporous materials were determined by a method proposed by Rouquerol et al,[8] i.e. the p/p_0 range with increasing the value of $n(1 - p/p_0)$ was applied. In this study, the volumetric surface area was defined as the surface area per the skeletal volume of the material, and it was evaluated to multiply the gravimetric surface area by the skeletal density.

Total pore volume

The specific total volume was evaluated by

$$V_p = n\rho_L \tag{3.2.7}$$

where n is the amount of adsorbate at $p/p_0 = 0.99$, ρ_L is the density of liquid for the adsorbate.

Average pore diameter

The average of pore diameter was evaluated by considering the total pore volume as the cylindrical shape of pore. The total volume (V_p) and the surface area (SSA), i.e. the lateral area of the cylindrical pore were given by

$$V_p = \frac{\pi D^2 H}{4} \tag{3.2.8}$$

$$SSA = \pi DH \tag{3.2.9}$$

where H is the height of cylindrical pore and D is the diameter of cylindrical pore, i.e. the average pore diameter. Therefore, the average pore diameter of D was given by

$$D = \frac{4V_p}{SSA} \tag{3.2.10}$$

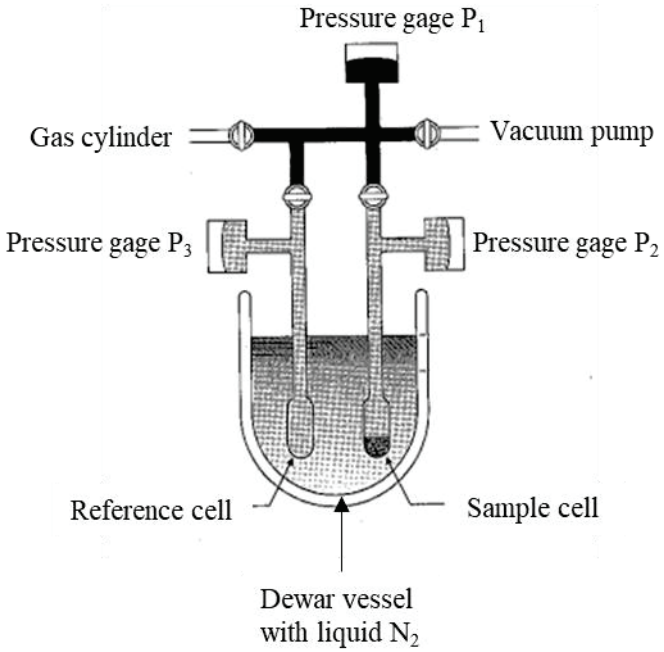

Fig. 3.3.2 Schematic diagram of Sievert's apparatus (Belsorp-max 12N-VP-LTC, Microtrac BEL) for N_2 adsorption measurement

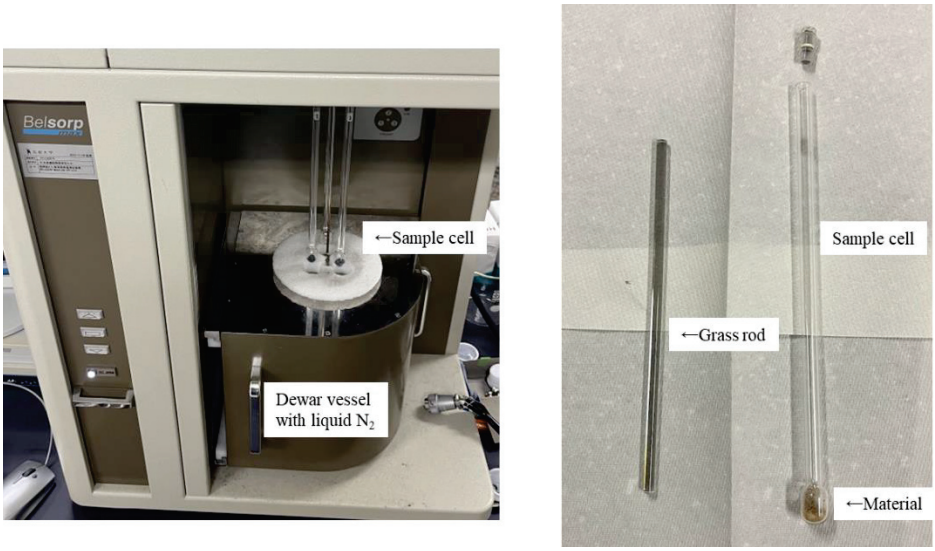

Fig. 3.3.3 Picture of Sievert's apparatus (Belsorp-max 12N-VP-LTC, Microtrac BEL) and sample and sample cell

3.3.3 Measurement of skeletal density

The skeletal densities of all materials were measured by volumetric method using Sievert's apparatus (Belsorp-max 12N-VP-LTC, Microtrac BEL). He gas was used as a non-sorbing gas, and a temperature of the sample cell was maintained at 40 ºC by water bath. At the first step, the volume of the empty cell (V_{cell}) with a glass rod was measured. After that, m (g) of degassed material was put into the sample cell in the grove box, and the free volume of the sample cell (V_{free}) was measured. Finally, the skeletal density of a material was evaluated by

$$\rho_{sk} = \frac{m}{V_{cell} - V_{free}} \tag{3.3.11}$$

It was carried out 6 times, and the average values were shown in the result section for each adsorbent.

3.3.4 Cryogenic adsorption measurement

The cryogenic adsorption measurement was carried out by using the Sievert's type apparatus, which is called Pressure-Composition isothermal (PCI) system, provided by Suzuki Shokan Co., Ltd., and then the sample cell (12.3 cm^3) was cooled by the cryostat system with He cryocooler (C200G) provided by Suzuki Shokan Co., Ltd.. Fig. 3.3.4 and Fig. 3.3.5 show the schematic diagram and pictures of the PCI and the cryostat system. By using this system, the introduced gas amount into the sample cell can be accurately evaluated as following steps: (1). a gas was introduced at desired pressure (P_1) into the reservoir with a specific volume (V_R) which was kept at room temperature (T_R); (2). The valve connected to the sample cell (valve S) was opened, and the gas was introduced into line part and the sample cell from the reservoir. The equilibrium pressure (P_1') was determined when the pressure variation is within 0.01 MPa in each 5-10 min period. (3). The introduced gas amount (n_1) into the line part and the sample cell was evaluated by comparing the gas amount in the reservoir at the pressure of P_1 in the step (1) with that at the pressure P_1' in the step (2), therefore n_1 was given by

$$n_1 = V_R \cdot \rho(P_1, T_R) - V_R \cdot \rho(P_1', T_R) \tag{3.3.12}$$

where the gas density of $\rho(P, T)$ was obtained from the NIST chemistry Web Book;[9] (4). Steps 1-3 were repeated. At the second cycle, the total introduced gas amount was given by

$$n_2 = n_1 + V_R \cdot \rho(P_2, T_R) - V_R \cdot \rho(P_2', T_R) \tag{3.3.13}$$

Subsequently, the total introduced gas amount at the i-th cycle was given by

$$n_i = n_{i-1} + V_R \cdot \rho(P_i, T_R) - V_R \cdot \rho(P_i', T_R) \tag{3.3.14}$$

These cycles were repeated until the pressure in the sample cell was reached up to 1.5 MPa; (5). In order to obtain the introduced gas amount into the sample cell, the introduced gas amount into the line part was evaluated by the measurement of step 1-4 with blind gasket between the line part and the sample cell, and then the result was subtracted from the introduced gas amount into the line part

and the sample cell.

Prior to the measurement, all materials were degassed at 200 ºC for 12 h under dynamic vacuum condition in a stainless tube, and the materials were put into the sample cell in a glove box filled by highly purified Ar gas (>99.9999%). When the sample cell was connected to the cold head, Apiezon N high vacuum grease (Apiezon products M&L Materials LTD) was used to make close contact between the sample cell and the cold head to obtain good thermal conductivity and less temperature gradient. Ar gas in the sample cell was evacuated to 1×10^{-4} MPa by rotary pump at room temperature, and the air in the vacuum insulation container (cryostat) was evacuated to 1×10^{-2} Pa by turbo molecular pump with diaphragm pump. Then, the sample cell was cooled by the He cryocooler and the temperature was adjusted to desired temperature by heater block with a temperature controller surrounding the sample cell.

The measurements of isotherms for H_2 were carried out by using the cell with and without adsorbents listed in Table. 3.2.1 at the boiling point of H_2 (20.4 K). The temperature dependence of H_2 adsorption using MSC-30, GNPs, and MOF-177 was investigated below the critical temperature of H_2 at 20.4 K (0.10 MPa), 23.3 K (0.22 MPa), 26.5 K (0.44 MPa), and 30.6 K (0.88 MPa), where inside of brackets showed the phase transition pressure at each temperature. In order to investigate the gas dependence of adsorption properties, the measurements using MSC-30 were carried out for H_2, D_2, Ne, and N_2 at each boiling point of 20.4, 23.6, 27.1, and 77.2 K, respectively. The temperature dependence on each gas was investigated at 23.6 K (0.10 MPa), 26.6 K (0.22 MPa), 29.9 K (0.44 MPa), and 33.9 K (0.88 MPa) for D_2, and at 27.1 K (0.10 MPa), 29.4 K, 32.5 K for Ne, and at 77.2 (0.10 MPa), 85.1 K (0.22 MPa) and 92.9 K (0.44 MPa) for N_2. These temperatures were determined by referencing the liquefaction pressure obtained from the results of isotherms and the database in NIST chemistry Web Book.[9]

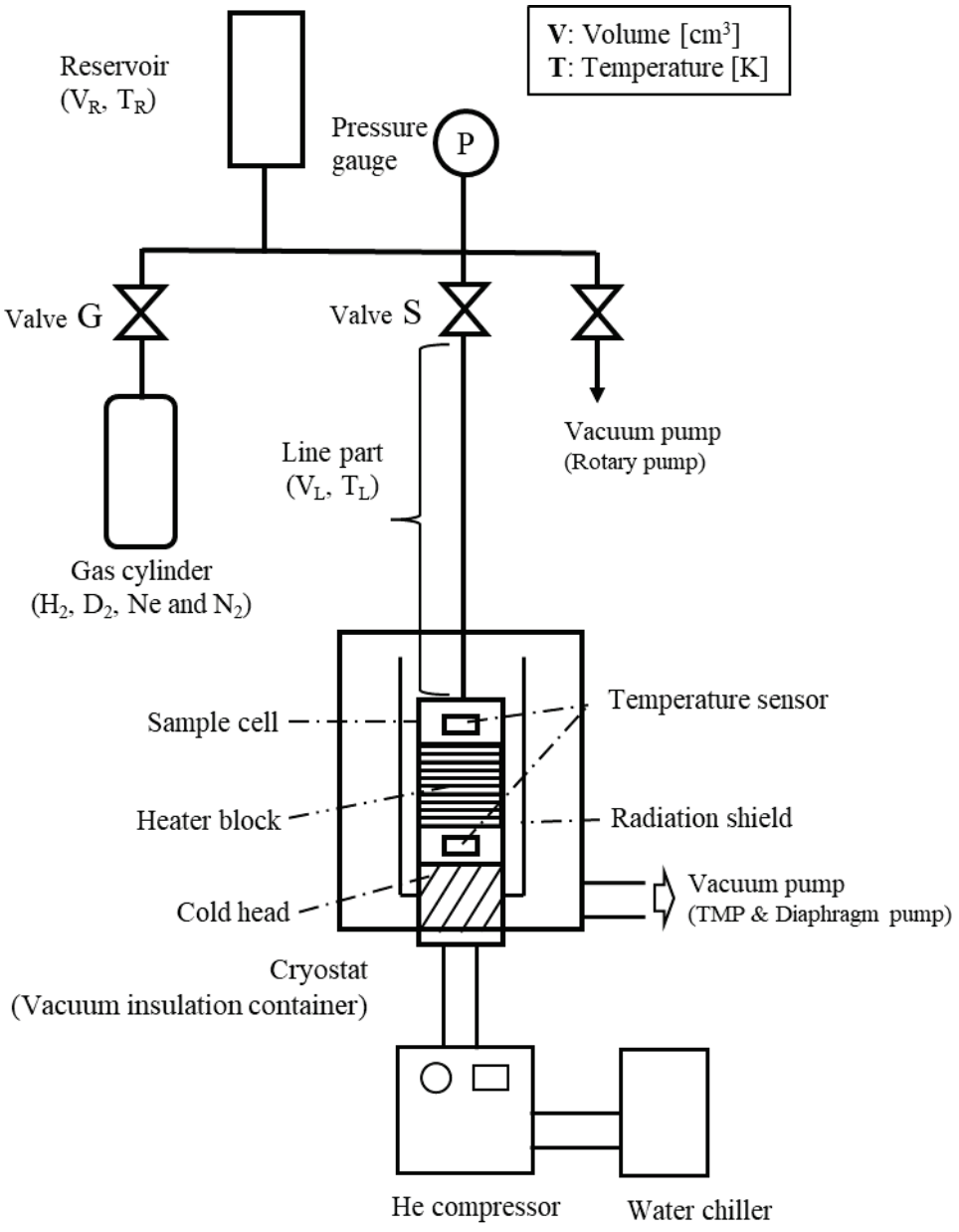

Fig. 3.3.4 Schematic diagram PCI and the cryostat systems.

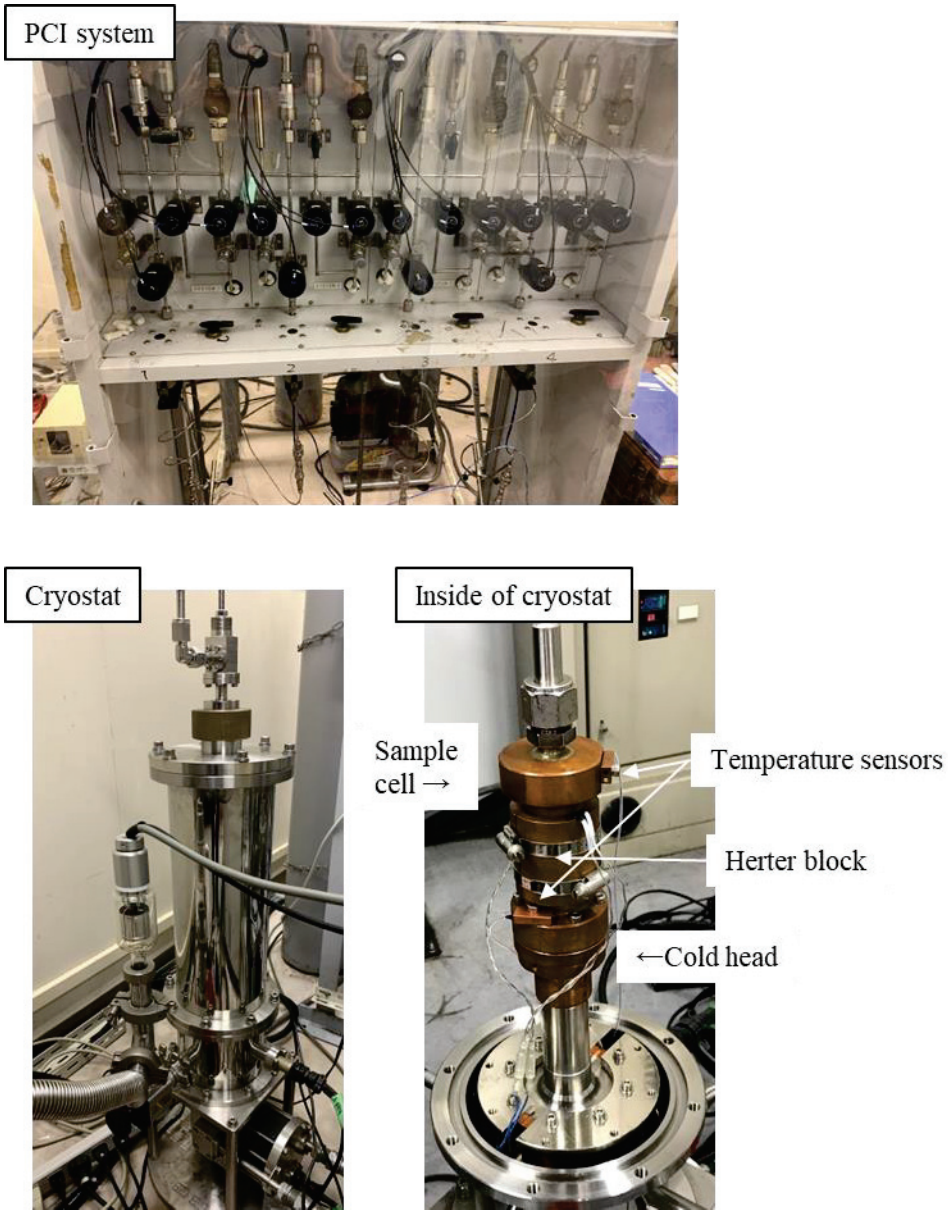

Fig. 3.3.5 Picture of the PCI system and the cryostat and inside of cryostat

3.3.5 Evaluation of density of adsorbate

The densities of adsorbed H_2 ($\rho_{ads.H_2}$; $\mathrm{mol/cm^3}$) for all the adsorbents were evaluated based on the results obtained from the experiment in the section 3.3.4. Figs. 3.3.6 show a typical result of the isotherms for an empty cell (Blank) and a cell with adsorbents, representing the i-H_2 amount into both cells as a function of H_2 pressure. In Fig. 3.3.6, the points of "α" and "β" were defined, corresponding to the "beginning" and "end" point of liquefaction, respectively. The density of adsorbed H_2 ($\rho_{ads.H_2}$; $\mathrm{mol/cm^3}$) was evaluated by following identities related to the points α and β. Initially, the read value of i-H_2 amount at the point α (n_α; mol) is given by

$$n_\alpha = n_{ads.H_2} + n_{\alpha.gas.H_2}, \tag{3.3.15}$$

where $n_{ads.H_2}$ is the amount of adsorbed H_2 as unknown value, and $n_{\alpha.gas.H_2}$ (mol) is the amount of gaseous H_2 as unknown value. At the point β, the read value of i-H_2 amount (n_β; mol) is given by

$$n_\beta = n_{ads.H_2} + n_{liq.H_2} + n_{\beta.gas.H_2}, \tag{3.3.16}$$

where $n_{ads.H_2}$ is assumed to be equal to that of point α, $n_{liq.H_2}$ (mol) is the amount of liquid H_2 as unknown value, and $n_{B.gas.H_2}$ (mol) is the amount of gaseous H_2 as unknown value.

The identity equations about the volume in the cell occupied with adsorbents at the point α and β are shown below. At the point of α, the total volume of the cell ($V_{cell} = 12.3\ \mathrm{cm^3}$) is represented as

$$V_{cell} = V_{ads.H_2} + V_{\alpha.gas.H_2} + V_{sk} = \frac{n_{ads.H_2}}{\rho_{ads.H_2}} + \frac{n_{\alpha.gas.H_2}}{\rho_{gas.H_2}} + \frac{m}{\rho_{sk}}, \tag{3.3.17}$$

where $V_{ads.H_2}$ and $V_{\alpha.gas.H_2}$ ($\mathrm{cm^3}$) are the volume of adsorbed H_2 and gaseous H_2, respectively, V_{sk} ($\mathrm{cm^3}$) is the skeletal volume of an adsorbent, $\rho_{gas.H_2}$ ($\mathrm{mol/cm^3}$) is the density of gaseous H_2 obtained from NIST chemistry Web Book[9] at each phase transition point, ρ_{sk} ($\mathrm{g/cm^3}$) is the skeletal density, and m (g) is the mass of an adsorbent put in the cell. By the same procedure, V_{cell} at the point β is given by

$$V_{cell} = V_{ads.H_2} + V_{liq.H_2} + V_{\beta.gas.H_2} + V_{sk} = \frac{n_{ads.H_2}}{\rho_{ads.H_2}} + \frac{n_{liq.H_2}}{\rho_{liq.H_2}} + \frac{n_{\beta.gas.H_2}}{\rho_{gas.H_2}} + \frac{m}{\rho_{sk}}, \tag{3.3.18}$$

where $\rho_{liq.H_2}$ is the density of liquid H_2 obtained from NIST chemistry Web Book[9] at each phase transition point. Here, the volume of the homogeneous temperature region was defined as the volume occupied by liquid H_2 in Blank ($V_h = n_{liq.H_2}^{empty}/\rho_{\mathrm{liq.H_2}}$) at the point β (see image in Fig. 3.3.6 (a)), where $n_{liq.H_2}^{empty}$ is the amount of liquid H_2 in Blank. Assuming that V_h of Blank is equivalent to that with adsorbents, V_h with adsorbents at the point β can be given by

$$V_h = \mathrm{V_{cell}} - V_{\beta.gas.H_2} = \mathrm{V_{cell}} - \frac{m_{\beta.gas.H_2}}{\rho_{gas.H_2}} \tag{3.3.19}$$

Accordingly, the equation 3.3.18 can be changed to equation 3.3.20

$$V_h = V_{ads.H_2} + V_{liq.H_2} + V_{sk} = \frac{n_{ads.H_2}}{\rho_{ads.H_2}} + \frac{n_{liq.H_2}}{\rho_{liq.H_2}} + \frac{m}{\rho_{sk}} \tag{3.3.20}$$

V_h ($= n_{liq.H_2}^{empty}/\rho_{\mathrm{liq.H_2}}$) can be determined by evaluating $n_{liq.H_2}^{empty}$ to solve the two identity equations 3.3.16 (without $n_{ads.H_2}$) and 3.3.18 (without $V_{ads.H_2}$, V_{sk}) based on the result of Blank as shown in Fig. 3.3.6 (a). Finally, five of unknown values, ($n_{ads.H_2}$, $\rho_{ads.H_2}$, $n_{\alpha.gas.H_2}$, $n_{\beta.gas.H_2}$ $n_{liq.H_2}$), can be evaluated by five identities of equation 3.3.15, 3.3.16, 3.3.17, 3.3.19, 3.3.20. By using the above processes, the value of $\rho_{ads.H_2}$ was evaluated for each adsorbent. For other gas such as D_2, Ne, and N_2, this method is available to evaluate the density of adsorbates. In this evaluation, the errors were evaluated to consider that the read value of n_α, n_β have errors of 0.001 and 0.003 mol, and ρ_{sk} has error of 0.5 g/cm^3.

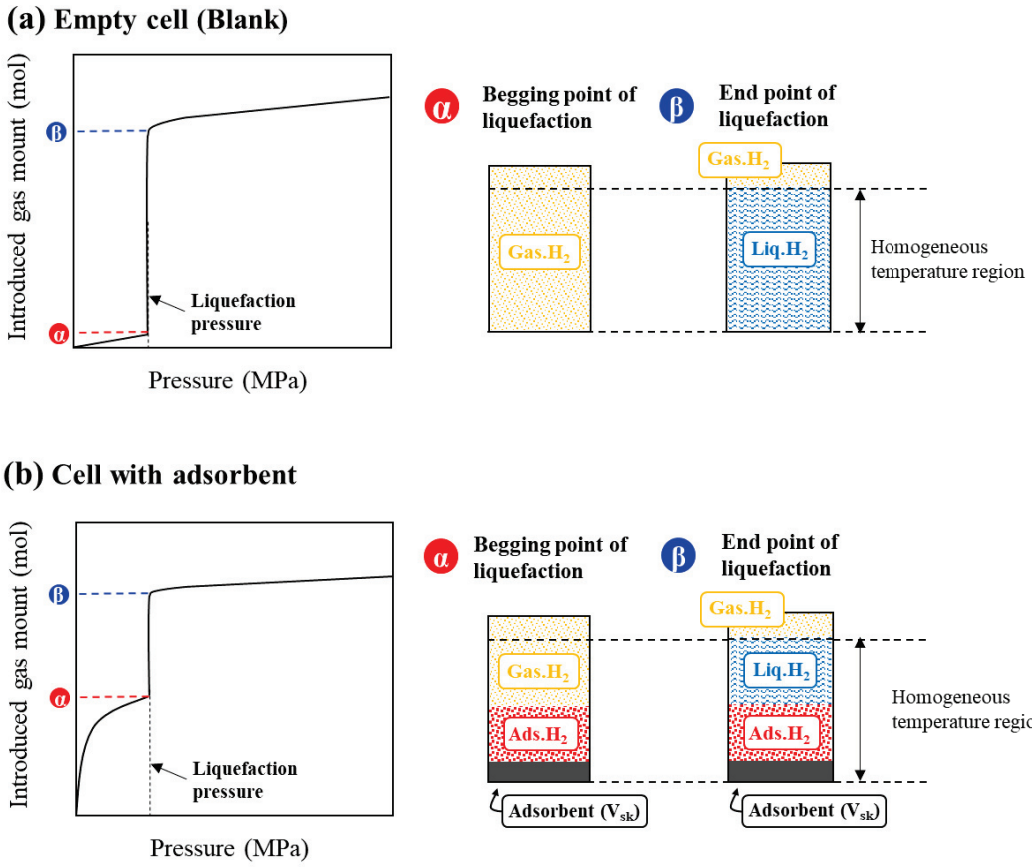

Fig. 3.3.6 Typical result of isothermal properties of H_2 introduction (left side) and image of inside of the cell at the bigging and end point of liquefaction for (a) an empty cell and (b) a cell with adsorbents

References

1. Mamedov, B. A. & Somuncu, E. Analytical treatment of second virial coefficient over Lennard-Jones potential and its application to molecular systems. *J Mol Struct* **1068**, 164–169 (2014).
2. Butt, H.-J. & Kappl, M. *Surface and Interfacial Forces*. (WILET-VCH, 2010).
3. Langmuir, I. The Adsorption of Gases on Plane Surfaces of Glass, Mica and Platinum. *J Am Chem Soc* **40**, 1361–1403 (1918).
4. Brunauer, S., Emmett, P. H. & Teller, E. Adsorption of Gases in Multimolecular Layers. *J. Am.Chem.Soc.* **60**, 309–319 (1938).
5. Livingston, H. K. The cross-sectional areas of molecules adsorbed on solid surfaces. *J Colloid Sci* **4**, 447–458 (1949).
6. Thommes, M. *et al.* Physisorption of gases, with special reference to the evaluation of surface area and pore size distribution (IUPAC Technical Report). *Pure and Applied Chemistry* **87**, 1051–1069 (2015).
7. Parilla, P. A., Gross, K., Hurst, K. & Gennett, T. Recommended volumetric capacity definitions and protocols for accurate, standardized and unambiguous metrics for hydrogen storage materials. *Appl Phys A Mater Sci Process* **122**, 1–18 (2016).
8. Rouquerol, J., Llewellyn, P. & Rouquerol, F. Is the BET equation applicable to microporous adsorbents. *Stud Surf Sci Catal* **160**, 49–56 (2007).
9. Eric W. Lemmon, Ian H. Bell, Marcia L. Huber, and Mark O. McLinden, "Thermophysical Properties of Fluid Systems" in NIST Chemistry WebBook, NIST Standard Reference Database Number 69, Eds. P.J. Linstrom and W.G. Mallard, National Institute of Standards and Technology, Gaithersburg MD, 20899, https://webbook.nist.gov/chemistry/, (retrieved September 19, 2022).

4. Results and discussion

4.1 Textural properties of adsorbent

Textural properties of materials are investigated by the N_2 adsorption/desorption isotherms at 77 K as shown Figs. 4.1.1 (a) for carbon materials, (b) for MOFs, (c) for silica gel. The types of N_2 isotherms are classified by International Union of Pure and Applied Chemistry (IUPAC) categorization (see the Fig. 3.1.7), and summarized in Table. 4.1.1. The N_2 adsorption isotherms of MOF-177, HKUST-1, ZIF-8 are classified as Type I(a) given by the typical microporous adsorbents. Type I(b) isotherms are observed on MSC-30 and Fi-Mil-100, given by the microporous adsorbents with wider micropores or narrow mesopores. The isotherms of GNPs and Aerogel can be classified as Type II given by the typical nonporous or microporous adsorbents. The isotherm of MIL-53 includes Type I and II isotherm. The isotherms of Wakogel can be classified as Type IV, illustrating hierarchical structure including mesopore and micropore in the adsorbent, and the hysteresis loop is due to the effect of the capillary condensation as explained the experimental section. The gravimetric surface area is evaluated by BET method, and all results are in good agreement with the reported values.[1–10] MOF-177 shows the highest surface area of 3950 m^2/g. The volumetric surface area is evaluated to multiply the gravimetric surface area by the skeletal density, and then MSC-30 shows the highest value of 7975 m^2/cm^3. The total pore volume and the average of pore size are also evaluated and summarized in Table. 4.1.1. In addition, the referred pore size analyzed by the nonlocalized density functional theory (NLDFT) method, which provides more detailed pore size, are added in Table. 4.1.1 for microporous materials.

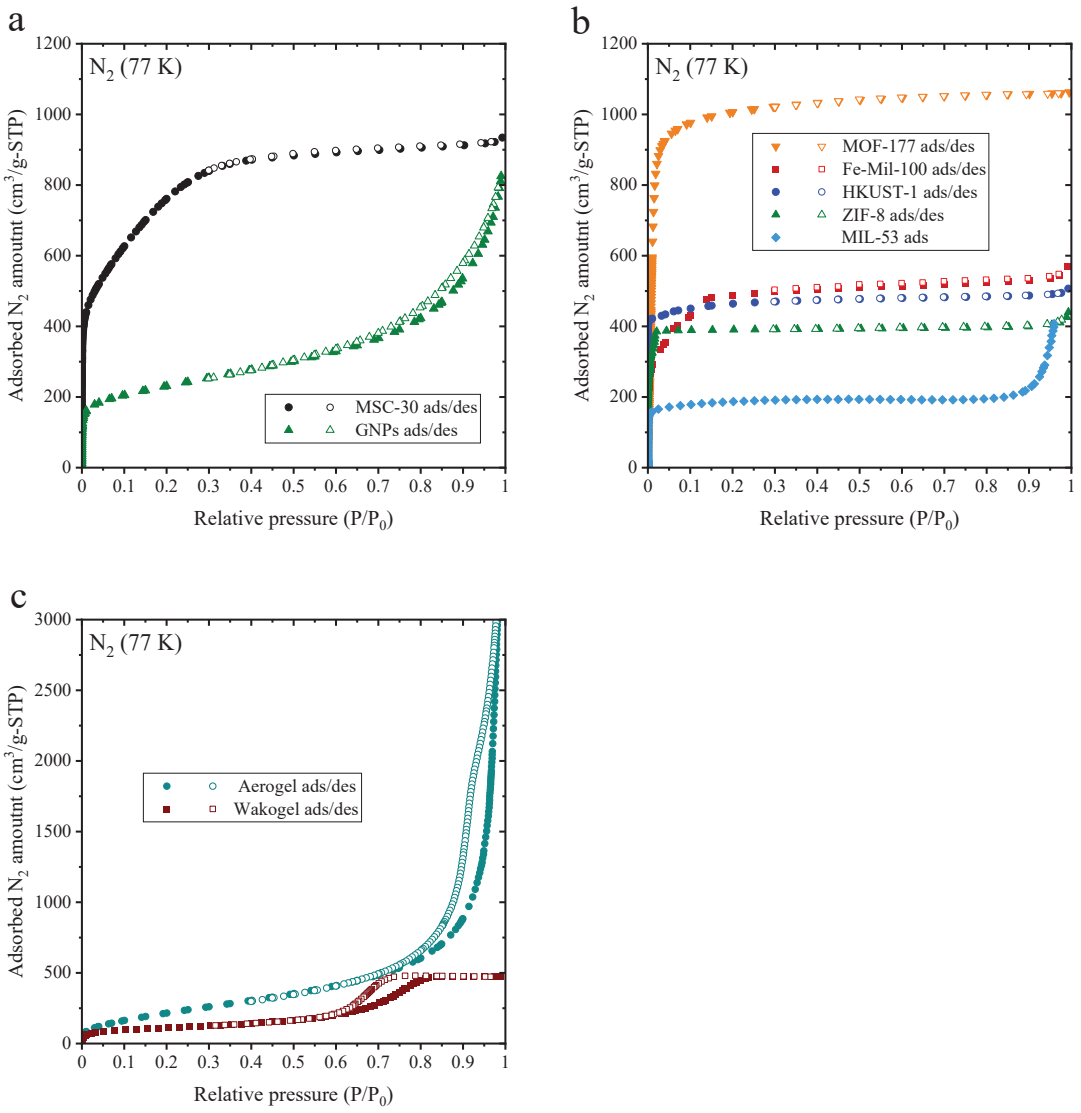

Figs. 4.1.1 N_2 isotherms at 77 K (a) carbon materials of MSC-30 and GNPs, (b) MOFs of MOF-177, Fe-Mil-100, HKUST-1, MIL-53 and ZIF-8 (c) silica gel of Aerogel and Wakogel.

Table. 4.1.1 Summary of textural properties of the materials.

Adsorbent		Adsorption type	Gravimetric surface area m^2/g	Volumetric surface area m^2/cm^3	Total pore volume cm^3/g	Average of pore size nm	Pore size* [ref] nm	Skeletal density g/cm^3
Crbon	MSC-30	Type I	3190	7975	1.6	2.2	1.1~3.0[11, 12]	2.5
	GNPs	Type II	810	1782	1.3	6.3	-	2.2
MOF	MOF-177	Type I	3950	6320	1.6	1.7	1.7~2.0[13]	1.6
	HKUST-1	Type I	1812	3443	0.8	1.7	1.0~1.2[13]	1.9
	Fe-Mil-100	Type I	1867	3734	0.9	1.9	1.2~2.1[14]	2.0
	MIL-53	Type I, II	967	1837	0.5	2.3	6~1.0[13, 15]	1.9
	ZIF-8	Type I	2061	3298	0.7	1.3	1.2~1.7[13]	1.6
Silica gel	Wakogel	Type IV	388	815	0.6	3.6	-	2.1
	Aerogel	Type II	1279	1919	5.6	26.0	-	1.5

*The pore size is based on the nonlocalized density functional theory (NLDFT)[11–15]

4.2 Material dependence of the super-dense hydrogen adsorption

4.2.1 Hydrogen adsorption isotherms at 20.4 K

Figs. 4.2.1 show the H_2 adsorption isotherms at the boiling pint of H_2 (20.4 K), which represents the gravimetric H_2 uptake (wt.%) as a function of the relative pressure p/p_0, where p_0 is the liquefied pressure (0.1 MPa) at the boiling point. The shapes of all H_2 isotherms are similar to the N_2 adsorption isotherms of Figs. 4.1.1, and can be classified as the same type of N_2 isotherms according to the IUPAC classification. This indicates that there are no significant differences in the physical adsorption phenomena between N_2 and H_2. The gravimetric H_2 uptakes at 0.1MPa for all materials are summarized in Table. 4.2.1. For all adsorbents, the H_2 uptakes at 20.4 K are higher than that at 77 K even under the condition of high pressure above 1 MPa. MOF-177 shows the highest gravimetric H_2 uptake of 13.0 wt.%, which is much higher than 1.36 wt.% obtained at 0.1 MPa, and 7.5 wt.% obtained at 7 MPa examined at 77 K by Dipendu et al..[3] Fig. 4.2.2 shows the liner relationship between the H_2 uptake and the specific surface area of adsorbents, indicating that adsorbents with higher surface area give the higher H_2 uptake, which is in good agreement with the trend in the previous research.[16–18] According to the Chahine's rule,[19,20] the gravimetric H_2 uptakes approximately correspond to 1 wt.% per 500 m^2/g of the specific surface area under the condition at 77 K. In the result of Fig. 4.2.2 under the condition at 20.4 K, the H_2 uptakes approximately correspond to 1wt.% per 300 m^2/g and 100 m^2/g on Type I and Type II-IV materials, respectively. The relatively high H_2 uptake per specific surface on Type II-IV adsorbents is due to the multilayer H_2 adsorption.

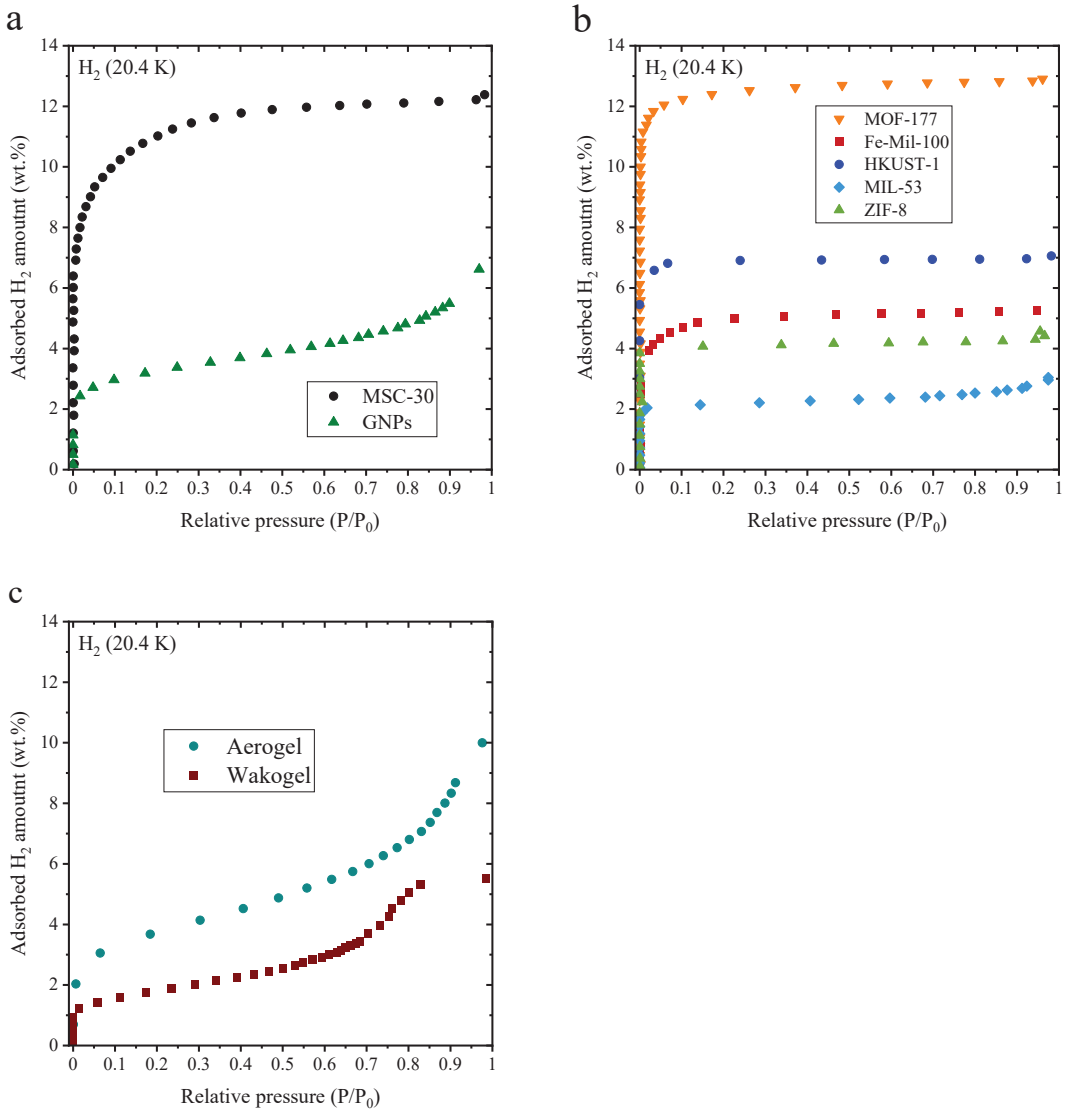

Figs. 4.2.1 H_2 adsorption isotherms on (a) carbon materials of MSC-30 and GNPs, (b) MOFs of MOF-177, Fe-Mil-100, HKUST-1, MIL-53 and ZIF-8 (c) silica gel of Aerogel, Wakogel at 20.4 K.

Table. 4.2.1 Gravimetric H_2 uptake and density of adsorbed H_2 on all adsorbents.[21,22]

Adsorbent		Adsorption type	Gravimetric surface area m^2/g	Gravimetric H_2 uptake @ 20.4 K wt.% (0.1 MPa)	Gravimetric H_2 uptake @ 77 K[ref] wt.% (Pressure)
Carbon	MSC-30	Type I	3190	12.2	5.0 (30 bar)[21]
	GNPs	Type II	810	6.6	-
MOF	MOF-177	Type I	3950	12.9	7.5 (70 bar)[22]
	HKUST-1	Type I	1812	7.1	3.6 (50 bar)[22]
	Fe-Mil-100	Type I	1867	5.3	3.3 (25 bar)[22]
	MIL-53	Type I, II	967	3.5	3.8 (16 bar)[22]
	ZIF-8	Type I	2061	4.4	1.5 (40 bar)[22]
Silica gel	Wakogel	Type IV	388	5.5	-
	Aerogel	Type II	1279	10.0	-

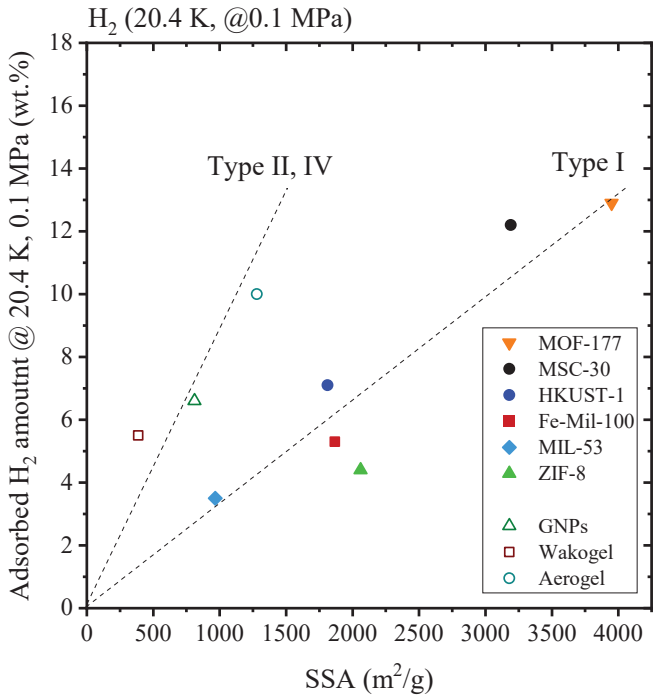

Fig. 4.2.2 The liner relationship between the adsorbed H_2 uptake (wt.%) and the surface area (m^2/g) at 20.4 K and 0.1 MPa for all materials. The solid symbols and open symbols correspond to the results on Type I and Type II, IV, respectively.

4.2.2 Density of adsorbed hydrogen at the boiling point

Figs. 4.2.3 show the isothermal curves, representing the introduced H_2 (i-H_2) amount into the empty sample cell for blank measurements and the cell with each adsorbent of (a) carbon materials, (b) MOFs, and (c) other materials. The densities of adsorbed H_2 for all adsorbents are investigated by the method described in the experimental section 3.3.5. In Figs, 4.2.3, the blank result shows the characteristics of the pure H_2, which shows subtle increase in i-H_2 amount as the gaseous H_2 below 0.1 MPa, and then i-H_2 amount simply increases at 0.1 MPa as the phase transformation from gas to liquid. At the end point of liquefaction, which is defined as the point in Fig. 3.3.6, the volume occupied by liquid H_2 in the blank measurement is evaluated to be 9.3 cm^3 (see also experimental section 3.3.5), where the volume of liquid H_2 illustrated in blue color is defined as homogeneous temperature region as shown in Fig. 4.2.3 (d). Above 0.1 MPa, i-H_2 amount gradually increase with increasing the pressure because the region of the gaseous H_2 illustrated in orange color in Fig. 4.2.3 (d) has slight temperature gradient. This phenomenon can be understood by the expansion of liquefied H_2 region, which is caused by satisfying the liquefaction conditions above H_2 boiling point (at 20.4 K and 0.1 MPa).

In the case of the isotherms with adsorbents, i-H_2 amount clearly increase by H_2 adsorption on adsorbents below 0.1 MPa as a main contribution. At 0.1 MPa, liquefaction of H_2 starts, then the free volume, which is the cell volume excluding the volume of adsorbents and adsorbed H_2, is filled with liquefied H_2. Fig. 4.2.3 (d) illustrates the image of occupation in the cell filled with liquid H_2, gaseous H_2, adsorbents and adsorbed H_2 at 0.1 MPa. Here, I'd like to focus on the result of MSC-30. Comparing the i-H_2 amount at the end point of liquefaction (inset of Fig. 4.2.3), the value of MSC-30 is almost equivalent to that of the blank result even though the H_2 molecules cannot occupy the volume with carbon atoms of MSC-30. In other words, the free volume (defined in Fig. 3.2.1) in the empty cell, in which the H_2 molecule can exist, should be larger than that with MSC-30 (see also Fig.

4.2.3 (d)). According to this result, it can be expected that the density of adsorbed H_2 on MSC-30 is much higher than that of liquid H_2. In this case, this anomalously high density of adsorbed H_2 at 20.4 K is suggested as the "super-dense H_2 adsorption".

In order to quantitatively discuss the superdense state of H_2, the densities of adsorbed H_2 ($\rho_{ads.H_2}$) on each adsorbent at 20.4 K and 0.1 MPa, and the results are summarized in Table 4.2.2. Interestingly, $\rho_{ads.H_2}$ on almost all of the adsorbents (excluding MIL-53) show higher density than the density of liquid H_2 ($\rho_{liq.H_2}$:35.2 mmol/cm^3) at 20.4 K as the super-dense adsorption. In particular, $\rho_{ads.H_2}$ on adsorbents with Type I adsorption isotherms (MSC-30, MOF-177, HKUST-1, Fe-Mil-100 and ZIF-8) shows relatively high value in the range of 43.0~47.4 mmol/cm^3, compared with that on adsorbents with Type II or IV adsorption isotherms (GNPs, Wakogel, Aerogel) which show $\rho_{ads.H_2}$ around 40 mmol/cm^3. Especially, the values of $\rho_{ads.H_2}$ for Type I adsorbents show higher density than the solid H_2 density ($\rho_{sol.H_2}$: 43 mmol/cm^3), which is known as a hexagonal close-packed (hcp) structures below 14 K.[23–25] These results suggest that the influence of super-dense effect depends on the adsorption type of adsorbents rather than the surface element of adsorbents. The adsorption types are determined by the pore structure (micropore, mesopore and macropore), and the significant difference between Type I and Type II-IV adsorption is the amount of the monolayer and multilayer adsorption, where Type I adsorption is mostly occupied by the monolayer adsorption. Therefore, it can be expected that the monolayer H_2 forms the super-dense H_2 state due to a direct interaction between H_2 molecules and the surface of adsorbents. This monolayer H_2 properties are discussed later in the section 4.4.

Next, it is discussed the reason why only MIL-53 shows the much lower $\rho_{ads.H_2}$ of 27.3 mmol/cm^3 compared with $\rho_{liq.H_2}$ (35.2 mmol/cm^3) and $\rho_{ads.H_2}$ on all adsorbents. MIL-53 has the smallest micropore size (6~10 Å) analyzed by nonlocalized density functional theory (NLDFT) method as shown in Table 4.2.1, which is relatively close to the intermolecular distance of H_2-H_2 in

bulk-solid (3.76 Å).[26] The values of $\rho_{ads.H_2}$ were evaluated by using the skeletal densities of adsorbents, which were experimentally measured by He gas. Since the size of He atom is smaller than that of H_2 molecule, He can fill the smaller pores compared with that of H_2. In other words, pores, that H_2 molecule cannot fill, are regarded as closed pores, and the skeletal density for H_2 must be smaller than that for He. Therefore, it is possible that $\rho_{ads.H_2}$ on MIL-53 is evaluated to be lower than actual value. If the pore size, that is bigger than He molecule and smaller than H_2 molecule, exists, the skeletal density measured by He and H_2 must be different.

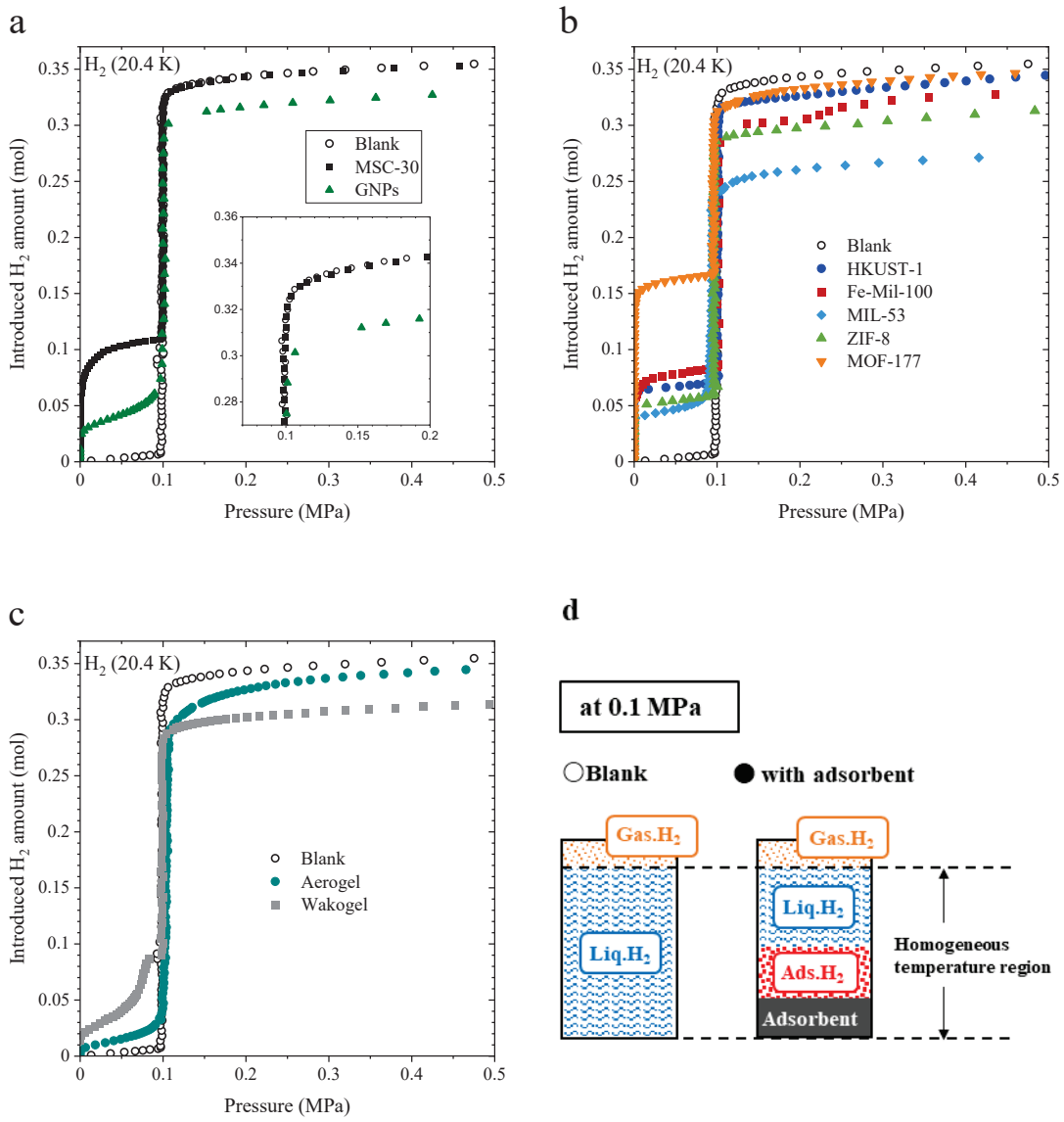

Figs. 4.2.3 Isothermal properties of H_2 introduction into the cell (12.3 cm^3) with and without adsorbents for (a) carbon materials of MSC-30 and GNPs, (b) MOFs of MOF-177, Fe-Mil-100, HKUST-1, MIL-53 and ZIF-8 (c) silica gel of Aerogel, Wakogel and at 20.4 K. (d) Image of inside of cryogenic cell with and without adsorbent at 0.1 MPa.

Table. 4.2.2 Density of adsorbed H_2 together with textural properties of adsorption type, gravimetric surface area, pore size.

Adsorbent		Adsorption type	Gravimetric surface area m^2/g	Pore size[ref] Å	Density of adsorbed H_2 $mmol/cm^3$
Crbon	MSC-30	Type I	3190	11~30[11, 12]	43.6
	GNPs	Type II	810	-	40.0
MOF	MOF-177	Type I	3950	17~20[13]	47.3
	HKUST-1	Type I	1812	10~12[13]	44.8
	Fe-Mil-100	Type I	1867	12~21[14]	47.4
	MIL-53	Type I, II	967	6~10[13, 15]	27.4
	ZIF-8	Type I	2061	12~17[13]	43.0
Silica gel	Wakogel	Type IV	388	-	39.0
	Aerogel	Type II	1279	-	38.4

4.3 Temperature dependence of the super-dense hydrogen adsorption

4.3.1 Hydrogen adsorption isotherms

Figs. 4.3.1 show the H_2 adsorption isotherms which represent the gravimetric H_2 uptake as a function of H_2 pressure at 20.4. 23.3, 26.5, 30.6 K on MSC-30, GNPs and MOF-177. The maximum H_2 uptakes on all adsorbents decreases with increasing pressure. This is a general trend of the typical physical adsorption. The heat of adsorption on MSC-30, GNPs and MOF-177 is estimated by applying the Clausius-Clapeyron equation to the H_2 adsorption isotherms in Figs. 4.3.1 at different temperature, and the results are shown in Fig. 4.3.2. The three adsorbents show the heat of adsorption between 1-3 kJ/mol in descending order of MOF-177, MSC-30 and GNPs. The heat of adsorption in the region of low H_2 uptake cannot be estimated because of the low pressure below the limit of pressure gauge. This low pressure region represents the monolayer adsorption, so it is inadequate for discussing the superdense H_2 adsorption.

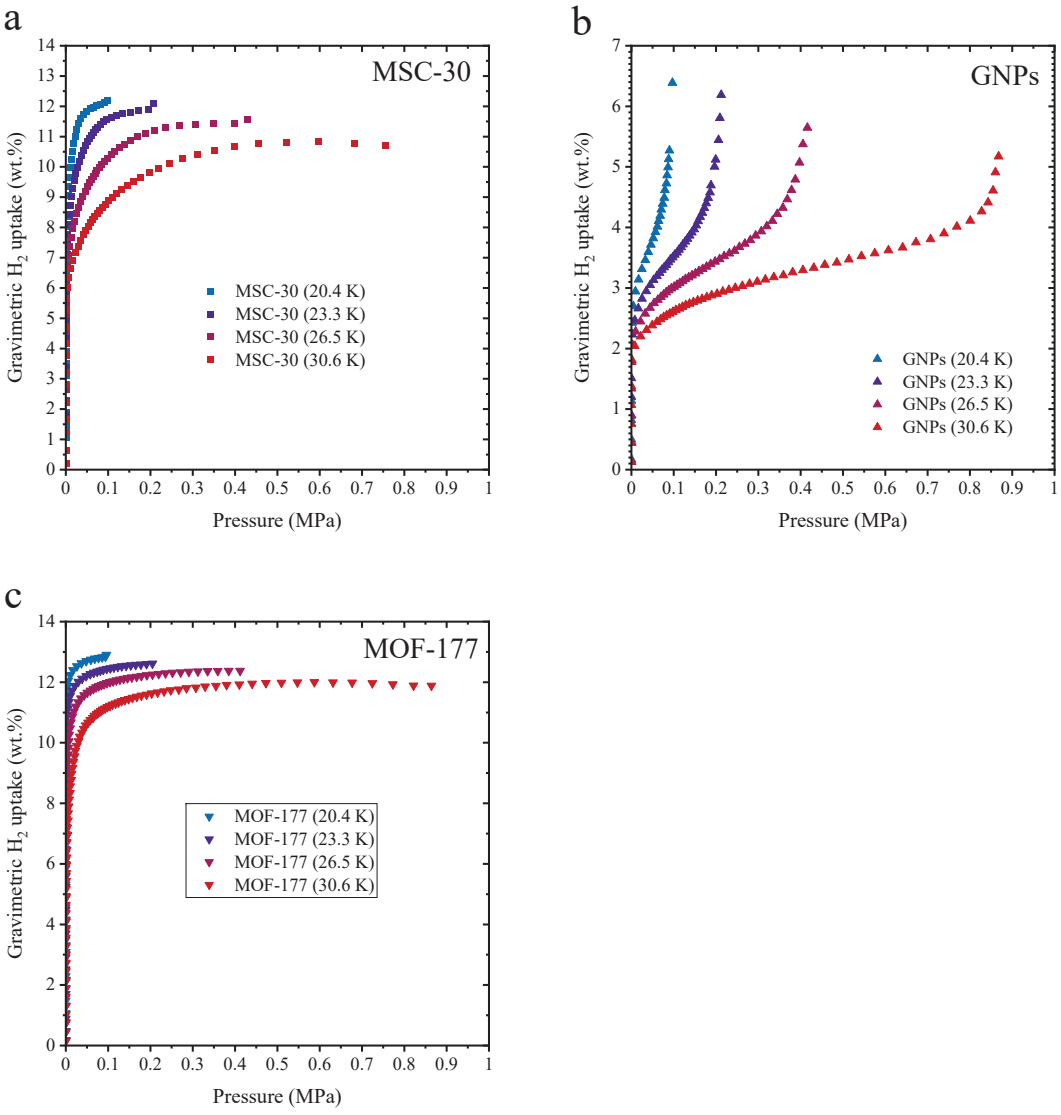

Fig. 4.3.1 Temperature change of H_2 adsorption isotherms at 20.4, 23.3, 26.5 and 30.6 K on (a) MSC-30, (b) GNPs, (c) MOF-177, respectively.

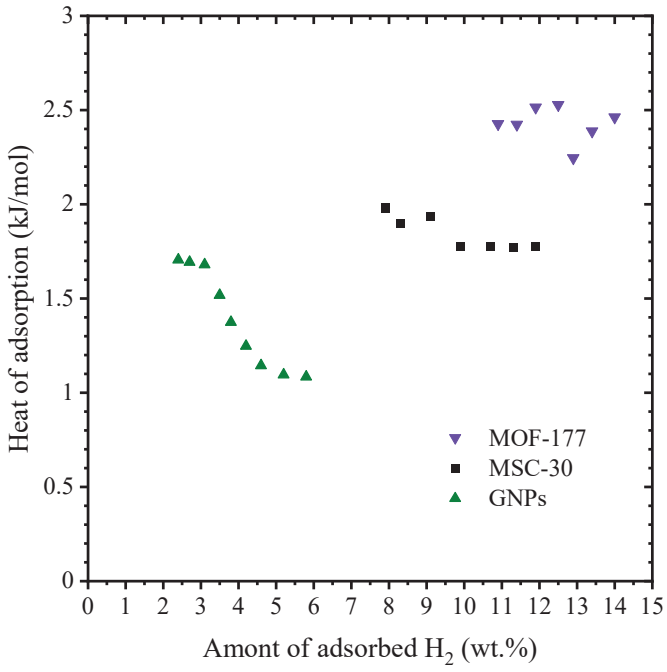

Fig. 4.3.2 Heat of adsorption on MSC-30, MOF-177 and GNPs.

4.3.2 Density of adsorbed hydrogen

Figs. 4.3.3 show the isothermal properties of the H_2 introduction into the cell with MSC-30, GNPs, and MOF-177 at 20.4, 23.3, 26.5 and 30.6 K in the same way as the experiment corresponding to Figs. 4.2.3. The isotherms of the blank cell show each liquefaction step, where H_2 liquefy at 0.10 MPa (20.4 K), 0.22 MPa (23.3 K), 0.43 MPa (26.5 K), and 0.88 MPa (30.6 K). The i-H_2 amount in the blank cell above each phase transition pressure tends to decrease with increasing temperature due to the physical properties of liquid H_2 density, which are 35.2 mmol/cm^3 (20.4 K, 0.10 MPa), 33.3 mmol/cm^3 (23.3 K, 0.22 MPa), 30.9 mmol/cm^3 (26.5 K, 0.42 MPa), and 26.2 mmol/cm^3 (30.6 K, 0.87 MPa). All isotherms for the cell with adsorbents show similar adsorption and liquefaction steps at each temperature. Comparing the i-H_2 amount of blank results with i-H_2 of adsorbents above each phase transition pressure, it is noteworthy that the i-H_2 amount with MOF-177 and MSC-30 gradually exceeds the value of blank with increasing temperature. These phenomena suggest that the temperature dependence of $\rho_{ads.H_2}$ is different from $\rho_{liq.H_2}$. In other words, the density of superdense H_2 is less affected by temperature than the density of liquid H_2.

The values of $\rho_{ads.H_2}$ at each temperature and on each adsorbent are evaluated in the same way as discussed in the section 4.2.2. The evaluated $\rho_{ads.H_2}$ is plotted as a function of temperature in Fig. 4.3.4 together with $\rho_{liq.H_2}$ at each phase transition point. It can be seen that $\rho_{ads.H_2}$ on any adsorbents shows the higher density than $\rho_{liq.H_2}$ at any temperatures, and MOF-177 shows the highest $\rho_{ads.H_2}$, followed in the order MSC-30 and GNPs. Temperature change of $\rho_{ads.H_2}$ on adsorbents doesn't significantly decrease with increasing temperature compared with $\rho_{liq.H_2}$. In particular, the values of $\rho_{ads.H_2}$ on MOF-177 and MSC-30 with the large amount of monolayer H_2 as the Type I adsorption show the temperature independent properties. According to these results, it can be seen that the monolayer H_2 strongly interacted with material surface leads to the temperature independence of super-dense H_2 state.

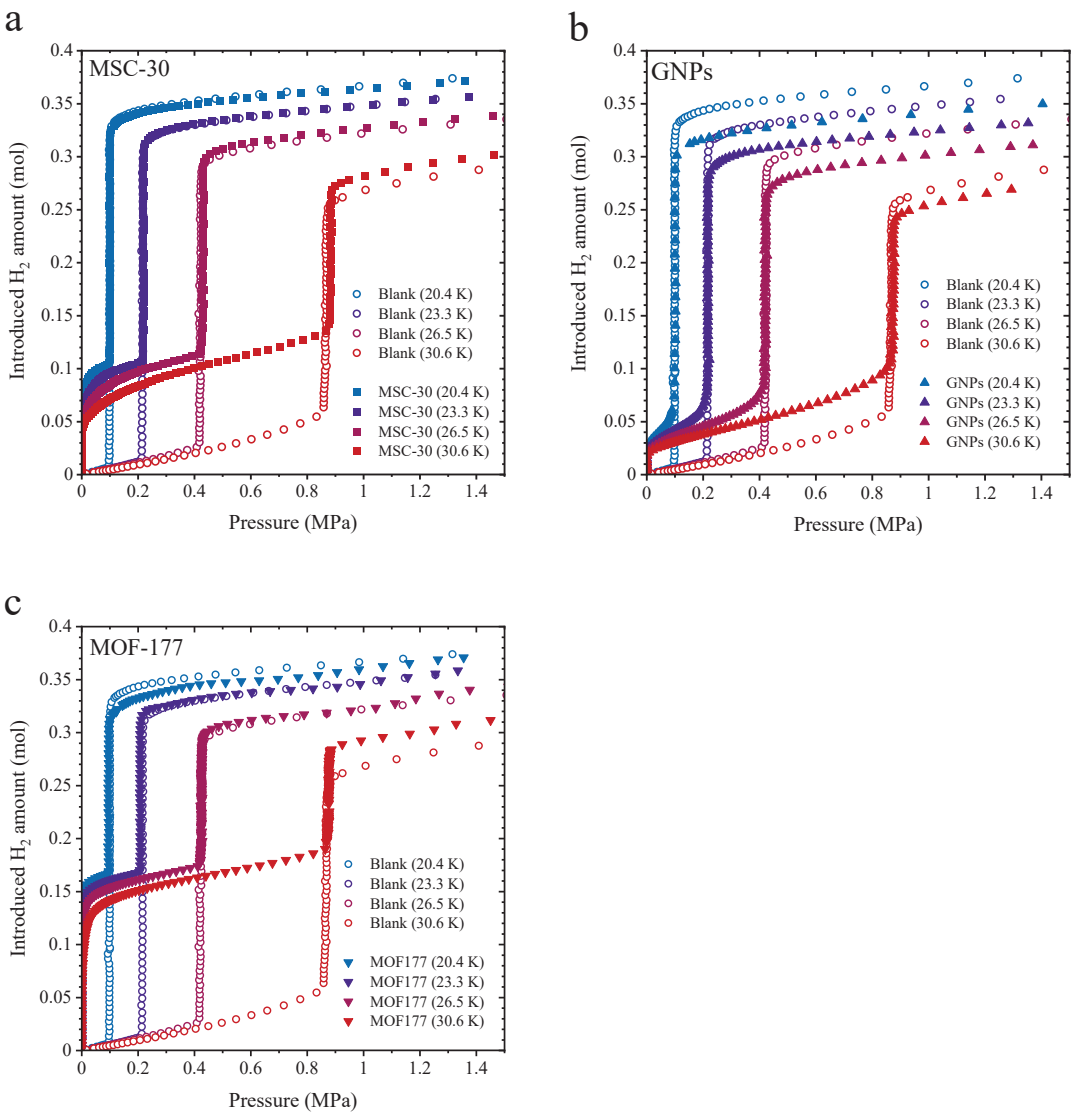

Figs. 4.3.3 Temperature dependence of isothermal properties for H_2 introduction into the empty cell (blank) and into the cell with (a) MSC-30, (b) GNPs and (c) MOF-177 at 20.4, 23.3, 26.5, 30.6 K, respectively.

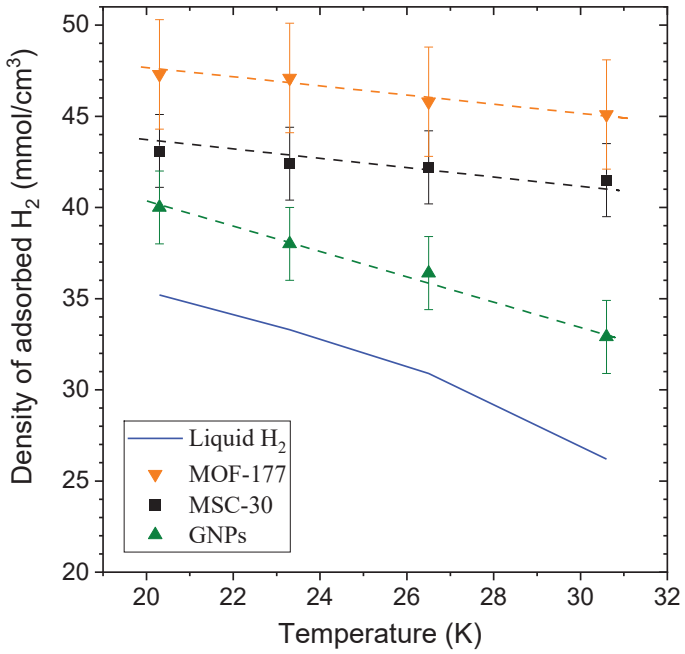

Fig. 4.3.4 Temperature dependence of the density of adsorbed H_2 compared to that of liquid H_2. The density of adsorbed H_2; $\rho_{ads.H_2}$ at 20.4, 23.3, 26.5, 30.6 K on MOF-177. MSC-30 and GNPs.

4.3.3 Isobars of volumetric hydrogen capacity

Fig. 4.3.5 shows the isobaric curve at 0.9 MPa as a function of temperature in the range of 10-80 K, which represents the i-H_2 amount (left Y axis) corresponding to the volumetric H_2 capacity in the cell (right Y axis). The volumetric H_2 capacity of the cell (ρ_{vol}^{cell}) can be evaluated by

$$\rho_{vol}^{cell} = \frac{n_{int}}{V_{cell}}, \tag{4.3.1}$$

where n_{int}[mmol] is the i-H_2 amount; V_{cell} [cm^3] is the volume of cryogenic cell (12.3 cm^3). By comparing ρ_{vol}^{cell} in the blank cell and ρ_{vol}^{cell} in the cell with MSC-30 and MOF-177, the isobaric properties of the volumetric H_2 capacity in the liquid H_2 tank with and without adsorbents are discussed. The sample cells are filled with 2.30 g of MSC-30 and 2.27 g of MOF-177, which correspond to 9.0 cm^3 of bulk-volume for both materials. The isobaric curve of blank shows the characteristics of the pure H_2. In the temperature range of 30-80 K with the gaseous phase of H_2, the results of MSC-30 and MOF-177 show much higher volumetric H_2 capacity compared with that of blank, which is naturally due to the contribution of H_2 adsorption on adsorbents. At 30 K and 0.9 MPa, H_2 starts to liquefy and the i-H_2 amount (volumetric H_2 capacity) increase up to 23.1, 22.3, 20.5 mmol/cm^3 for the cell of MSC-30, MOF-177 and blank, respectively. It is notable that the cells with both adsorbents have higher volumetric H_2 capacity than that of blank even in the liquid phase of H_2, especially, the capacity of MSC-30 is 13% higher than that of blank at 30 K and 0.9 MPa. With decreasing temperature from 30 K, the volumetric H_2 capacity increase due to the increase in the density of liquid H_2. The capacity of MSC-30 and MOF-177 gradually increase with decreasing temperature compared with that of blank. This is because of the temperature independence of adsorbed H_2 density as the super-dense state, which is in good agreement with the temperature change of the isotherms and $\rho_{ads.H_2}$ in Figs. 4.3.3 and Fig. 4.3.4, respectively. The volumetric H_2 capacity in the blank cell is equivalent to that of MOF-177 at 27.5 K and MSC-30 at 23.0 K. Here, behaviors of these isobar are considered in the viewpoint of H_2 losses by temperature increase (Boil-

off). Fig. 4.3.6 shows the H_2 losses with increasing temperature from 23 K to 30 K for the results of blank and MSC-30 based on the values in Fig. 4.3.5. It is clearly found that the amount of H_2 losses in the blank cell is larger than that of MSC-30 at higher temperature, which is due to the contribution of the temperature independent properties of super-dense H_2. At 30 K, the H_2 losses in the blank cell and with MSC-30 are 6.3 and 4.3 mmol/cm^3, respectively, which correspond to 32% of the suppression of H_2 losses by temperature increase from 23 to 30 K at 0.9 MPa by using MSC-30 adsorbent. Thus, this result suggests that H_2 storage of cryo-adsorption using porous materials provides not only the volumetric H_2 capacity equivalent to that of liquid H_2 but also the availability of the suppression of H_2 boil-off in the liquid H_2 storage tanks.

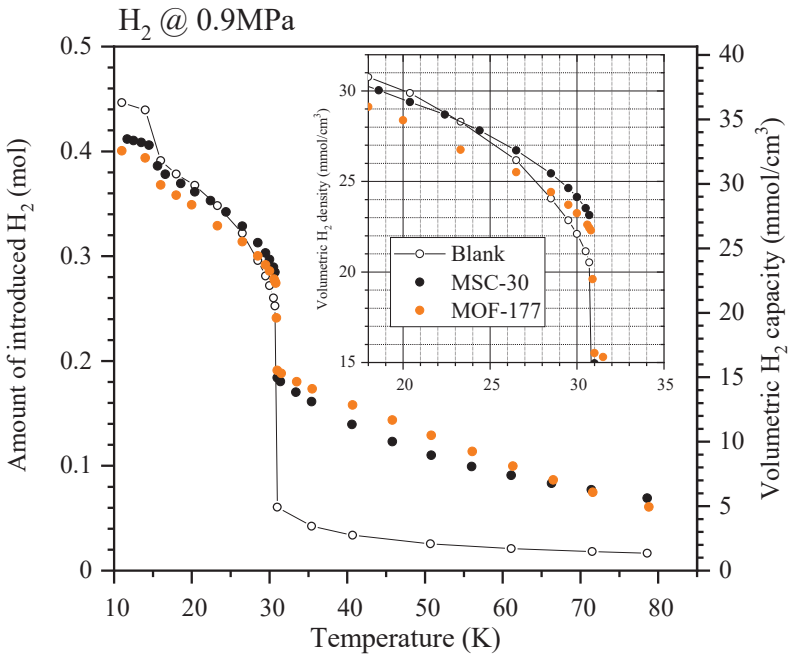

Fig. 4.3.5 Isobar of the introduced H_2 amount (left axis) corresponding to the volumetric H_2 density (right axis) in the blank cell and the cell with MSC-30 and MOF-177 at 0.9 MPa as a function of temperature in the range of 10-80 K.

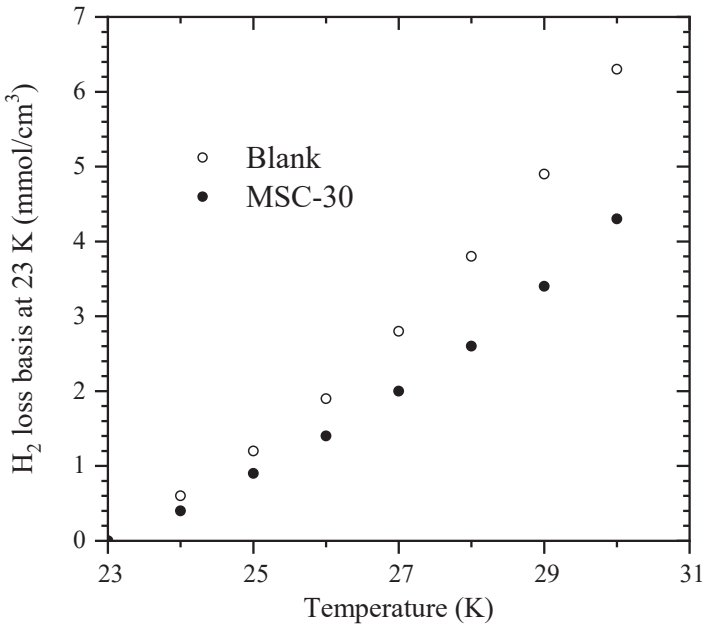

Fig. 4.3.6 H_2 losses with increasing temperature from 23 K at 0.9 MPa in the cell with and without MSC-30.

4.4 Adsorbed layer dependence of the super-dense hydrogen adsorption

Here, microscopic structures of adsorbed H_2 molecules are pictured by taking account of adsorption Types I and II to discuss the superdense H_2 state and the temperature dependence. Type I adsorption isotherms for MSC-30 and MOF-177 are given by micropores filling of H_2 at low pressure due to the strong interaction with the material surface in narrow micropores. It can be considered that the adsorption with strong interaction makes the adsorption state to be the superdense H_2 state. In the case of Type II adsorption isotherms for GNPs, it is understood that the end point of steep H_2 uptake at low pressure corresponds to the completion of monolayer coverage and after that, H_2 uptake gradually increases by multilayer adsorption. In the BET theory, it is assumed that the multilayer adsorption region is equivalent to liquid phase and the monolayer adsorption region just on the surface is more stable than the liquid phase.[27] H.K. Livingston[28] and Xicohténcatl et al.[26] reported the anomalously low cross-sectional areas of H_2 at 20 K on the Ni foil and a mesoporous silica compared with bulk-liquid and bulk-solid H_2 density, indicating the super-dense H_2 state just on the material surface similar to our result.

In this work, the region of monolayer adsorption was focused on and the density of monolayer H_2 ($\rho_{ads.H_2}^{mono}$) just on the material surface was evaluated based on the BET theory. It is possible to determine the monolayer H_2 uptake ($n_{wt.\%}^{mono}$) by applying BET equation to the adsorption isotherms in Figs. 4.3.1, and the ratio of monolayer H_2 uptake to the total uptake (R_{mono}) is given by

$$R_{mono} = {n_{wt.\%}^{mono}}\Big/{n_{wt.\%}^{max}} \tag{4.4.1}$$

where $n_{wt.\%}^{max}$ is the maximum H_2 uptake obtained from Figs. 4.3.1. The values of R_{mono} are evaluated to be 74%, 42% and 90% for MSC-30, GNPs and MOF-177, respectively, at 20.4 K. R_{mono} at other temperature on each adsorbent show similar values and they are summarized in Table. 4.4.1. Thus, the density of monolayer H_2 ($\rho_{ads.H_2}^{mono}$) is given by

$$\rho_{ads.H_2}^{mono} = \frac{n_{ads.H_2}^{mono}}{V_{ads.H_2}^{mono}} = \frac{n_{ads.H_2}^{mono}}{V_{ads.H_2} - V_{ads.H_2}^{multi}} = \frac{R_{mono} n_{ads.H_2}}{n_{ads.H_2}/\rho_{ads.H_2} - R_{multi} n_{ads.H_2}/\rho_{ads.H_2}^{multi}}, \quad (4.4.2)$$

where $n_{ads.H_2}^{mono}$ (mol) is the amount of monolayer H_2, $V_{ads.H_2}^{mono}$ (cm^3) is the volume of monolayer H_2 $V_{ads.H_2}$ (cm^3) is the volume of total adsorbed H_2, $V_{ads.H_2}^{multi}$ (cm^3) is the volume of multilayer H_2, $n_{ads.H_2}$ (mol) is the total amount of adsorbed H_2; R_{multi} is the ratio of multilayer H_2 given by

$$R_{multi} = 1 - R_{mono} \quad (4.4.3)$$

Here, the density of multilayer H_2 ($\rho_{ads.H_2}^{multi}$) can be considered as liquid phase ($\rho_{liq.H_2}$) at each phase transition point, which is following the assumption of the BET theory. Finally, $\rho_{ads.H_2}^{mono}$ can be evaluated by

$$\rho_{ads.H_2}^{mono} = \frac{R_{mono} n_{ads.H_2}}{n_{ads.H_2}/\rho_{ads.H_2} - R_{multi} n_{ads.H_2}/\rho_{liq.H2}} \quad (4.4.4)$$

The evaluated $\rho_{ads.H_2}^{mono}$ on MSC-30, GNPs and MOF-177 are plotted in Fig. 4.4.1 as a function of temperature below critical point of H_2. As a result, $\rho_{ads.H_2}^{mono}$ on all adsorbents show the constant value of 50 mmol/cm^3 without temperature dependence below the critical point of H_2. Therefore, it can be concluded that the super-dense H_2 state is strongly related to the monolayer adsorption with direct interaction from material surface, irrespective of the adsorption types and temperature below critical point.

Focusing on the introduced H_2 (i-H_2) amount into the sample cell at 20.4 K above 0.1 MPa shown in Fig. 4.2.3, MSC-30 shows the highest i-H_2 amount, even though MOF-177 has the higher gravimetric H_2 uptake and larger amount of adsorbed H_2. In order to clarify this mystery, we evaluated the volumetric H_2 uptake (n_{mol/cm^3}). Since $\rho_{ads.H_2}^{multi}$ is regarded as $\rho_{liq.H_2}$ at each condition as discussed above, n_{mol/cm^3} is defined by

$$n_{mmol/cm^3} = \frac{n_{ads.H_2}^{mono}}{V_{ads.H_2}^{mono} + V_{sk}}, \quad (4.4.5)$$

where V_{sk} (cm^3) is the skeletal volume of adsorbents given by m/ρ_{sk}, m (g) is the weight of

materials; ρ_{sk} (g/cm^3) is the skeletal density of materials. According to the above discussion, n_{mol/cm^3} can be evaluated by

$$n_{mmol/cm^3} = \frac{R_{mono} n_{ads.H_2}}{R_{mono} n_{ads.H_2} \Big/ \rho_{ads.H_2}^{mono} + m \Big/ \rho_{sk}} \tag{4.4.6}$$

Accordingly, n_{mol/cm^3} for each adsorbent and temperature are evaluated and plotted in Fig. 4.4.2 as a function of temperature below the critical point of H_2. n_{mol/cm^3} shows constant values of 34 mmol/cm^3, 17 mmol/cm^3, and 33 mmol/cm^3 for MSC-30, GNPs, and MOF-177, respectively, without temperature dependence (see also the Table 4.4.1). MSC-30 shows the highest value of n_{mol/cm^3}, and it is comparable to $\rho_{liq.H_2}$ at 22 K and 30% higher than $\rho_{liq.H_2}$ at 30.6 K, that are consistent with the result of isobar of Fig. 4.3.5 representing the volumetric H_2 capacity in the cell discussed in section of 4.3.3.

When the density of monolayer H_2 shows the constant without temperature and material dependences, the cross-sectional area (σ; $\mathrm{m^2/molecule}$), which is a value of occupied area by one molecule of adsorbate, of H_2 must be a constant. By using the parameters of the cross-sectional area (σ), gravimetric surface area (S_{gravi}; $\mathrm{m^2/g}$), and mass of adsorbate (m; g), equations 4.4.5 and 4.4.6 are changed as

$$n_{ads.H_2}^{mono} = \frac{m \cdot S_{gravi}}{\mathrm{N_A}\sigma} \tag{4.4.7}$$

$$V_{ads.H_2}^{mono} = \frac{m \cdot S_{gravi} \Big/ \mathrm{N_A}\sigma}{\rho_{\mathrm{ads.H_2}}^{\mathrm{mono}}}, \tag{4.4.8}$$

where $\mathrm{N_A}$ is the Avogadro number (6.022×10^{23} mol^{-1}). When equations 4.4.7 and 4.4.8 are introduced into equation 4.4.5, $\rho_{H_2}^{vol}$ is given by

$$n_{mmol/cm^3} = \frac{1}{1 \Big/ \rho_{\mathrm{ads.H_2}}^{\mathrm{mono}} + \mathrm{N_A}\sigma \Big/ (m \cdot S_{gravi})}, \tag{4.4.9}$$

Here, the value of ($m \cdot S_{gravi}$) corresponds to the volumetric surface area (m^2/cm^3) of adsorbents.

Since the values of $\rho_{ads.H_2}^{mono}$ and σ are constant regardless of temperature and adsorbents based on the above discussion, equation 4.4.9 suggests that the volumetric surface area ($m \cdot S_{gravi}$) is a unique factor to determine the volumetric H_2 uptake of n_{mol/cm^3} under the super-dense H_2 phenomena. As a result, the highest value of n_{mol/cm^3} corresponding to the i-H_2 amount in Fig. 4.2.3 are shown on MSC-30 with the highest volumetric surface area ($m \cdot S_{gravi} = 7975\ m^2/cm^3$).

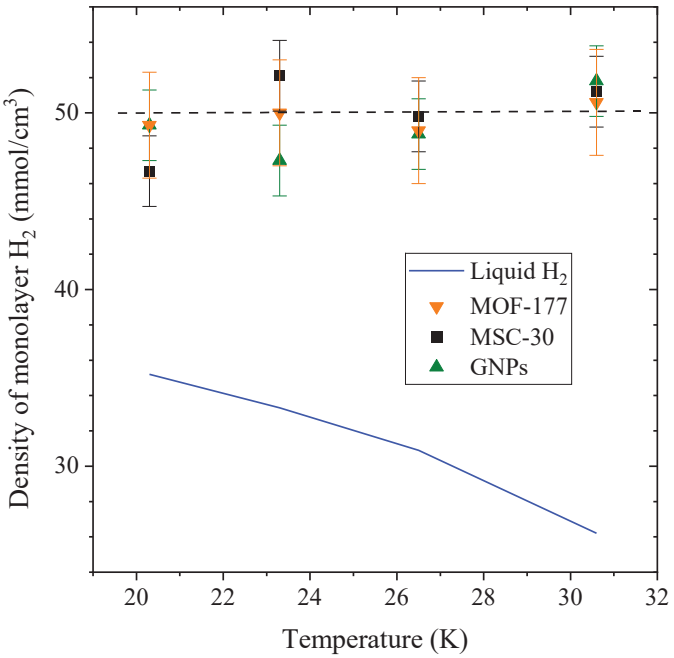

Fig. 4.4.1 Temperature dependence of the density monolayer H_2 ($\rho_{ads.H_2}^{mono}$)c on MSC-30, GNPs and MOF-177 at 20.4, 23.3, 26.5, 30.6 K, compared to the density of liquid H_2.

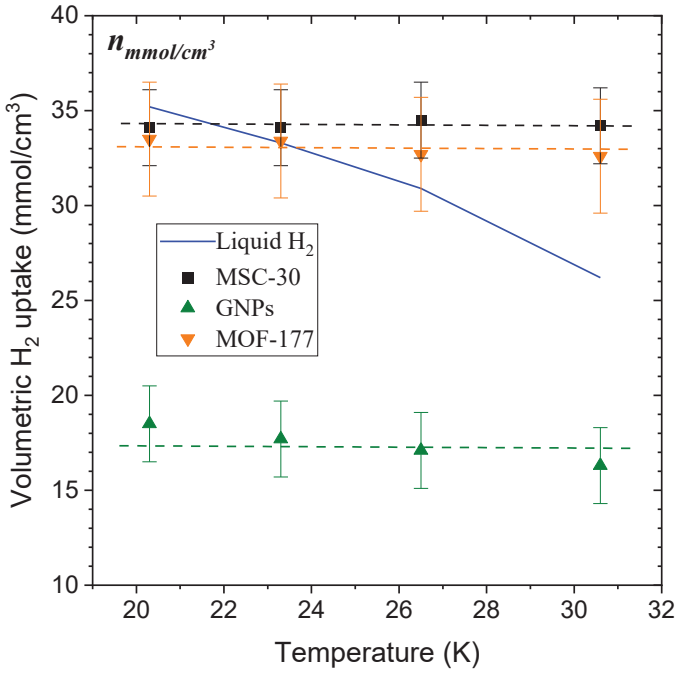

Fig. 4.4.2 The temperature dependence of the volumetric H_2 uptake (n_{mmol/cm^3} in the temperature range of 20.4-30.6 K on MOF-177. MSC-30 and GNPs, respectively

Table. 4.4.1 Summary of the gravimetric H_2 uptake (wt.%), density of adsorbed H_2 ($\rho_{ads.H_2}$, mmol/cm^3), density of adsorbed H_2 in monolayer ($\rho_{ads.H_2}^{mono}$, mmol/cm^3), and volumetric H_2 uptake (n_{mmol/cm^3}, mmol/cm^3) for MOF-177, MSC-30, and GNPs at each temperature and pressure.

		Condition			Adsorbent		
		T [K]	P (MPa	Liquid H_2	MOF-177	MSC-30	GNPs
Gravimetric H_2 uptake	$n_{\text{wt.\%}}$ [wt.%]	20.4	0.10	-	12.9 (90%)[1]	12.2 (74%)[1]	6.6 (42%)[1]
		23.3	0.22	-	12.6 (87%)[1]	11.9 (60%)[1]	6.1 (42%)[1]
		26.5	0.43	-	12.4 (88%)[1]	11.5 (71%)[1]	5.9 (41%)[1]
		30.6	0.88	-	11.9 (86%)[1]	10.8 (76%)[1]	5.3 (41%)[1]
Density of adsorbed H_2	$\rho_{ads.H_2}$ [mmol/cm^3]	20.4	0.10	35.2	47.3 (134%)[2]	43.6 (124%)[2]	40.0 (114%)[2]
		23.3	0.22	33.3	47.1 (141%)[2]	42.4 (127%)[2]	38.0 (114%)[2]
		26.5	0.43	30.9	45.8 (148%)[2]	42.2 (137%)[2]	36.4 (118%)[2]
		30.6	0.88	26.2	45.1 (172%)[2]	41.5 (159%)[2]	32.9 (125%)[2]
Density of monolayer H_2	$\rho_{ads.H_2}^{mono}$ [mmol/cm^3]	20.4	-	35.2	49.3 (140%)[2]	46.7 (133%)[2]	49.3 (140%)[2]
		23.3	-	33.3	50.0 (150%)[2]	52.1 (156%)[2]	47.3 (142%)[2]
		26.5	-	30.9	49.0 (159%)[2]	49.8 (161%)[2]	48.8 (158%)[2]
		30.6	-	26.2	50.6 (193%)[2]	51.2 (195%)[2]	51.8 (198%)[2]
Volumetric H_2 uptake	$n_{\text{mol/cm}^3}$ [mmol/cm^3]	20.4	-	35.2	33.5 (95%)[2]	34.1 (97%)[2]	18.5 (52%)[2]
		23.3	-	33.3	33.4 (100%)[2]	34.1 (102%)[2]	17.7 (53%)[2]
		26.5	-	30.9	32.7 (106%)[2]	34.5 (112%)[2]	17.1 (56%)[2]
		30.6	-	26.2	32.6 (124%)[2]	34.2 (130%)[2]	16.3 (62%)[2]

[1] Ratio (%) of monolayer adsorption in the H_2 uptake

[2] Ratio (%) compared to density of liquid H_2 ($\rho_{liq.H_2}$) at each phase transition point, 35.2 mmol/cm^3 (20.4 K, 0.10 MPa), which are 33.3 mmol/cm^3 (23.3 K, 0.22 MPa), 30.9 mmol/cm^3 (26.5 K, 0.43 MPa), 26.2 mmol/cm^3 (30.6 K, 0.88 MPa)

4.5 Gas dependence of the super-dense hydrogen adsorption

4.5.1 Density of adsorbate for deuterium, neon and nitrogen

In order to compare the superdense H_2 for different gases, the adsorption properties for deuterium (D_2), neon (Ne) and nitrogen (N_2) were investigated at each boiling point (23.6 K for D_2, 27.1 K for Ne and 77.2 K for N_2) in the same way as section 4.2.2. Fig. 4.5.1 shows the isothermal properties of the gas introduction into the cell with and without 1.5 g of MSC-30, where the introduced gas (i-gas) amount is plotted as a function of the pressure. For all gases, the isotherms show the similar adsorption and liquefaction steps to H_2 isotherm. When the i-gas amount in blank cell and the cell with MSC-30 are compared at 0.1 MPa for each gas, the i-gas amount for D_2, Ne, N_2 (except for H_2) in the blank cell are clearly higher than that of MSC-30. These behaviors for D_2, Ne, N_2 consistent to the general understanding of adsorption state of "liquid state ≈ adsorbed state" because the free volume in cell with adsorbents is smaller than that of blank cell. As discussed in the section 4.2.2, the comparable i-H_2 amount in the blank cell and with MSC-30 is due to the effect of the super-dense H_2 adsorption, therefore this result qualitatively suggests that the super-dense effect on D_2, Ne and N_2 are not clearly shown, in other words, the super-dense adsorption is a unique phenomenon for H_2 or strongly enhanced in H_2.

Figs. 4.5.2 show the temperature change of the gas introduction isotherms for D_2, Ne and N_2. The measurements were carried out at 23.6 K (0.10 MPa), 26.4 K (0.22 MPa), 29.8 K (0.44 MPa) and 33.9 (0.88 MPa) for D_2, at 27.1 K (0.10 MPa), 29.4 K (0.22 MPa) and 32.5 K (0.44 MPa) for Ne, at 77.2 K (0.10 MPa), 85.1 K (0.22 MPa) and 92.9 K (0.44 MPa) for N_2, where the pressure in brackets is the liquefaction pressure at each temperature. It is observed that the i-D_2 amount with MSC-30 gradually exceeds the amount in the blank cell with increasing temperature, which is the similar trend to that of H_2 as shown in Fig. 4.2.3 (a). This trend suggests that the density of adsorbed D_2 is also less affected by increasing temperature compared with that of liquid D_2. On the other hand,

the i-Ne and N_2 amount with MSC-30 are always lower than that of blank cell even at higher temperature, suggesting the densities of adsorbed Ne and N_2 are relatively affected by temperature increase unlike the trend of H_2 and D_2.

In the same way as section 4.2.2, the densities of adsorbates for D_2, Ne, and N_2 are quantitively evaluated and the results are summarized in Figs. 4.5.3 and Table. 4.5.1. The density of adsorbed D_2 shows the value in the range of 40.4~31.4 mmol/cm^3 in the temperature range from 23.6 to 33.9 K, which is slightly higher than that of H_2. At any temperature, the densities of adsorbed D_2 show higher density than that of liquid D_2, and they are less affected by temperature increase similar to the temperature independent properties of the super-sense H_2. The density ratios of adsorbed phase to liquid phase ($\rho_{ads.}/\rho_{liq.}$) for each gas are summarized in Table. 4.3.1. It can be seen that $\rho_{ads.}/\rho_{liq.}$ ratios for H_2 and D_2 increase with temperature in the range of 1.24~1.61 and 1.19~1.35, respectively. Comparing the ratio of H_2 ($\rho_{ads.H_2}/\rho_{liq.H_2}$) with that of D_2 ($\rho_{ads.D_2}/\rho_{liq.D_2}$), $\rho_{ads.H_2}/\rho_{liq.H_2}$ ratio is always higher than $\rho_{ads.D_2}/\rho_{liq.D_2}$ ratio at any temperature. It suggests that the adsorbed H_2 is more strongly affected by the effect of super-dense adsorption compared with D_2 adsorption. On the other hand, the temperature changes of the adsorbed Ne and N_2 density are totally comparable to that of liquid Ne and N_2, and both $\rho_{ads.}/\rho_{liq.}$ ratios are around 1.0 at any temperature, which are in the good agreement with the general understanding of adsorption state of "liquid state ≈ adsorbed state". In addition, the experimentally observed super-dense adsorption of H_2 and D_2 are confirmed as the special adsorption compared with the adsorption of Ne and N_2.

The monolayer densities of H_2 and D_2 are evaluated in the same way as section 4.4. Fig.4.5.4 shows the densities of monolayer D_2 in the temperature range of 23.6-33.9 K. The density of monolayer D_2 also shows a constant value of around 50 mmol/cm^3 without temperature dependence below the critical temperature of D_2. It is remarkable that the densities of adsorbed D_2 and H_2 are comparable in the super-dense state of monolayer, even though the density of liquid D_2 is

1.15 times higher than that of H_2 at each boiling point. The H_2 molecule with light mass is strongly affected by quantum effects at low temperature, yielding the lower density of bulk-liquid H_2 due to the high zero-point energy compared with that of D_2 (see the introduction section 1.2). However, the difference of adsorbed density between the monolayer H_2 and D_2 is not observed below each critical point. The quantum effects in bulk-liquid H_2 and D_2 seem to be cancelled by interactions of adsorption with the material surface.

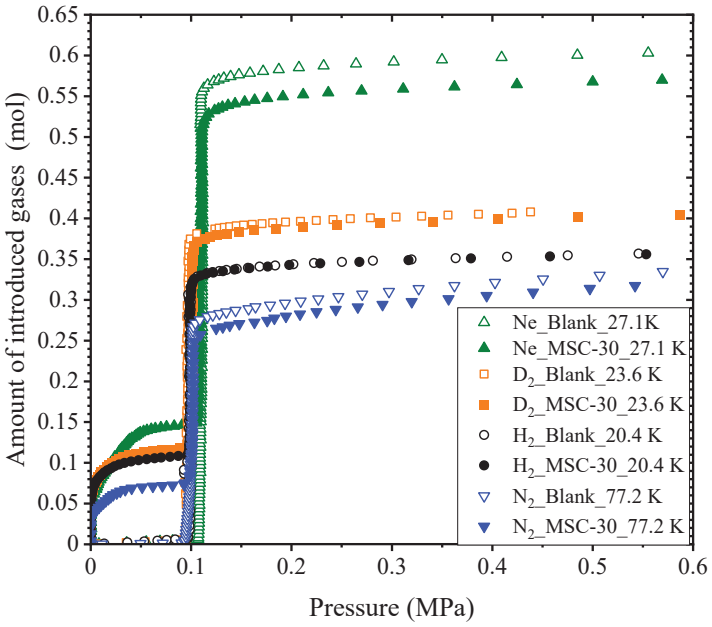

Fig. 4.5.1 Isothermal properties of gas introduction into the empty cell (Blank) and the cell with 1.5 g of MSC-30 for H_2, D_2, Ne and N_2 at each boiling point of 20.4 K, 23.6 K, 27.1 K and 77.2 K, respectively.

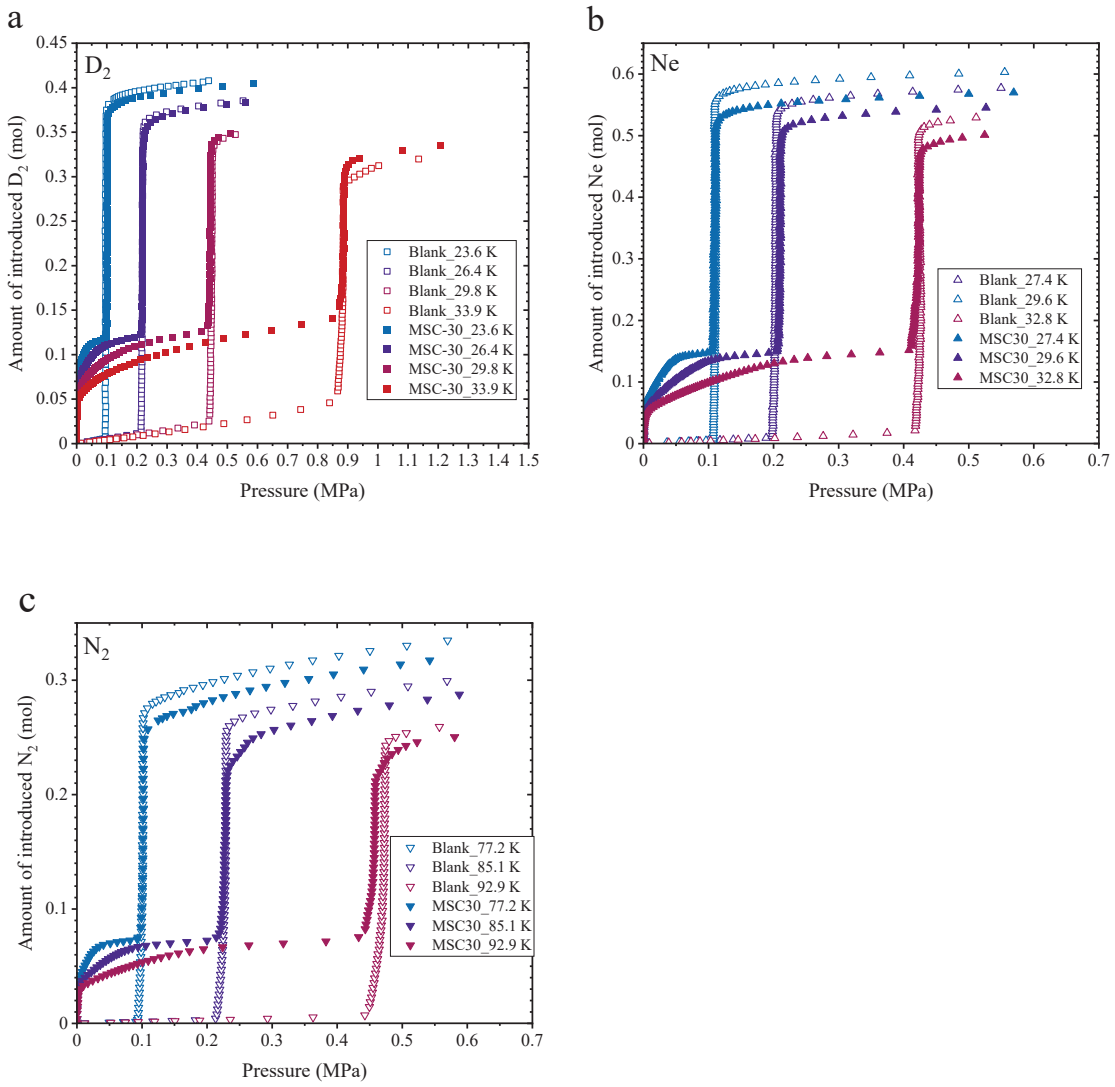

Fig. 4.5.2 Temperature dependence of isothermal properties of gases introduction for (a) D_2, (b) Ne and (c) N_2 into the empty cell (Blank) and the cell with 1.5 g of MSC-30, at 23.6, 26.4, 29.8 and 33.9 K for D_2, at 27.4, 29.6, 32.8 K for Ne, 77.2, 85.1, 92.9 K for N_2.

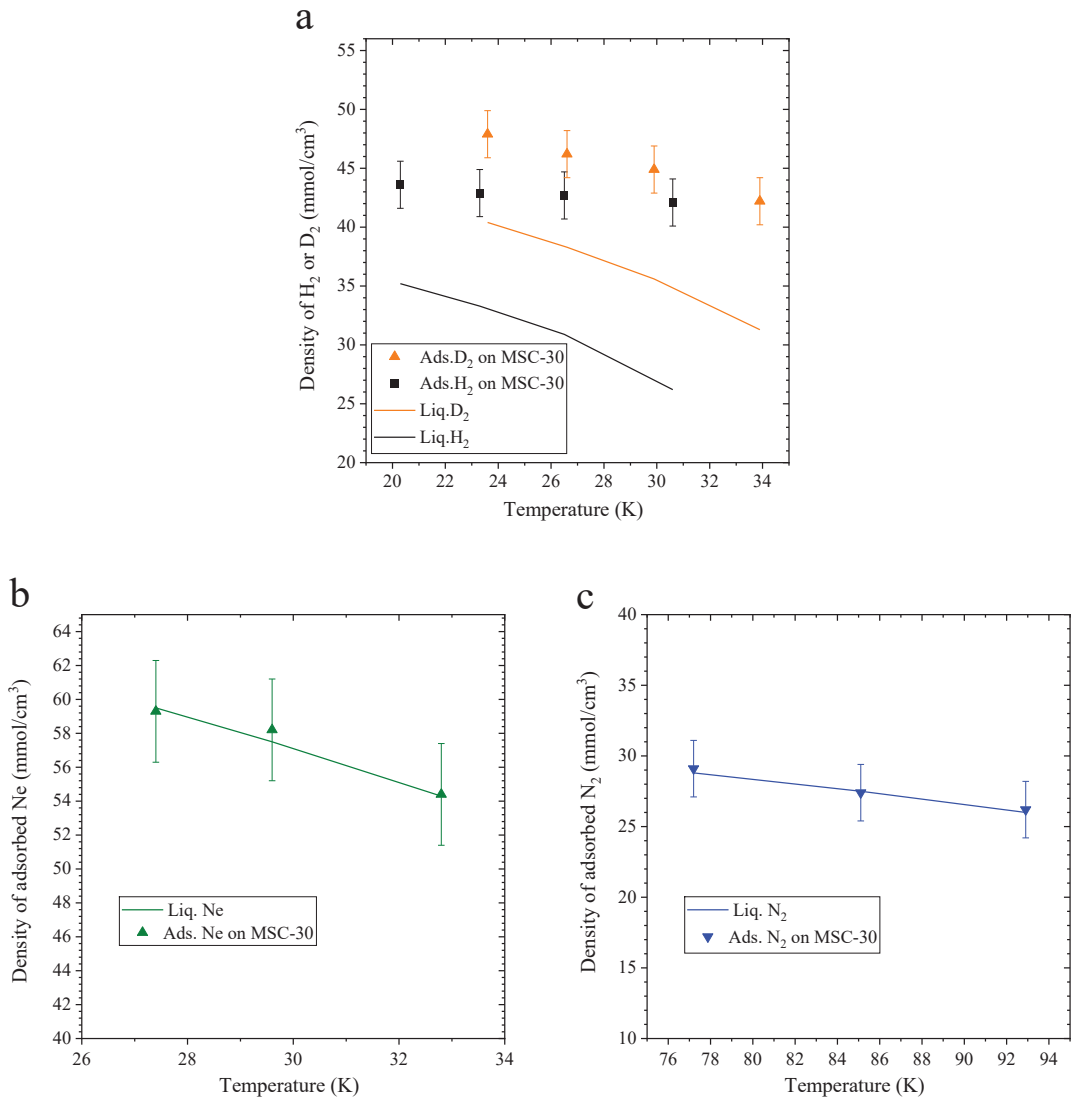

Fig. 4.5.3 Temperature dependence of the density of adsorbate for (a) H_2 and D_2, (b) Ne and (c) N_2, compared with the density of liquid phase.

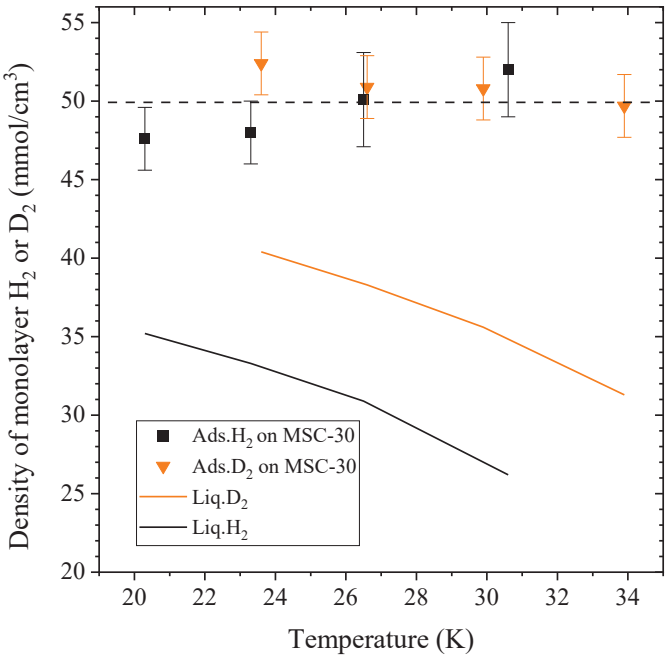

Fig. 4.5.4 Temperature dependence of the density of monolayer H_2 and D_2 compared with the density of liquid phase.

Table. 4.5.1 Density of adsorbate and liquid phase for H_2, D_2, Ne and N_2 and monolayer, and Monolayer density for H_2 and D_2 at each temperature below critical point.

Gas	Condition						
	Temp.	Liquefied pressure	Liquid density	Density of adsorbate	Ads./Liq.×100	Monolayer density	Ads./Liq.×100
	K	MPa	mmol/cm^3	mmol/cm^3	%	mmol/cm^3	%
H_2	20.4	0.10	35.2	43.6	124	47.6	135
D_2	23.6		40.4	47.9	119	52.4	130
Ne	27.1		59.5	59.3	100	-	-
N_2	77.2		28.8	29.1	101	-	-
H_2	23.3	0.22	33.3	42.9	129	48	144
D_2	26.4		38.3	46.2	121	50.9	133
Ne	29.4		57.5	58.2	101	-	-
N_2	85.1		27.5	27.4	100	-	-
H_2	26.5	0.44	30.9	42.7	138	50.1	162
D_2	29.8		35.6	44.9	126	50.8	143
Ne	32.5		54.3	54.4	100	-	-
N_2	92.9		26.0	26.2	101	-	-
H_2	30.6	0.88	26.2	42.1	161	52	204
D_2	33.9		31.4	42.2	135	49.7	158

4.5.2 Two-dimensional density

Figs. 4.5.5 show the adsorption isotherms for H_2, D_2, Ne and N_2 on MSC-30, which represent the molar basis uptake (mmol/g) as a function of the relative pressure, where each temperature was determined so that the liquefaction pressure was at 0.10 MPa for (a), at 0.22 MPa for (b), at 0.44 MPa for (c) and at 0.88 MPa for (d). Fig. 4.5.5 (a) shows the adsorption isotherms for H_2, D_2, Ne and N_2 at each boiling point of 20.4, 23.6, 27.1, and 77.2 K, respectively. The all isotherms can be classified as Type I. The maximum adsorption uptake is in order of Ne, D_2, H_2 and N_2 corresponding to the trend of liquid density as shown in Table 4.5.2. The monolayer uptakes for each gas were evaluated by applying the BET equation into the isotherms, and the points of monolayer completion, defined as B-point in the experimental section 3.1.3., are marked as open dots in Figs. 4.5.5 (a), and the results are summarized in Table. 4.5.2. It is observed that B-point of H_2 is equivalent or close to the point of D_2 and Ne even though D_2 and Ne have much higher total uptake (n_{max} at $p_0/p=1$) than that of H_2. As a result, the ratio of the monolayer uptake to the total uptake (n_{mono}/n_{max}) for H_2 shows the highest ratio of 79 % compared with the ratios of D_2 (69%), Ne (60%) and N_2 (67%) at each boiling point. The monolayer ratio for H_2 is clearly higher than the ratios for other gases even using the same adsorbent of MSC-30, which is obviously due to the super-dense adsorption of monolayer H_2 and the region of multilayer adsorption correspond to the properties of liquid phase. In this way, the anomalously high area density (two-dimensional density) of super-dense H_2 is revealed. For other temperatures in Figs. 4.5.5 (b), (c), and (d), the similar trends to the result of Fig. 4.5.5 (a) are observed. The monolayer H_2 capacities (B-point) are relatively close to that of D_2 and Ne, even though the total uptake of D_2 and Ne are clearly higher than H_2, especially, the monolayer capacity of H_2 is higher than that of Ne in Fig. 4.5.5 (c).

In order to discuss the area densities of adsorbates in more details, the cross-sectional areas (σ) for all adsorbates were evaluated by equation 4.5.1.

$$\sigma = \frac{S_a}{n_m \cdot N_A}, \tag{4.5.1}$$

where S_{gravi} (m^2/g) is the gravimetric surface area, $n_{mmol/g}$ (mmol/g) is the monolayer capacity as defined in equation 3.1.34, N_A is the Avogadro number (6.02×10^{23} mol^{-1}). The evaluated σ, which is called "experimental σ" below, for each adsorbate and temperature is shown in Table 4.5.2. Emmett et al. propose that the cross-sectional area of adsorbates is related to the volume factor of $W^{2/3}$. W is given by

$$W = \frac{M}{N_A \cdot \rho}, \tag{4.5.2}$$

where M is the molar mass of adsorbates, ρ is the density of liquid or solid phase. Thus, the cross-sectional area σ can be theoretically evaluated by

$$\sigma = F\left(\frac{M}{N_A \cdot \rho}\right)^{2/3}, \tag{4.5.3}$$

where F is the packing factor. $F = 1.091$ is well used as the hexagonal close-packed factor [28]. The evaluated σ from equation 4.5.3 is called "theoretical σ". The theoretical σ is evaluated based on the liquid density and the hexagonal close-packed factor, and the results are summarized in Table 4.5.2. The experimental σ of Ne and N_2 are comparable to the theoretical σ at each boiling point, indicating the properties of Ne and N_2 adsorbates are close to the liquid phase. On the other hand, the experimental σ of H_2 and D_2 are 10.3 and 10.1 $Å^2$/molecule, respectively, which are quite lower than the theoretical σ of 14.2 and 13.0 $Å^2$/molecule, respectively, indicating the anomalously high area density due to the super-dense H_2 and D_2. In addition, the packing factors of F are evaluated experimentally to introduce the experimental σ into the equation 4.5.3 (called "experimental F" below), and the results are summarized in Table 4.5.2. The experimental F of H_2 and D_2 are 0.79 and 0.85, respectively, at each boiling point, which are also unusually low compared with the typical packing factor of 1.091. These results indicate the anomalously high two-dimensional density of H_2 and D_2 on the adsorbent, not expected from the liquid phase. For other temperatures, the

experimental σ of H_2 and D_2 shows relatively constant value in the range of 10.3-11.3 and 10.1-11.4, respectively, even at higher temperature up to each critical point, which are much lower than the theoretical σ in the range of 14.2-17.3. Thus, temperature independence of area density of the super-dense H_2 and D_2 are revealed.

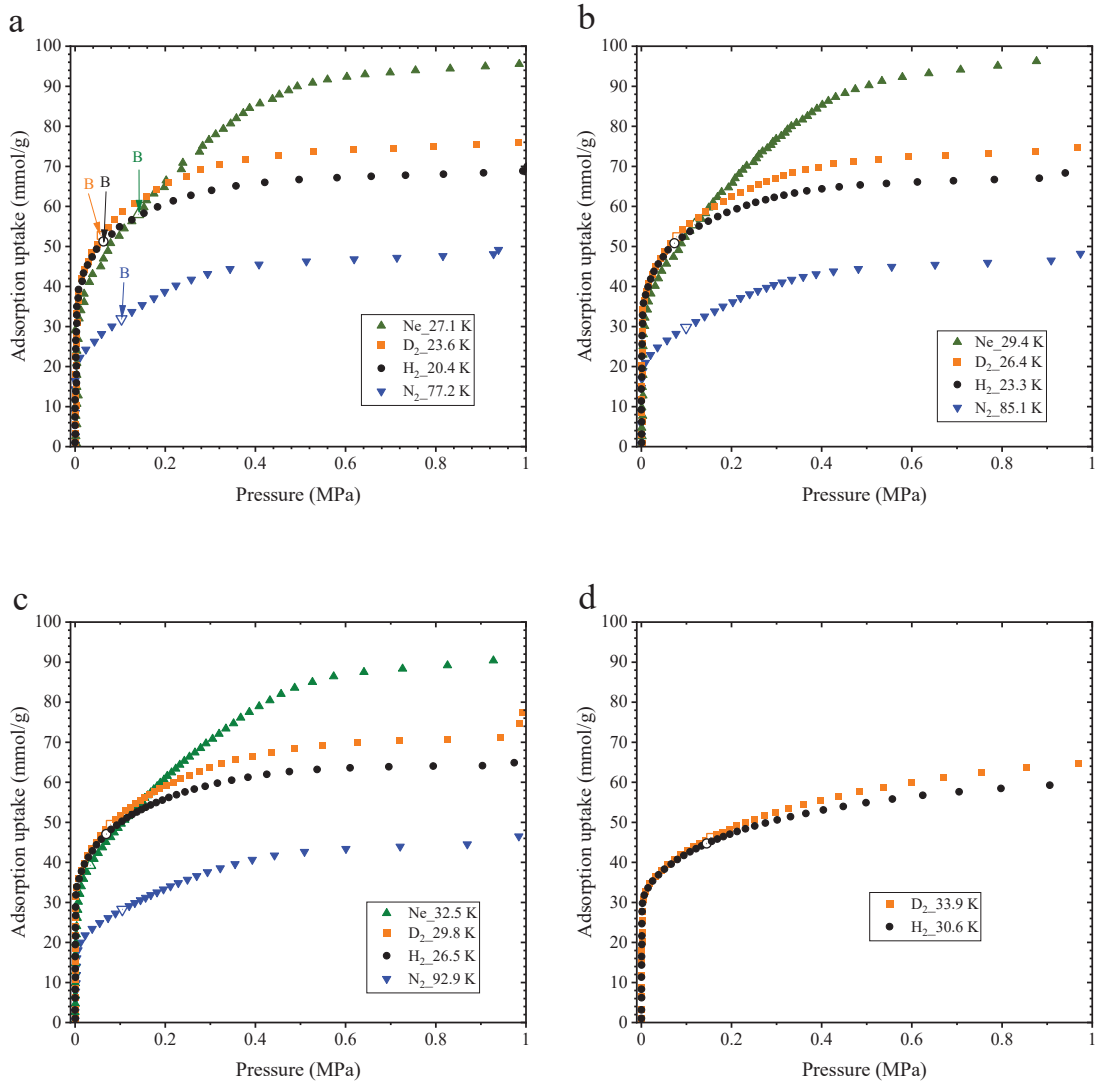

Fig. 4.5.5 Adsorption isotherms of the molar basis uptake for H_2, D_2, Ne and N_2 on MSC-30 as a function of the relative pressure, and each temperature correspond to the liquefaction pressure at (a) 0.10 MPa, (b) 0.22 MPa, (c) 0.44 MPa and (d) 0.88 MPa. The points of monolayer completion (B-point) are marked as open dots.

Table. 4.5.2 Adsorption uptakes and cross-sectional area for H_2, D_2, Ne and N_2 at each temperature.

	Condition		Liquid	Adsorption uptake					
	Temp.	Liquefied pressure	Liquid density	Total uptake	Monolayer uptake	Monolayer ratio	Cross-sectional area (this study)	Packing factor (F)	Cross-sectional area (F=1.091)
	K	MPa	mmol/cm^3	mmol/g	mmol/g	%	Å^2/molecule		Å^2/molecule
H_2	20.4	0.10	35.2	65.2	51.5	79	10.3	0.79	14.2
D_2	23.6		40.4	76	52.4	69	10.1	0.85	13.0
Ne	27.1		59.5	96.2	58.1	60	9.1	0.99	10.0
N_2	77.2		28.8	49	32.7	67	16.2	1.09	16.3
H_2	23.3	0.22	33.3	63.5	49.8	78	10.6	0.79	14.8
D_2	26.4		38.3	74.3	51.8	70	10.3	0.83	13.5
Ne	29.4		57.5	94.5	55.9	59	9.5	1.01	10.3
N_2	85.1		27.5	48.1	30	62	17.7	1.15	16.8
H_2	26.5	0.44	30.9	60.9	46.7	77	11.3	0.8	15.5
D_2	29.8		35.6	71.6	49.5	69	10.7	0.83	14.1
Ne	32.5		54.3	90.3	33.8	37	15.7	1.6	10.7
N_2	92.9		26.0	47.2	27.9	59	19	1.19	17.4
H_2	30.6	0.88	26.2	52.3	44.4	85	10.7	0.67	17.3
D_2	33.9		31.4	66.2	46.3	70	11.4	0.81	15.4

References

1. Otowa, T., Tanibata, R. & Itoh, M. Production and adsorption characteristics of MAXSORB: High-surface-area active carbon. *Gas Separation and Purification* **7**, 241–245 (1993).
2. Zhao, W., Fierro, V., Fernández-Huerta, N., Izquierdo, M. T. & Celzard, A. Impact of synthesis conditions of KOH activated carbons on their hydrogen storage capacities. *Int J Hydrogen Energy* **37**, 14278–14284 (2012).
3. Saha, D., Wei, Z. & Deng, S. Equilibrium, kinetics and enthalpy of hydrogen adsorption in MOF-177. *Int J Hydrogen Energy* **33**, 7479–7488 (2008).
4. Furukawa, H., Miller, M. A. & Yaghi, O. M. Independent verification of the saturation hydrogen uptake in MOF-177 and establishment of a benchmark for hydrogen adsorption in metal-organic frameworks. *J Mater Chem* **17**, 3197–3204 (2007).
5. Huo, S. H. & Yan, X. P. Metal-organic framework MIL-100(Fe) for the adsorption of malachite green from aqueous solution. *J Mater Chem* **22**, 7449–7455 (2012).
6. Lin, K. S., Adhikari, A. K., Ku, C. N., Chiang, C. L. & Kuo, H. Synthesis and characterization of porous HKUST-1 metal organic frameworks for hydrogen storage. *Int J Hydrogen Energy* **37**, 13865–13871 (2012).
7. Soleimani Dorcheh, A. & Abbasi, M. H. Silica aerogel; synthesis, properties and characterization. *J Mater Process Technol* **199**, 10–26 (2008).
8. Do, X. D., Hoang, V. T. & Kaliaguine, S. MIL-53(Al) mesostructured metal-organic frameworks. *Microporous and Mesoporous Materials* **141**, 135–139 (2011).
9. Tsai, C. W. & Langner, E. H. G. The effect of synthesis temperature on the particle size of nano-ZIF-8. *Microporous and Mesoporous Materials* **221**, 8–13 (2016).
10. Nitta, Y., Yamanishi, O., Sekine, F., Imanaka, T. & Teranishi, S. Effect of supports on enantioselectivity of modified Ni catalyst. *J Catal* **79**, 475–480 (1983).
11. Murialdo, M., Stadie, N. P., Ahn, C. C. & Fultz, B. Krypton Adsorption on Zeolite-Templated Carbon and Anomalous Surface Thermodynamics. *Langmuir* **31**, 7991–7998 (2015).
12. Seo, S., Mikšík, F., Maeshiro, Y., Thu, K. & Miyazaki, T. Performance evaluation of an adsorption heat pump system using msc-30/r1234yf pair with the impact of thermal masses. *Applied Sciences (Switzerland)* **11**, 1–25 (2021).
13. Sosa, J. E. *et al.* Exploring the Potential of Metal–Organic Frameworks for the Separation of Blends of Fluorinated Gases with High Global Warming Potential. *Global Challenges*

2200107, (2022).

14. Wickenheisser, M., Herbst, A., Tannert, R., Milow, B. & Janiak, C. Hierarchical MOF-xerogel monolith composites from embedding MIL-100(Fe,Cr) and MIL-101(Cr) in resorcinol-formaldehyde xerogels for water adsorption applications. *Microporous and Mesoporous Materials* **215**, 143–153 (2015).
15. Cho, K. H. *et al.* Pore control of Al-based MIL-53 isomorphs for the preferential capture of ethane in an ethane/ethylene mixture. *J Mater Chem A Mater* **9**, 14593–14600 (2021).
16. Boateng, E. & Chen, A. Recent advances in nanomaterial-based solid-state hydrogen storage. *Mater Today Adv* **6**, 100022 (2020).
17. Wong-Foy, A. G., Matzger, A. J. & Yaghi, O. M. Exceptional H2 saturation uptake in microporous metal-organic frameworks. *J Am Chem Soc* **128**, 3494–3495 (2006).
18. Thomas, K. M. Hydrogen adsorption and storage on porous materials. *Catal Today* **120**, 389–398 (2007).
19. Bénard, P. & Chahine, R. Storage of hydrogen by physisorption on carbon and nanostructured materials. *Scr Mater* **56**, 803–808 (2007).
20. Poirier, E., Chahine, R. & Bose, T. K. Hydrogen adsorption in carbon nanostructures. *Int J Non Linear Mech* **26**, 831–835 (2001).
21. Kojima, Y. *et al.* Hydrogen adsorption and desorption by carbon materials. *J Alloys Compd* **421**, 204–208 (2006).
22. Latroche, M. *et al.* Hydrogen Storage in the Giant-Pore Metal–Organic Frameworks MIL-100 and MIL-101. *Angewandte Chemie* **118**, 8407–8411 (2006).
23. van Kranendonk, J. *SOLID HYDROGEN*. (Plenum, 1983).
24. Kogan, V S; Lazarev, B G; Bulatova, R. F. The crystalline structure of hydrogen and deuterium. *Soviet Phys. JETP* **4**, (1957).
25. WH Keesom, J De Smedt, H. M.-P. R. A. A. On the crystal structure of para-hydrogen at liquid helium temperatures. *Proc Royal Acad Amsterdam* **33**, 814 (1930).
26. Balderas-Xicohténcatl, R. *et al.* Formation of a super-dense hydrogen monolayer on mesoporous silica. *Nat Chem* (2022) doi:10.1038/s41557-022-01019-7.
27. Thommes, M. *et al.* Physisorption of gases, with special reference to the evaluation of surface area and pore size distribution (IUPAC Technical Report). *Pure and Applied Chemistry* **87**, 1051–1069 (2015).

28. Livingston, H. K. The cross-sectional areas of molecules adsorbed on solid surfaces. *J Colloid Sci* **4**, 447–458 (1949).

5. Conclusion

In this thesis, the systematic investigation of the cryogenic H_2 adsorption properties was carried out to understand the super-dense H_2 state, which showed higher density than liquid H_2 density, from the following point of view, 1) Material dependence, 2) Temperature dependence, 3) Adsorbed layer dependence and 4) Gas dependence.

1) Material dependence

The densities of adsorbed H_2 at the boiling point of H_2 (20.4 K) for various kind of adsorbents, such as carbon materials, MOFs, and the silica gels, show the values in the range of 38.4~47.3 mmol/cm^3, which are higher than that of liquid H_2 (35.2 mmol/ cm^3). Namely, the super-sense H_2 state can form on any adsorbents regardless of material species and pore structures. In particular, the adsorbents with Type I adsorption isotherms given by micropores show relatively high densities of adsorbed H_2 in the range 43.0~47.4 mmol/cm^3, which is higher than that of solid H_2 (43 mmol/cm^3).

2) Temperature dependence

The temperature dependence of the super-dense H_2 state is investigated below the critical temperature of H_2 (33 K) for the adsorbents of MSC-30 and MOF-177 with Type I adsorption, and GNPs with Type II adsorption. For all adsorbents, the phenomenon of super-dense H_2 adsorption is observed at any temperatures. Especially, the densities of adsorbed H_2 on MSC-30 and MOF-177 with micropores do not significantly decrease with temperature rise compared with that of liquid H_2, suggesting that the temperature dependence of super-dense H_2 state is not large. The feasibility of suppression for liquid H_2 boil-off by using the super-dense H_2 with small temperature dependence is discussed. In the case of a temperature increase from 23 to 30 K under isobaric condition at 0.9 MPa,

the boil-off amount of liquid H_2 is reduced by 32% when MSC-30 is filled in the cell.

3) Adsorbed layer dependence

In order to discuss the super-dense H_2 state in more details, the behaviors of monolayer and multilayer H_2 are discussed separately. The density of monolayer H_2 is evaluated based on the BET theory, and then the multilayer H_2 is assumed to be the liquid phase. It is clarified that the density of monolayer H_2 has a constant value of 50 mmol/cm^3 without temperature and material dependence. Interestingly, the density of monolayer H_2 clearly exceeds the density of solid H_2 (43 mmol/cm^3). In order to increase the volumetric H_2 uptake including the volume of adsorbents themselves, it is found that the volumetric surface area of adsorbents is a unique factor, and it is proportional to the volumetric H_2 uptake. This is important for developing materials to obtain higher volumetric H_2 uptake for the super-dense H_2 adsorption. In this work, MSC-30 with the highest volumetric surface area (7975 m^2/cm^3) shows the highest volumetric H_2 density (33 mmol/cm^3), which is comparable to that of liquid H_2 at 23 K.

4) Gas dependence

The density of adsorbed H_2 is compared with those of adsorbed D_2, Ne, and N_2 at each boiling point, and the temperature dependence of adsorbed density is discussed for each gas. It is found that the densities of adsorbed Ne and N_2 are equivalent to that of each liquid phase, indicating that Ne and Ne do not form the superdense state. On the other hand, the density of adsorbed D_2 is higher than that of liquid D_2, which is the similar trend to H_2. In addition, the density of monolayer D_2 shows a constant value of 50 mmol/ cm^3 without temperature dependence below the critical point of D_2 (38.3 K). It is clarified that the densities of monolayer D_2 and H_2 are comparable, even though the density of bulk-liquid D_2 is 1.15 times higher than that of bulk-liquid H_2 at each boiling point. It

is known that the lower density of bulk-liquid H_2 is caused by the higher zero-point energy compared with that of D_2. From these results, it can be expected that the difference between bulk-liquid H_2 and D_2 density due to the quantum effect is cancelled out by interactions between adsorbates and adsorbents at cryogenic conditions, and the super-dense H_2 is formed.

Acknowledgements

I would like to express my great appreciation to my supervisor, Professor Takayuki Ichikawa for his supervision, helpful guidance, discussions. He gave me a lot of opportunity and experience for helping the progress of this work, my career and my growth as a person. I would like to express my special thanks to Associate Professor Hiroki Miyaoka for all supports and encouragement. He always supports my research, presentations, and writing papers. I would like to great appreciate to Professor Norio Ogita for helping my experiments, and for the valuable comments and discussions. I would like to offer my special thanks to my co-researcher of Mr. Laurent Prost, Dr. Marolop Simanullang, Mr. Ogawa Tomofumi in Air Liquide, Research & Development, Innovation Campus Tokyo for all of cooperations and for providing the samples for this work. Finally, I gratefully acknowledge to the past and present members of my laboratory, Mr. Tomoyuki Ichikawa, Dr. Khushbu Sharma, Mr. Yuki Kashiwara, Mr. Yuki Itoh, Project Professor Hitoshi Saima, Assistant Professor Fangqin Guo, Project Assistant Professor Rini Singh, and Dr. Keita Shinzato for their king help in my doctoral course.